SYNTHESIS OF Co-Cr-Mo/ FLUORAPATITE NANO-COMPOSITE COATINGS BY PULSED LASER DEPOSITION FOR DENTAL APPLICATIONS

By

OSAMA MOHAMED IBRAHIM KHFAGI

Thesis submitted in fulfilment of the requirements for the degree
Magister of Technology: Biomedical Technology

In the Faculty of Health and Wellness Sciences
At the Cape Peninsula University of Technology

Supervisor: Professor**.** D Gihwala
Co-supervisor: Professor**.** M Maaza

Bellville
August 2015

DECLARATION

I, Osama Mohamed Ibrahim Khfagi, declare that the contents of this dissertation/thesis represent my own unaided work, and that the dissertation/thesis has not previously been submitted for academic examination towards any qualification. Furthermore, it represents my own opinions and not necessarily those of the Cape Peninsula University of Technology.

Signed **Date**

ABSTRACT

Metallic materials play an essential role in assisting with the repair or replacement of bone tissue that has become diseased or damaged. Metals are more suitable for load bearing applications compared to ceramics or polymeric materials due to high mechanical strength and fracture toughness that are exhibited by metallic materials. However, the main limitation in the application of these metallic materials is the release of the toxic metallic ions. The release of these ions is caused by the interaction of metallic materials with human body fluids. These ions react with body tissue, which might lead to various adverse tissue reactions and/or hypersensitivity reactions.

Cobalt-chromium-molybdenum (Co-Cr-Mo) alloys are one of the most useful alloys for biomedical applications such as dental and orthopedic implants because of acceptable mechanical properties and biocompatibility. However, the use of these alloys in biomedical applications has of late come under scrutiny recently due to unacceptable revision rates of applications such as hip resurfacing and total hip arthroplasty designs. Failure analysis has demonstrated that solid and soluble wear debris and corrosion products resulted. This release of ions from the joints has resulted in adverse local tissue reactions. Laser-aided deposition is a material additive based manufacturing process via metallurgically bonding the deposited material to the substrate. Due to its capability to bond various materials together, it became an attractive technology The principal aims of this study were to 1a) fabricate nanocomposite materials by depositing fluorapatite nanopowder onto the Co-Cr-Mo dental alloy using pulsed laser deposition and 1b) evaluate which laser beam energy and layer thickness, based on the exposure time period, would be applicable, and 2) evaluate bioactivity properties on biological material.

The fluorapatite nanopowder, of particle-size of 40 to 60 nanometer, was prepared by mixing stoichiometric amounts of calcium hydroxide, ($Ca(OH)_2$), phosphorous-pentoxide (P_2O_5) and calcium fluoride (CaF_2) in a planetary high energy ball mill using zirconium vial. The powder was pressed into pellet form for use in the deposition process. In principle, five specimens were prepared: a) Energy of 130 mJ and five minutes exposure time, b) energy of 130 mJ and 10 minutes exposure time, c) 130 mJ and 20 minutes exposure time, d) 170 mJ and 10 minute exposure time, and e) 170 mJ and 15 minutes exposure time. For non-destructive instrumental analysis, X-ray Diffraction was applied to determine the phases and unit cell structure, Scanning Electron Microscopy was used to determine the distribution of the fluorapatite layer, Energy Dispersive analysis of X-rays was used to obtain the chemical composition in terms of concentration and Atomic Force Microscopy was used to obtain a three-dimensional image of the deposited layer. For bioactivity, the specimens were immersed in Simulated Body Fluid (SBF) for a period of 14 days. After this period the specimens were dried at ambient temperature.

In this study it was determined that:

1. The layer deposited at 130 mJ and for a period of five minutes, nearly completely dissolved into the SBF;

2. For the specimen prepared at 130 mJ and for a period of 10 minutes, the solution of the FA layer occurred but to a lesser extent;
3. The specimen prepared at 130 mJ and for a period of 20 minutes only minutely dissolved into SBF;
4. The specimen prepared at 170 mJ and for a period of 10 minutes only minutely dissolved into the SBF and,
5. The specimen prepared at 170 mJ for a period of 15 minutes did not dissolve into the SBF.

It was concluded that a layer thickness resulting after an exposure period of 20 minutes at energy of 130 mJ or thickness resulting after 15 minutes of exposure at an energy of 170 mJ are optimum.

KEYWORDS

Biocompatibility
Pulsed Laser Deposition (PLD)
Co-Cr-Mo
Fluorapatite
Simulated body fluid (SBF)
Dental matrial
Cobalt-Chromium-Molybdenum Alloys
Dental alloy-materials
Porcelain laboratory scales Ball-Mill dimension
Lab Pellet Presses (Beckman)
X-ray diffraction (XRD)
Atomic force microscopy (AFM)
Scanning electron microscopy (SEM)
Energy-Dispersive Analysis of X-Rays Spectroscopy (EDAX)

ACKNOWLEDGEMENTS

First and foremost, I thank God (Allah) for giving me the ability and good health to complete the study and the thesis writing successfully.

The thesis would not be possible without the encouragement, guidance and support from many people whom I wish to thank:

First of all, I would sincerely like to thank my supervisor, Professor Dhiro Gihwala for his continuous supervision, support, commitment, and for providing me with the opportunity to study at Cape Peninsula University of Technology (CPUT).

My Co-supervisor Professor, Malik Maaza from iThemba LABS, for his continuous support and excellent supervision throughout my thesis.

I would also like to give a heartfelt thanks to my co-mentor Dr. Ntevheleni Thovhogi from iThemba LABS, for her valuable advice, guidance and encouragement during this study. Her assistance throughout the experiments and writing of the thesis is really appreciated.

My sincere gratitude also goes to the late, Professor Esterhuyse, the head of the Department in the Biomedical Sciences, Faculty of Health and Wellness Sciences, Cape Peninsula University of Technology, who was always guiding, motivating and encouraging me during the study.

My approbation also go to my colleagues from iThemba LABS:

- Dr. Chester Kotsedi, for his advice and helping with anything I needed for this study.
- Dr. Remy Bucher & Mr. Zakhele Khumalo, for assisting in the XRD measurements.
- Dr. M. Nkosi, for AFM imaging and results analysis.
- All the fellows under (UNESCO-CHAIR, South Africa) the nanoscience research group.

I wish to thank

- My country Libya for the opportunity and funds given to me.
- The Department of Biomedical, CPUT, for the unlimited use of their equipment and laboratories to conduct this study.
- Mrs Small from the Chemical Engineer at CPUT Cape Town campus.
- Mr. Adrian Josephs at the University of Western Cape, for helping me with SEM–EDS measurements.

I would also like to extend my sincere gratitude to my family especially to my mother & my father, they were prayed for me and encouraged me to work hard and succeed.

To my wife, Tbrah Nuoh Saleh, who has encouraged support me to do my best in everything that I have undertaken.

To my children, Gehad & Mohammad (Nidal) & Gwad, who have always gave me the smile in the worst conditions.

My deepest appreciation also goes to my brothers and sisters for their motivation and constant encouragement, and finaly I wish to thanks all my friends who have continued to support me without whom the completion of this thesis would not have been possible.

DEDICATION

In the name of Allah the beneficent and the merciful, all praise and thanks is due to

ALLAH" TAALA (الله)

For giving me the ability and health to complete my study successfully.

Contents

List of Figures

List of Tables

Abbreviation

Co-Cr-Mo	Cobalt–chromium–molybdenum
FA	Fluorapatite
PLD	Pulsed Laser Deposition
SBF	Simulate body fluid
XRD	X-ray diffraction
AFM	Atomic force microscopy
EDS	Energy Dispersive X-ray Spectroscopy
SEM	Scanning electron microscopy
fcc	Face centered cubic
hcp	Hexagonal closed packaged
RT	Room temperature

Chapter 1

Introduction

1.1. Introduction

The ultimate goal in dentistry and dental technology is to maintain or improve the quality of life of the patient. This goal can be realised by preventing disease, relieving pain, improving mastication efficiency, enhancing speech and improving aesthetics. To achieve many of these objectives there is an essential a need for the replacement or reshaping of tooth structure. The main challenges for years have been the development and selection of biocompatible, long lasting, direct filling tooth restoratives and indirectly processed prosthetic materials that can withstand the adverse conditions of the oral environment (Anusavice, 2003).

Metallic materials play an essential role in assisting with the repair or replacement of diseased or damage bone tissue. Metals are more suitable for load bearing applications compared with ceramics or polymeric materials because they combine high mechanical strength and fracture toughness (Staiger & Pietak., 2006). However, the main limitation of these metallic materials is the release of the toxic metallic ions that can lead to various adverse tissue reactions and/or hypersensitivity reactions (Wapner, 1991). In the future development of alloys, an effort should be made to gain a better understanding of the interactions between the surface of the metal and its environment, a particular interest should be taken in the interdependence between the physical and chemical state of the alloy's surface and its corrosion behaviour. Corrosion resistance is a very important property for dental alloys, in addition to other properties such as strength, ductility and casting accuracy. Corrosion of dental alloys in the oral environment not only results in the deterioration of restoration. But also involves release of ions that is considered unclear to their biocompatibility (Wataha *et al.*, 1991a).

Metals were used in dentistry for hundreds years (Tuna *et al.*, 2009). The first metallic material used in stomatology was gold in foil form, used as loss and tooth decay fillers. Unfortunately, this material could not be applied to customized crowns and bridges because of their low strength (Supady, 2010; Reimann & Dobrzański, 2011). The used the precious alloys based on gold for prosthodontia declined, which resulted in research for different materials (Dobrzański, 2007).

Cobalt–chromium–molybdenum (Co-Cr-Mo) alloys have been widely used as removable partial dentures metal frames and porcelain-fused-to-metal crowns (Craig *et al.*, 2000; Powers & Sakaguchi., 2006; Wataha, 2002). The reason for this is that these materials are strong and resistant to corrosion. These alloys have also been used in orthopaedics for bone-fixation devices and total hip and knee replacements in both the cast and wrought forms. Therefore, Co-Cr-Mo alloys are essential in medical applications. However, despite these properties, manufacturing processes, such as casting, cutting and plastic-work are usually difficult due to the high melting point (1623–1723 K), hardness and limited ductility of these alloys (Davis, 2003; Montero-Ocampo *et al.*, 1999).

1.2. Background to the problem statement

Co-Cr-Mo alloys are one of the most useful alloys for biomedical applications such as dental and orthopaedic implants because of their excellent mechanical properties and biocompatibility (Granchi *et al.,* 2010; Huang *et al.,* 1999; Haynes *et al.*, 2000; Klawitter *et al.,* 1977). However, as indicated, the cast alloys (the ASTM[1]-75 specification) exhibit low ductility compared to forged alloys (the ASTM-799 and ASTM-1537 specification) and Co-based dental casting alloys occasionally fracture during small plastic deformation caused by the adjustment (Herö *et al.,* 1984). Under cast conditions, Ni-, C- and N-free Co-Cr-Mo alloys exhibit low ductility owing to the formation of shrinkage porosity, interdendritic segregation and intermetallic inclusions at the grain boundaries (Lee *et al.,* 2006). This is especially so in the instance of the α-phase, formed along the interdendritic region during the solidification, when brittle fracture occurs (Lee *et al.,* 2006). Therefore, it is essential to suppress the formation of the α-phase in the as-cast Co-Cr-Mo alloys, to improve the ductility. Various studies on chemical composition and casting technology have been performed to improve the strength and ductility of these alloys (Salinas-Rodriguez, 1999). Moreover, maintaining the crystal structure of the Co-Cr-Mo alloys to be the γ-phase (face-centred cubic, *fcc*) is considerably effective in keeping the Co-Cr-Mo alloys ductile since the α-phase satisfies the Von Misses criterion, for which five independent slip systems are required for good ductility. According to the ternary phase diagram of the Co-Cr-Mo system (Figure 1.1), the crystal structure of the alloy will transform from the α-phase, which is stable at high temperatures (1600 K) to the ε-phase (hexagonal close packing, hcp) which is stable at room temperature and is martensitically or diffusionally dependent on the cooling rate. In order to stabilize the γ-phase, the addition of a fourth element to Co-Cr-Mo alloys is one of the effective methods. Shi *et*

---

[1] American Standard Testing Materials

al., (1993) have reported that Ni, C, and N addition stabilize the γ-phase in Co-Cr-Mo alloys.

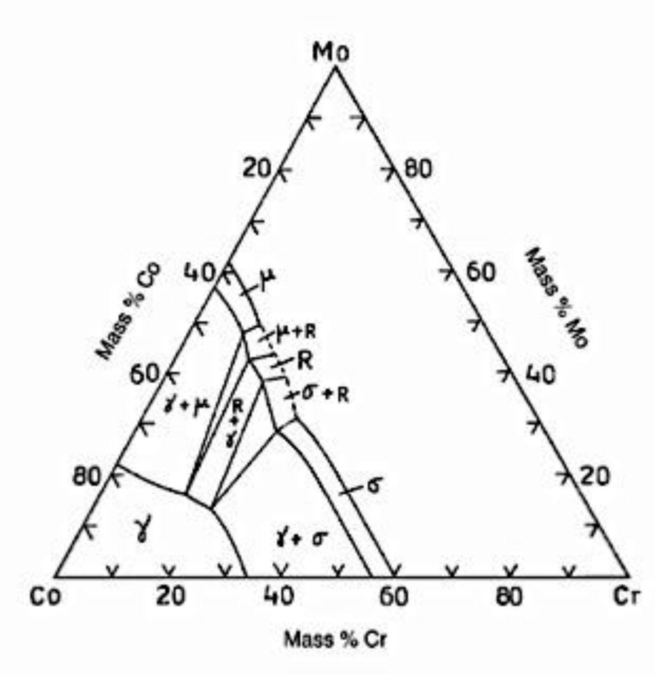

Figure 1.1: The ternary phase diagram of the Co-Cr-Mo system at 1200⁰C (Shie *et al.,* 1993).

Carbon addition is often used to improve the mechanical properties of the Co-Cr-Mo alloys. Carbon also has an ability to increase the stability of the α-phase, but forms the $M_{23}C_6$ carbide. When coarse $M_{23}C_6$ carbides precipitate along grain boundaries then preferential sites for fatigue crack propagation are formed (Zhuang & Langer, 1989). In the instance of N, the addition, especially in high % (mass/mass)[2] concentrations to stainless steels stabilizes the α-phase, and considerably improvement in the tensile and fatigue strength of austenitic stainless steels (Menzel *et al.,* 1996; Horovitz *et al.,* 1996).

It is also expected that the stability of the α-phase would be improved by N addition of Co-Cr-Mo alloys, considering the similarity in crystal structure and lattice parameter between the Fe-Cr and Co-Cr systems present in the steel. Both alloy systems have the *fcc* structure at high temperatures and similar lattice parameters of approximately 0.357 to 0.360 nm (Kliner *et al.,* 1987). Main substitutional-solid solution element for both these alloys is Cr, which affects the solubility and mobility of interstitial solute elements such as C and N atoms. Moreover, Cr strongly increases solubility of N in Fe-Cr systems (Menzel *et al.,* 1996).

---

[2] From here onwards % will denote % mass per mass and %at the atomic percentage.

1.2.1. Problem statement

Metallic biomaterials have been successfully used for dental and orthopaedic applications. However, metallic implants are bio-inert and have poor interfacial bond between the tissue and the implant due to bio-inert surface itself. Surface treatment, compositional improvement, structural modification or changing the bio-inert property into bioactivity could increase the interfacial bond between living cells and the implant materials in order to increase the *in vivo* lifetime of the metallic implants (Ryan *et al.,* 2006; Krishna *et al.,* 2007; Xue *et al.,* 2007).

Fluorapatite ($Ca_{10}(PO_4)_6F_2$) is one of the attractive bioactive ceramics which has excellent biocompatibility properties. Its attractiveness is due to its similarity in structure and composition to teeth and bone with the added benefit of fluoride release. In vitro studies have shown that fluorapatite is biocompatible and has a higher stability in comparison with hydroxyapatite. In addition, fluoride release takes place at a controlled rate to ensure the formation of a mechanically and functionally strong bone stevedore (Rodriguez-Lorenzo *et al.,* 2003; Ben Ayed *et al.,* 2001; Ben Ayed *et al.,* 2006).

Fluorapatite is a bioactive material which also has a low modulus elasticity in comparison with Co-Cr-Mo alloys (Finkelstein & Nancollas, 1980). Dental cobalt base alloys are biocompatible dental materials and have been widely used in dentistry (Craig, 2004). One of the primary aims of this research is to synthesize a novel Co-Cr-Mo alloy, fluorapatite nanocomposite by pulsed laser deposition (PLD) for dental coating applications. These nanocomposite coatings should exhibit time stability in simulated body fluid (SBF) solutions.

1.2.2. Hypothesis

For the purpose of this study the null hypothesis (H_0) is defined as the disproof of the results of the study and the alternative hypothesis (H_a) is defined as the acceptance of the results of this study.

- H_0: The nanocomposite coatings should not exhibit a high degree of corrosion resistance and an exceptionally long time time-stability in simulated body fluid (SBF).
- H_a: The nanocomposite coatings should exhibit a high degree of corrosion resistance and an exceptionally long time time-stability in simulated body fluid (SBF).

1.2.3. Aim of the study

The main goal of the proposed research project is to fabricate nanocomposite coatings by a versatile PLD technique based on dental Co-Cr-Mo alloy with different amounts of fluorapatite nanopowder using the PLD and evaluate their bioactivity and investigate how various fluorapatite content affected the biological properties of fabricated nanocomposites thin film.

1.3. Objectives of the study

The objectives of this study as follows:

(i) To synthesize fluorapatite nanopowder.

(ii) To synthesize - pure Co-Cr-Mo alloy and fluorapatite thins films.

(iii) To synthesize of Co-Cr-Mo alloy/fluorapatite nanocomposites.

(iv) To characterize and optimize of Co-Cr-Mo/fluorapatite nanocomposite thin-films.

Chapter 2

Literature Survey

2.1 Introduction

The purpose of this literature survey is to give a broad background relating to dental or bone replacement materials (particularly Fluorapatite, FA), and ceramic-matrix composites, along with a more in-depth examination of recent publications related to these and other thin films composites.

Detailed information relating to processing of deposition techniques and characterization; physical heat treatment chemistry, thermodynamics, and kinetics; mechanical property-structure relationships and testing techniques; and biological techniques and characterization will be included. This literature review first covers the nature of dental and the types of materials currently in use and under development that can replace bone and aid in its repair, etc.

2.2 Historical Overview of Dental Materials

Dental prosthetics, a field of dentistry, entails the replacement of missing teeth and related mouth or jaw structures with bridges, dentures or other replacement devices. the characteristics of functional dentures depend on various biological and technical factors. The main criterion for biocompatibility is corrosion resistance of the material in the environment of tissues and body fluids. Despite the many advantages of the introduction and application of implants in the oral environment, this application has always been associated with the prevention of corrosion and the effects of its occurrence in connection with its operation in the dynamic environment of the human body, which is particularly aggressive to metals (Kiel *et al.*, 2008; Budak *et al.*, 2012).

2.3 Types of Dental Alloys

Dental alloys can be categorized as noble alloys for example (gold- and palladium-containing) or base metal alloys for example (nickel- and cobalt containing alloys). Major (> 10 %at[3]) and minor (< 10 %at) components of these different alloy types are shown in Tables 2.1-2.4.

---

[3] %at is the atomic percentage.

2.3.1 Noble Alloys

Noble alloys are compositionally more diverse than high-noble alloys because of the included gold-containing alloys and those based on other elements such as palladium or silver. They are comprised of four groups: Au-Cu-Ag, Pd-Cu-Ga, Pd-Ag, and Ag-Pd. The Au-Cu-Ag noble alloys are similar in composition and metallurgy to the high-noble Au-Cu-Ag alloys. They were developed in the early 1980s when the price of gold significantly increased, making the high-noble counterparts too expensive. These alloys have a decreased gold content and compensate for the reduced gold by increasing copper, silver, or palladium. These alloys have moderate moduli of elasticity but are higher in hardness and yield strength than their high-noble counterparts. Depending on the amount of silver or copper present, Au-Cu-Ag alloys may be used in porcelain–metal applications but are more commonly used for full-cast restorations. The melting range of these alloys is lower than that of their high-noble counterparts if the copper or silver has been supplemented and the color of these alloys varies from yellow to reddish-yellow to silver depending how the reduced gold is compensated for in the composition. For example, alloys with 10 % or more of palladium have a silver color, whereas those with 20 to 30 % of copper are more reddish in color (Wataha, 2002a). Most often single-phase alloys, such as the Au-Ag-Cu alloys generally have poorer corrosion properties than their high-noble counterparts if the copper or silver has been increased to more than 15 % (Wataha & Lockwood, 1998).

2.3.1.1 Gold-containing noble alloys

The quantitative chemical compositions of the gold-containing noble alloys are shown in Table 2.1. These alloys have the longest history of use in dentistry and is *per se* the *standard* used when evaluating existing alloys. These gold-containing noble alloys are used for fabrication of inlays, crowns, partially fixe dentures, and metal ceramic restorations (PFM). Gold adds high corrosion resistance, good castability, good ductility and the distinctive yellow gold color. Silver reduces density, slowly whitens the alloy color when added in increasing amounts and counteracts the redness of copper. In PFM alloys, silver may discolor porcelain veneers. Copper, when present in the matrix, strengthens gold-containing alloys by forming $AuCu_3$. Both palladium and platinum increase casting

Table 2.1: The quantitative chemical composition Gold-containing Alloys.

Crowns and fixed partial dentures	Metal ceramic (PFM)
(1) Major: gold, silver, copper (2) Minor: palladium, platinum, zinc, indium, iridium, rhenium, germanium	(1) Major: gold, platinum, palladium (2) Minor: rhodium, silver, indium, tin, iron, iridium, rhenium, copper

temperature, strength, and corrosion resistance of the alloy (Tuccillo & Nielson, 1971). Palladium lowers cost and improves rigidity and sag resistance of PFM alloys (Moffa, 1983). Zinc (traces)[4] increases castability (Raub & Ott, 1983). Iron improves mechanical properties and, in PFM alloys, increases sag resistance (Kojima, 1980) and bond strength with porcelain (Espevik & Oilo, 1979). Tin acts as a bonding element in PFM alloys and a hardening agent in palladium-gold alloys, Iridium acts as a grain refiner in gold-containing PFM alloys (Raub & Ott, 1983). Indium serves as a bonding agent in PFM alloys (Espevik & Oilo, 1979). Germanium increases the castability of gold-copper alloys (Townsend & Hamilton, 1983).

2.3.1.2 Palladium-containing noble alloys

The quantitative chemical compositions palladium-containing noble alloys are shown in Table 2.2. Silver have been incorporated into the alloy matrices since 1974. In the early 1980s, there was an increase in palladium-containing formulations with reduced amounts of silver. They are used primarily for the fabrication of PFM restorations. However, a variety of type IV, extra-hard alloys exists can be used to cast inlays, crowns, fixed partial dentures and removable partial dentures (RPDs).

Table 2.2: The quantitative chemical composition palladium-containing noble alloys.

Crowns and fixed partial dentures	Metal ceramic (PFM)
(1) **Major:** palladium, silver, copper, gold (2) **Minor:** zinc, indium, iridium	(1) **Major:** palladium, silver, gold, copper, cobalt (2) **Minor:** gold, platinum, indium, tin, gallium, ruthenium, rhenium

Palladium reduces the cost of the alloy whilst increasing strength, rigidity and sag resistance (Moffa, 1983). Indium and/or tin is incorporated to improve bonding with the porcelain veneer. Gallium contributes to a homogeneous microstructure.

Ruthenium is used primarily as a grain refiner. Palladium containing alloys absorb small amounts of carbon that increase brittleness of the alloy (Eichner, 1983). Gas porosities (CO gas) may occur after the alloy is cooled. The palladium-silver alloys are somewhat more difficult to cast (McLean, 1983).

---

[4] When the element is present in mass/mass percentage less than 0.01% its concentration is referred to as trace.

Table 2.3: The quantitative chemical composition cobalt-containing base metal alloys.

Crowns and fixed partial dentures	Metal ceramic (PFM)
(1) **Major:** cobalt, chromium, nickel (2) **Minor:** molybdenum, tantalum, manganese, gallium, silicon, carbon, tungsten	(1) **Major:** cobalt, chromium, tungsten, molybdenum (2) **Minor:** copper, silicon, gallium, aluminium, nickel, tantalum, ruthenium

2.3.2 Base metal alloys

The quantitative chemical compositions of base metal alloys are shown in Tables 2.3 and 2.4. These alloys were first introduced in dentistry for the fabrication of RPDs in the early 1930s. Subsequently, these alloys have largely replaced the noble-containing alloys for RPDs. The most successful RPD alloys are those that contain cobalt-chromium, shown in Table 2.3, and those that contain nickel-chromium, shown in Table 2.4. There has also been an increase in the use of similar "base metal" alloys for application in the manufacture of less costly crowns, fixed partial dentures and PFM restorations due to the increase in price of gold and subsequently gold-containing dental casting alloys in the 1970s. (Morris *et al.*, 1992).

2.3.2.1 Cobalt-containing base metals alloys

The quantitative chemical compositions of base metal alloys containing cobalt are shown in Table 2.3. The alloys are primarily used in the fabrication of RPDs. Several manufacturers (e.g., J.F. Jelenko, Dentsply) have marketed cobalt-containing alloys for PFM restorations. Cobalt, when present in the matrix, provides strength, hardness, and corrosion resistance.

Chromium provides hardness and resilience and increases corrosion resistance when present in at least 16 %. Nickel increases ductility (Asgar & Peyton, 1961) while lowering melting temperature and hardness (Asgar & Allan, 1968). The carbon content of these alloys is critical. Since carbon is only slightly soluble in cobalt-chromium solid solutions, it is present mainly as dispersed carbides of chromium, cobalt or molybdenum, and these carbides increase the strength and hardness of the alloy (Tesk & Waterstrat, 1985). Manganese is a de-oxidizer and reacts with oxygen to form manganese oxide. Tungsten helps reduce the formation of chromium-depleted zones.

2.3.2.2 Nickel-containing base metal alloys

The quantitative chemical compositions of nickel-containing base metal alloys are shown in Table 2.4 and is used primarily for RPDs and PFM restorations. Nickel when present in the matrix, yields a softer alloy and hence causes a decrease in the melting temperature of the resulting alloy. Aluminum reacts with Ni to form Ni_3Al and an increase in strength and hardness results. Beryllium decreases melting temperatures and corrosion resistance (Lee *et al.*, 1985).

Table 2.4: The quantitative chemical composition nickel-containing base metal alloys.

Crowns and fixed partial dentures	Metal ceramic (PFM)	Removable partial dentures
(1) **Major:** nickel, chromium, iron	(1) **Major:** nickel, chromium	(1) **Major:** nickel, chromium
(2) **Minor:** molybdenum, silicon, manganese, boron, copper	(2) **Minor:** molybdenum, iron, silicon, manganese, beryllium, boron, aluminum, yttrium, tin	(2) **Minor:** molybdenum, iron, silicon, manganese, beryllium, boron, aluminum, carbon, cobalt, gallium, tin

While improving castability and bonding, lower melting temperatures also provide a smoother casting surface that requires less finishing. Boron decreases alloy-melting temperatures (Haudin & Perrin, 1981). Titanium and manganese increase corrosion resistance (Meyer, 1977) and serve as bonding agents (Espevik & Oilo, 1979). Iron increases strength (Meyer *et al.*, 1979). Cobalt increases hardness. Copper increases corrosion resistance (Bui & Dabosi, 1981). Yttrium aids in the adherence of oxide layers (Townsend & Hamilton, 1983). Molybdenum increases corrosion resistance (Lee *et al.*, 1985). Tin increases strength and hardness.

2.4 Classes of alloys currently available

Casting alloys are categorized in several ways, but the classification system most used by dental practitioners is the American Dental Association (ADA) compositional classification system. The ADA system divides casting alloys into three groups on the basis of mass/mass composition (Wataha, 2002c). The high-noble alloys are those with noble metal content (sum of gold, palladium, and platinum) of at least 60 % and a gold content of at least 40%. Most gold-containing alloys before 1975 were in this category.

The noble alloys must contain at least 25 % noble metal but have no specific requirement for gold content. Finally, the predominantly base-metal alloys contain less than 25 % noble metal, with no other specification on composition. The ADA also classifies alloys on the physical properties yield strength and elongation (Wataha, 2002c).

2.4.1 Alloys containing high concentrations of noble elements

High-noble dental casting alloys is shown in Table 2.5 and can be divided arbitrarily into those containing on (Au-Pt), (Au-Pd) or (Au-Cu-Ag). From these groups, the first two alloy types are appropriate for full-cast or porcelain–metal applications. The latter group is appropriate only for full-cast applications because of its higher silver and copper content and its lower melting range. The Au-Pt alloys are the newest of the high-noble alloys and were designed to avoid the use of palladium which became expensive and biologically controversial between 1995 and 1999. Both of these issues have since resolved, but this class of alloys is still available. These alloys are metallurgically complex because Au and Pt are not completely soluble in one another and are generally strengthened by a dispersed zinc phase. Some formulations contain silver to strengthen the alloy through solid solution hardening with gold. These alloys are white (silver) in color and have a moderately high melting range and moderate hardness, modulus, and strength. Because of their high noble-metal content (>97 %), they are curtly. The corrosion is highly variable depending on the phase structure and appropriate manipulation of the alloy by the laboratory. Au-Pt alloys are especially susceptible to overheating, which can disrupt the dispersed zinc phase and increase its corrosion significantly (Wataha, 2002a).

Table 2.5: Selected properties of the major types of alloys containing high concentrations of noble elements.

Type	Solidus-liquidus (°C)	Colour	Phase Structure	Elastic Modulus (static, GPa)	Vicker's Hardness (kg/mm^2)	Yield Strength (Tension, 0.2%, MPa)
Au-Pt (Zn)	1060–1140	Yellow	Multiple	65–96	165–210	360–580
Au-Pd (Ag)	1160–1260	White	Single	105	280	285
Au-Cu-Ag	905–960	White	Single	100	110	450

The Au-Pd alloys are a common type of high-noble alloy used in porcelain–metal and full-cast restorations but they are more common in porcelain–metal applications in Table 2.5. These alloys have moderate strength, elastic moduli, and hardness and have a moderately high melting range. The Au-Pd composition is at times supplemented with silver to increase the physical properties via solid solution hardening with gold and palladium. Au-Pd alloys are mostly single-phase alloys and are white in color when the Pd concentrations are greater than 10% (Wataha, 2002a). Corrosion of these alloys is low in biologic environments, even at low pH or during tooth brushing (Wataha *et al.*, 1998; Gerstrofer *et al.*, 1991).

The Au-Cu-Ag high noble alloys are shown in Table 2.6, and have a long history of use in dentistry for full-cast restorations (they are compositionally equivalent to the old type III casting alloys). The alloys generally are yellow in color and have moderately high yield strengths and hardness but only moderate elastic moduli. Because copper and silver are miscible with gold, these alloys are almost always single phase, which makes them easy to cast and solder. They also can be heat hardened by heating to about 600flC and then letting the alloy cool to room temperature slowly (Wataha, 2002a).

2.5 Predominantly base-metal alloys

The base-metal alloys can be arbitrarily divided into four groups: Ni-Cr- Be, Ni-Cr, Ni-high-Cr, and Co-Cr (*see* Table 2.6). The first three groups are closely related in composition and many physical properties but are fundamentally different in their corrosion properties. These alloys may be manufactured with or without trace amounts (0.1 %) of carbon. When used for cast restorations, these alloys generally do not contain carbon. However, when used for partial denture frameworks, carbon is generally added and is a potent enhance of yield strength and hardness, but not modulus (Baran, 2002).

All alloys of this group may be used for full-cast or porcelain–metal restorations, and all are silver in color. From the standpoint of porcelain application, these alloys all form heavy, dark oxide layers that are more difficult to aesthetically manage than those formed by alloys in the noble and high-noble alloy groups. The base-metal alloys share high physical properties, and these alloys have the highest moduli of any alloys used for cast restorations. They are all equally difficult to solder because of their propensity for formation of surface oxides. The nickel-containing alloys in this group may have chromium contents of approximately 14 % with (Ni-Cr-Be) or without (Ni-Cr) beryllium (Table 2.6).

Beryllium is primarily used to lower the melting range of the alloy to a point where gypsum-bonded investments can be used for casting (Wataha, 2002a). Although beryllium is advantageous in terms of casting manipulation of this alloy by the laboratory, the Ni-

Cr-Be alloys corrode more easily than the non-Be alloys (Bumgardner & Lucas, 1993). This corrosion is particularly evident in acidic environments. In some studies, the amount of nickel released from these alloys in an acidic environment in 30 minutes is more than that released in 1 year in a neutral environment (Wataha *et al.*, 1998). The Ni-high-Cr alloys are the most corrosion resistant of the Ni-containing group and have Cr contents of over 20 %. These alloys are the most common of the Ni-containing alloys used in Europe. The corrosion of these alloys is far better than the Ni-Cr-Be alloys but not as good as many alloys in the noble or high-noble groups. The common hypersensitivity to nickel (10% to 20% by most estimates (Hildebrand *et al.*, 1989). makes use of any of the Ni-containing alloys a higher biologic risk than many others.

Table 2.6: Selected properties of major types of predominantly metal-containing alloys.

Alloy type	Solidus-liquidus (°C)	Color	Phase structure	Elastic modulus (static, GPa)	Vicker's hardness (kg/mm^2)	Yield strength (tension, 0.2%, MPa)
Ni-Cr-Be	1160-1270	White	Multiple	192	350	325
Ni-Cr	1330-1390	White	Multiple	159	350	310
Ni-high-Cr	1250-1310	White	Multiple	205	205	180
Co-Cr	1215-1300	White	Multiple	155	155	390

Co-Cr alloys, shown in Table 2.7, are the most common base-metal alternative for patients allergic to nickel Unfortunately, cobalt is the second-most common metal allergen, and cobalt allergy should be ruled out before these alloys are substituted for nickel-containing alloys. With the exception of titanium-containing alloys, the Co-Cr alloys have the highest melting ranges of the casting alloys, and laboratory manipulation (casting, finishing, and polishing) of these alloys is difficult. The surface oxide of Co-Cr alloys is particularly difficult to mask, and the compatibility of coefficients of thermal expansion between these alloys and porcelains may be problematic.

2.6 Alloys exhibiting biocompatibility

Biocompatibility is best described as how an alloy interacts with and affects biologic systems. Although the interactions between an alloy and tissues may take many forms, the release of elements from the alloy into the oral cavity is a primary focus of alloy biocompatibility because most adverse biologic effects, such as allergy or inflammation, have been attributed to such release (Hanks *et al.*, 1996; Wataha, 2000). In this sense, biocompatibility is related to the corrosion of an alloy. However, care must be taken not to assume poor biocompatibility on the basis of elemental release alone because the ability of tissues to tolerate this element release varies widely (Wataha & Lockwood, 1998). One common misperception of dental casting alloys is that they may be inert in the oral environment.

The placement of a material into the oral cavity creates active interfaces through which the body affects the material and the material affects the body. Regardless of the material placed, these interactions occur. Thus, inertness of dental casting alloys is not possible.

Furthermore, the interactions that occur are dynamic and may change as the environment of the interface changes. For example, the development of periodontal inflammation changes in occlusal loading, or a change in diet may alter the way the alloy and oral tissues interact. Additional research is needed in this area. The biocompatibility of alloys may have legal implications for dental practitioners. Litigation by patients over issues of biocompatibility is rare but usually involves reactions of taste, inflammation, or infection from elemental release from casting alloys (Wataha, 2000). These allegations by patients are difficult to prove conclusively but can be avoided altogether by careful selection and proper manipulation of the alloys by laboratories and the practitioner. Procedures such as casting, soldering, polishing, or porcelain application may alter the nominal corrosion properties of casting alloys and their biologic behaviour if these procedures are improperly performed (Wataha, 2002a; Baran, 2002 & Wataha, 2000).

Furthermore, alloys within each of these groups are diverse and the practitioner faces a wide array of choices. Because of the long-term role these materials play in dental treatment, the selection of an appropriate alloy is critical from technical, ethical, and legal perspectives. Although uses for pure metals such as gold foil and platinum foil exist in dentistry, the main role for metals in dentistry has been in alloys. Alloys are used for fixed prostheses rather than pure metals because pure metals do not have the appropriate physical properties to function in these types of restorations. For example, the tensile strength of pure gold is 105 MPa. By adding 10 % of copper, this strength increases to 395 MPa (Wataha, 2002). With the appropriate addition of other elements and proper casting conditions, the strength increases to over 500 MPa. Even more impressive is the increase in hardness: from 28 kg/mm^2 for pure gold to nearly 200 kg/mm^2 for a typical gold-containing casting alloy.

Thus, the use of alloys provides physical and biologic properties that are required for successful, long-term fixed prostheses.

2.7 Properties of Alloys Important to Clinical Performance

A few properties of dental alloys are important to their clinical performance.

2.7.1 Colour

Colour seem to be an obvious such property of choice for most patients, the color of alloys is often described as being "yellow" or "white." These limited terms are inadequate because the range of alloy colors is much greater, encompassing reddish, brownish, and even greenish tints. Furthermore, the term "white" is a metallurgical term that does not describe the silver color ascribed to these alloys by most clinicians and patients. In any case, the color of casting alloys has little to do with the physical, chemical, dental, or biologic performance of the alloy (Wataha, 2001).

2.7.2 Phase Structure

When metals and non-metals are mixed to form an alloy, it has varying degrees of solubilities in each other (Wataha, 2002b).

The ability of elements to dissolve in each other is similar to compounds encountered in everyday life such as alcohol and water or vinegar and oil. If most of the components of the alloy dissolve in one another, the alloy is described as a single-phase alloy and has a more or less homogeneous composition throughout. If one or more components are not soluble in the other, then two or more phases form in the solid state, each having a different composition. In this case, the alloy is described as a multiple-phase alloy.

Single-phase alloys are generally easier to manipulate (i.e. easier to cast) and have lower corrosion rates than multiple phase alloys (Wataha, 2001). However, multiple-phase alloys may be etched for bonding and may be significantly stronger than single-phase alloys (Wataha, 2002c). Before 1975, the majority of alloys were single phase, being containing on gold, which is miscible with silver, copper, and palladium (Wataha, 2002).

2.7.3 Grain Size

A second important microstructural feature of casting alloys is its grain size. Grains are crystals of the alloy that form upon solidification from small nuclei, such as ice crystals form from water. As an alloy cools from the liquid state, these crystals grow until they meet each other at boundaries called grain boundaries. The size of the grains is influenced by factors such as the cooling rate of the alloy, the presence of special nucleating elements such as iridium, heat treatment after casting, and the composition of the alloy (Flinn &

Trojan, 1986). For gold-containing alloys, a small (<30 µm) grain size has been shown to improve tensile strength and elongation (Neilson & Tuccillo, 1966). For base-metal alloys, small, dispersed secondary phases (each with a small grain structure) are critical to the strength of the alloys. In other base-metal alloys, the grains are large and may approach 1 mm in diameter (Baran, 2002). These large grains, which do not have anisotropic properties, may be a clinical liability if it occurs in critical areas such as the connectors between units of a multiple-unit fixed restoration. (As with phase structure, grain structure is not visible to the naked eye).

2.7.4 Strength and hardness

The compressive strength of all dental casting alloys is sufficiently high that it is not a consideration for clinical performance; however, tensile strength varies considerably among alloys. A tensile strength above 300 MPa is necessary to avoid fracture of alloys in high-risk areas such as between poetics of a multiple-unit fixed restoration (Wataha, 2002a). Because tensile strength is difficult to measure in practice, most manufacturers cite yield strength instead. The yield strength in tension is the stress required to permanently deform an alloy by a given amount, expressed as a percentage of the length of the specimen being tested. This percentage "offset" (normally 0.1% or 0.2%) indicates a permanent deformation of the alloy and is relatively reproducible. Information on yield strength is easily obtainable from the manufacturer. The hardness of an alloy must be sufficient to resist wear from opposing teeth or restorations and not so hard as to wear enamel (which has a Vickers hardness of 340 kg/mm^2) (Wataha, 2002c). In practice, a Vickers hardness less than 125 kg/mm^2 makes an alloy susceptible to wear, and hardness greater than enamel may wear existing teeth (Wataha, 2002a).

However, wear is a complex phenomenon, and predicting clinical wear containing on hardness alone is not advisable (Kohn, 2002). Information on hardness is commonly available from manufacturers.

2.7.5 Corrosion

Perhaps no property has captured as much attention in recent years as alloy corrosion. The degree of corrosion, which results when one or more components of the alloys is oxidized, is critical to the long-term success of a fixed prosthesis for several reasons. Corrosion may compromise the strength of the restoration, leading to catastrophic failure (Wataha, 2002a) or the release of oxidized components may discolour natural teeth, porcelain veneers or even the soft tissues in severe cases (Wataha, 2000). Corrosion may reader the restoration itself aesthetically unacceptable because due the formation of pits or colored patinas. The electrons released during corrosion may be detectable by the patient as a shock (galvanic corrosion) that can be disconcerting and even debilitating.

Released metallic components may cause an undesirable metallic taste leading the patient request that the restoration be removed. The measurement of corrosion is complex and although many investigators have tried to predict corrosion of an alloy containing on its composition, such predictions are complex at best. Corrosion may be quantified by measuring the current flow associated with metal oxidation or the concentrations of released metals. These measurements may be made under a variety of conditions *in vitro* or, some cases, *in vivo*. Although corrosion is clearly visible to the naked eye when it is severe (such as rust on iron), most corrosion of dental casting alloys is insidious and invisible to the naked eye. Manufacturers of alloys need to measure corrosion by specific (ASTM or ISO) standards to gain appropriate certification of them. This information is usually available from manufacturers, reported in brochures. Because corrosion generally results in the release of mass from the alloy into the oral environment, it is related in complex ways to alloy biocompatibility (Wataha, 2000).

2.7.6 Alloy solidus and fit

The shrinkage properties of alloys force the practitioner to consider this property. When a molten alloy solidifies from the liquid state during casting, a large amount of shrinkage occurs but this is compensated for by the addition of molten metal from the reservoir in the casting ring. However, once all of the metal in the restoration has solidified, the shrinkage as the alloy cools from its solidus to room temperature cannot be compensated for by the addition of liquid. If the dimensions of the hot casting were the right clinical size, the final cooled casting would be too small because of this shrinkage. The higher the solidus temperature, the more shrinkage occurs. These shrinkage values range from about 0.3 % to 0.5 % for high-gold alloys with solids of about 950flC to nearly 2.5 % for nickel- and cobalt-containing alloys with solids of 1300°C to 1400°C (Wataha, 2002d). The shrinkage must be compensated for by expansion of the die; application of die spacers; the use of special expanding investment mechanisms; or, increasing the burnout temperature of the investment. The risk of ill-fitting crowns is much greater for alloys with high solids and this factor is a significant consideration in the choice of alloys.

2.8 Co-Cr-Mo alloys

Co-Cr-Mo alloys are actually found very wide in the prosthodontics implants, crown of a tooth, bridgework and full cast partial (Reimann & Dobrzański, 2011; Dobrzański, 2007).

Fixed prosthesis, no matter the form, was introduced into human oral cavity over many years, after body implantation, user demand from prosthesis should all the time be resistance on stresses, characterized good hardness, biotolerance characterized and corrosion resistance in environment in which they work (Walke *et al.*, 2006). Corrosion resistance is one of the meaningful property because it's influence on possible allergy and other inflammation conditions in oral cavity environment (Sharma *et al.*, 2008).

Materials selection on dentures is usually linked with the determination of the corrosion resistance and some mechanical properties because chosen metals must consider these two criteria (Upadhyay *et al.*, 2006; Manaranche & Hornberger, 2007). Many scientists in their work with biomaterials and also the use in prosthodontia, considered anticorrosion protection and either criteria almost connected with mechanical properties (Zupancic *et al.*, 2006). It is therefore important to take note of the results of research and pay attention on way which samples were preparation. Because of the many alloys used for dentures some authors decided to try to find some relationship in Co-Cr-Mo alloys between chemical composition and corrosion resistance or its influence on hardness.

Co-Cr-Mo alloys are typical non-magnetic metallic biomaterials because have abrasive and corrosion resistances in chloride environments, therefore it has a proven track record as materials for artificial hip and knee joints (Bauer *et al.*, 2012; Mori *et al.*, 2010). The corrosion resistance is related to surface oxide formation which is strongly enriched with Cr_2O_3 (Bauer *et al.*, 2012). The alloy was developed by Haynes E., as Stellite, in 1913. In 1930, an alloy containing on Co was patented as Vitallium and used for aircraft engines, and in the same period it was also used in dental medicine. A decade later, it was used for orthopedics. The original specification of the alloy contains 30 % Cr, 7 % W and 0.5 % C. Later tungsten has been replaced by 5 % Mo for changing the grain size and for increasing corrosion resistance (Milošev, 2009). Alloying of other elements such as nickel, molybdenum, or tungsten improve their mechanical properties and abrasion resistance (Bauer *et al.*, 2012).

Until present, the alloy composition has not changed significantly. The largest change was related in the area of carbon content due to better homogenization of hard carbide grains and increase abrasion resistance (Milošev, 2009). Generally, these alloys exhibit higher mechanical properties and higher corrosion resistance compared to steels. Large differences exist in the mechanical properties between cast and wrought (forged, ISO[5] 5832-12) alloys, as well as between low and high-carbon containing alloys. Co alloys are divided by carbon content:

- Low carbon (up to 0.08 %) - wrought

---

[5] ISO International Standards Organisation.

- High carbon (up to 0.2 %) - wrought and cast (Bauer *et al.*, 2012).

The most used as-cast alloys are Co-Cr-Mo (ISO 5832-4, ASTM F75) (Table 2.7). The rapid solidification, because it may result in large dendritic grains causing the yield strength reduction. Moreover, casting defects such as inclusions and microspores cannot be avoided and may act as stress risers and thereby result in the overall decrease of the fatigue strength of the material (Bauer *et al.*, 2012). Generally, the cast alloy is characterized by an inhomogeneous structure, larger grains, cored microstructure (Milošev, 2009).

Table 2.7: Chemical composition in % of Co-Cr-Mo alloys. Bal is the balance and Tol is the tolerance.

Element	Co-Cr-Mo					Co-Cr-Mo			
						ISO 5832-12			
	ISO 5832-4		ASTM F75			Low carbon		High carbon	
	Min	Max	Min	Max	Tol	Min	Max	Min	Max
Cr	26.5	30.0	27.00	30.00	±0.30	26.0	30.0	20.0	30.0
Mo	4.5	7.0	5.00	7.00	±0.15	5.0	7.0	5.0	7.0
Ni	-	1.0	-	0.50	±0.05	-	1.0	-	1.0
Fe	-	1.0	-	0.75	±0.03	-	0.75	-	0.75
C	-	0.35	-	0.35	±0.02	-	0.14	0.15	0.35
Mn	-	1.0	-	1.00	±0.03	-	1.0	-	1.0
Si	-	1.0	-	1.00	±0.05	-	1.0	-	1.0
W	-	-	-	0.20	±0.04	-	-	-	-
P	-	-	-	0.020	±0.005	-	-	-	-
S	-	-	-	0.010	±0.003	-	-	-	-
N	-	-	-	0.25	±0.02	-	0.25	-	0.25
Al	-	-	-	0.10	±0.02	-	-	-	-
Ti	-	-	-	0.10	±0.02	-	-	-	-
B	-	-	-	0.010	±0.002	-	-	-	-
Co	-	bal	-	Bal	-	-	bal	-	Bal

Larger grains can be reduced by subsequent hot isotactic pressing up to 8 μm (Bauer *et al.*, 2012; Milošev, 2009).

This operation is usually classified by precision casting and reduces the porosity of the alloy (Losertová, 2012). Another possibility of how to improve the mechanical properties (Table 2.8) is the homogenization heat treatment (Bauer *et al.*, 2012). The as-cast alloys have a microstructure consisting of a dendritic matrix α (Co *fcc*) Cr-rich or Mo-rich. The dendritic regions contain Co, while the interdendritic regions and the grain boundaries may consist of different phases (due to the higher carbon content majority of carbides $M_{23}C_6$) Co-rich or Cr- and Mo-rich (Bauer *et al.*, 2012; Milošev, 2009; Ramírez-Vidaurri *el al.*, 2008).

These extremely hard carbides precipitates increase the wear resistance of alloy (Bauer *et al.*, 2012; Milošev, 2009). A combination of high hardness and compression strength is the basis for their applications in joint replacements, but they are less important for fixation devices (Milošev, 2009). The implants are manufactured by mechanical processing, powders metallurgy and investment casting process (Ramírez-Vidaurri *et al.*, 2008). The Co-Cr-Mo as-cast alloy conforming to the ISO 5832-4 standard is widely used in the manufacturing of orthopedic implants with in- vestment casting techniques (Giacchi *et al.*, 2010).

2.9 Coating techniques of thin film PLD

2.9.1 Pulsed laser ablation

Pulsed laser deposition (PLD) is a technique in which a layer of target material[6] is deposited on a substrate such as an alloy or glass. The photon energy of a laser, characterized by pulse duration and laser frequency, interacts with the bulk material (Chrisey & Hubler, 1994). As a result, material is removed from the bulk, depending on the absorption properties of the target materials and deposited on the substrate. The principle of PLD is shown in Figure 2.1a. A laser pulse is focused onto the surface of a target (solid or liquid) in a vacuum chamber and thereby removes material. A significant removal of materials occurs above a certain threshold power density and the ejected, partially ionized material forms a luminous ablation plume. The threshold power density required to create such plasma depends on the absorption properties of the target material, the laser wavelength, and pulse duration. The typical pulse length for an excimer laser is of 10 ns. In the case of femtosecond excimer lasers, it is in the range of 500 fs. The removed material is directed towards a substrate where it recondenses to form a film. The growth kinetic of such films depends on the material flux, repetition rate, growth temperature, substrate material, pressure, and background gas (vacuum, reactive). To enhance the reactivity of the background gas with the ablated species, either a RF (radio-frequency)-plasma source (Braic *et al.*, 2007), shown in Figure 2.1b, or a gas pulse configuration (Willmott *et al.*, 1997), shown in Figure 2.1c, are used. An interesting development from

---

[6] Also called the bulk material.

conventional laser ablation is pulsed reactive crossed beam laser ablation (PRCLA, *see* Figure 2.1c).

The main feature of PRCLA is the interaction between the ablated plume and a pulsed gas. The purpose of the pulsed gas valve is to use a reactive gas when transfer and deposition of material occurs but also to provide a higher partial pressure during the interactions, yet to maintain a defined and low background pressure. This can be achieved experimentally by using a distance of at most 1 cm between the nozzle and the ablation point on the target, which results in a strong degree of scattering between the gas and the plume species also called interaction region (*see* Figure 2.1c).

After passing the interaction region, the initial two beams merge and expand together almost collision-free while maintaining their reactivity for the film growth (Wang *et al.*, 1994). One application of the gas pulse is to provide more reactive oxygen by injecting N_2O into the laser plume. As a result, the oxygen content in an oxide film can be improved (Montenegro *et al.*, 2006).

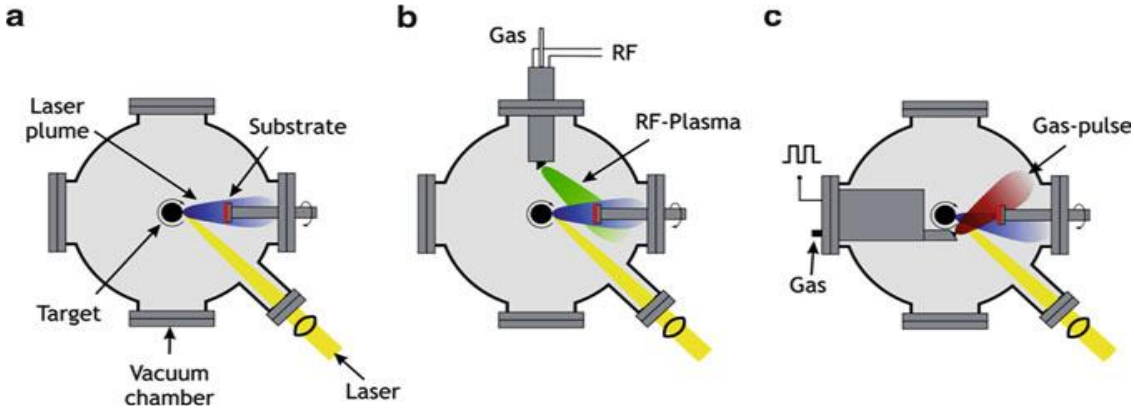

Figure 2.1: (a) Illustration of a simple pulsed laser deposition (PLD) process. The incoming laser beam is focused onto a target, thereby vaporizing the material of the surface region. The ejected material is partially ionized and forms the ablation plume that is directed towards the different substrate. (b) Schematic of a RF-plasma enhanced PLD (Braic *et al.*, 2007). (c) Typical view schematic of a gas-pulse set-up combined with PLD also known as pulsed reactive crossed beam laser ablation (PRCLA) (Willmott *et al.*, 1997). The two beams merge after passing the interaction zone and expand together.

In general, the idea of PLD is simple. A pulsed laser beam is focused onto the surface of a solid target. The strong absorption of the electromagnetic radiation by the solid surface leads to rapid evaporation of the target materials. The evaporated materials consist of highly excited and ionized species. They presented themselves as a glowing plasma plume immediately in front of the target surface if the ablation is carried out in vacuum. Typical plasma plumes produced during PLD process are shown in Figure 2.2.

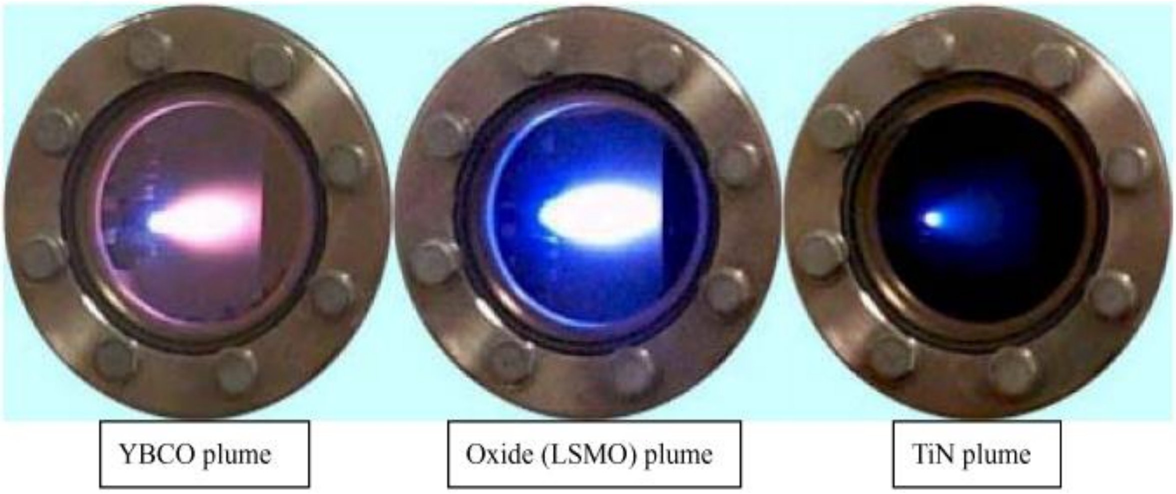

Figure 2.2: Typical plasma plumes production for various ceramic materials during PLD irradiation process.

2.9.2 Advantage and disadvantage of pulsed laser deposition

2.9.2.1 Advantages of pulsed laser deposition for thin film growth

To use PLD for thin film growth has advantages for a number of reasons:

- The flexibility in wavelength and power density allows to ablate almost any material or materials combination.
- The laser is not part of the vacuum system. Therefore, a considerable degree of freedom in the ablation geometry is possible.
- The use of a pulsed laser beam enables a precise control over the growth rate.
- The congruent transfer of the composition can be achieved for most ablated material or materials combinations.

Moderation of the kinetic energy of evaporated species to control the growth properties and growth modes of a film (Willmott & Huber 2000).

2.9.2.2 Disadvantages of pulsed laser deposition for thin film growth

Disadvantages in the use of PLD can be of a technical nature, or intrinsic to the ablation process and the electromagnetic interaction between photons and matter:

- The large kinetic energy of some plume species causes re-sputtering and likewise defects in the substrate surface and growing film.
- An inhomogeneous energy distribution in the laser beam profile gives rise to an inhomogeneous energy profile and angular energy distribution in the laser plume.
- Light elements like oxygen or lithium have different expansion velocities and angular distributions in a plume as compared to heavier elements. Therefore, an addition source to supplement these elements to obtain the desired film composition is required, e.g., adequate background gas[7] or an adapted target composition.
- Due to the high laser energies involved, macroscopic and microscopic particles from the target can be ejected which can be detrimental to the desired properties of films and multilayers.

The latter point can partially be overcome by working with very dense polycrystalline or even single crystalline targets, but it also depends on the absorption and mechanical properties of the target material and laser fluence used (Willmott & Huber 2000).

2.10 Initial ablation processes and plume formation

When a photon interacts with matter, the photon energy is coupled to the lattice through electronic processes. The photon absorption by a material occurs in general over an optical depth of several nanometers where the energy in metals is transferred to the electronic system directly and in nonmetallic systems typically to the lattice. Electronic relaxation processes are very fast with a typical lifetime of 10^{-14}–10^{-13} s. For metals it has been shown, that the time scale for the electron energy transfer to the lattice is of the order 1.5 pico seconds and strongly dependent on the thermal conductivity, specific heat, and electron–phonon coupling (Wang *et al.*, 1994).

For nonmetallic systems, the relaxation time varies between 10^{-12} and 10^{-3} s. Here, the absorption process occurs on a much shorter time scale compared to the thermal diffusion process, which gives rise to vaporization and plasma formation during the time scale of the pulse duration. The vaporization process can be described by the heat flow theory where the surface temperature of the target at the end of the laser pulse is determined by the light absorption and thermal diffusivity. It is therefore expected that the laser ablation mechanisms for nanosecond and femtosecond ablation are different (Wang *et al.*, 1994).

---

[7] A background gas is used to reduce the kinetic energy of the plume species and to increase the number of chemical reactions between the plume and gas molecules and in so doing form N and O and diatomic species.

2.10.1 Femtosecond laser irradiation

The use of femtosecond (fs) pulse in the ablation process, and in particular for nanoparticle synthesis, has been successfully demonstrated (Amoruso *et al.*, 2005). The fs ablation has several advantages compared to longer pulse lengths. First, for a given fluence, higher temperatures and pressures are obtained as compared to ns ablation because the laser energy is delivered before significant thermal conduction occurs. Second, there are no secondary interactions between the laser beam and the ablated material. A higher photon density also means a larger kinetic energy for plume species due to the so- called Coulomb explosion. This is often detrimental for thin film growth as a result of a high-energy ion bombardment of the substrate and growing film. In addition, nanoparticle formation is observed (Amoruso *et al.*, 2005).

2.10.2 Nanosecond laser irradiation

Irradiating a solid with a nanosecond (ns) pulse, there is enough time for a thermal wave to propagate into the bulk material thereby causing a melting and evaporation of the material. Two dominant mechanisms are involved in the plume absorption, i.e., inverse Bremsstrahlung and photoionization.

These phenomena induce vapor ionization and excitation through collisions with excited and ground state neutrals. Nanosecond ablation of metals and ceramics may result at high fluences in the formation of a liquid phase, which is the reason for the ejection of droplets which are embedded in a film. These drawbacks can be reduced and ns lasers are nowadays a useful tool to grow a large variety of materials.

When PLD is performed under vacuum conditions, two main aspects are different from sputtering or conventional thermal evaporation techniques. First, pulses of high vapor fluxes (˜1 ms) are separated by periods of no vapor flux (˜100 ms). Second, relatively high vapor arrival energies at the substrate. There may be ions with energies up to the keV range and neutral atoms with energies of several eV.

When PLD is performed in the presence of a background gas like oxygen, two effects are expected during the film formation: (a) the reduction of the kinetic energy of the vapor flux, (b) it provides a high flux of background oxygen molecules bombarding the surface during deposition. This high flux could change the film and substrate surface energies and will increase the oxygen content, like in oxide thin films. Changing the background gas to other gases such as NH_3 to provide reactive nitrogen, the composition of a film can be substantially changed (Marozau *et al.*, 2009).

2.11 Thin film growth

Growing oxide thin films involves a number of requirements. Often, epitaxial growth of a material is preferred and therefore the choice of the appropriate substrate material is important. Basic requirements are a good crystallographic lattice match between film and substrate, the substrate material should be chemically compatible to the film, it should have comparable thermal expansion coefficients, and a thermodynamically and chemically stable surface. Essential for some applications is to choose selectively the chemical termination of the surface (Kawasaki *et al.*, 1994 & Koster *et al.*, 1998).

2.12 Materials Characterization Techniques

2.12.1 X-Ray diffraction (XRD)

X-Ray diffraction (XRD) is a versatile, non-destructive technique that reveals detailed information about the chemical composition and crystallographic structure of natural and manufactured materials (Cullity, 1978). The X-ray diffraction method provides qualitative and quantitative analysis for all types of materials *in situ* and *ex situ* measurements possible.

Qualitative analysis yields the identification of phase or phases in a specimen by comparison with the reference pattern (i.e. data collected by someone else), and relative estimation of proportions of different phases in multiphase specimens by comparing peak intensities attributed to the identified phase. The quantitative analysis of diffraction data involves the determination of amounts of different phases in multi-phase samples. Quantitative analysis, an attempt is made to determine structural characteristics and phase proportions with quantifiable numerical precision from the experimental data itself. The most successful quantitative analysis usually involves modeling diffraction pattern such that the calculated pattern(s) duplicates the experimental one. All quantitative analysis requires precise and accurate determination of the diffraction pattern for a sample in terms of both peak positions and intensities. In some kinds of analysis (i.e. particle shape and clay structure) rely on the existence of preferred orientation, most require a uniformly sized, randomly oriented fine (ideally 1-2 μm) powder specimen to produce intensities which accurately reflect the structure and composition of the phase(s) analysed (Cullity, 1978).

2.12.2 Scanning Electron Microscope (SEM)

Scanning electron microscopy (SEM) is a type of electron microscope, which is used for various purposes:

- Topographic studies
- Microstructure analysis
- Chemical composition
- Elemental mapping
- Elemental analysis if equipped with appropriate detector (energy/wavelength dispersive X-rays).

For the SEM analysis, a focused beam of high-energy electrons is required to generate a variety of signals at the surface of solid specimens. The signals that derive from electron sample interactions reveal the hidden information about the sample including external texture (morphology), chemical composition, and crystalline structure, and the orientation of materials making up the sample (Hussain, 2009).

In SEM, primary electrons are filled emitted by cathode filament (W or LaB6) or filed emission gun (W-tip) and after that accelerated with high energy typically 1- 30KeV. An electron beam is steered with scanning coils over the area of the interest. During the interaction of the beam with material, the primary electrons decelerate and lose their energy by inelastic transfer to the other atomic electron and to the lattice. Due to continuous scattering events the primary beam spread up with different energies depending on origin source and the interaction volume with the various electrons emitted and their respective energy (Hussain, 2009; Postek *et al.,* 2001; Goodhew *et al.*, 2001).

2.12.3 Energy-Dispersive Analysis of X-Rays Spectroscopy (EDAX)

The EDAX system is connected to electron microscopes such as SEM, FE-SEM and HR-TEM. EDAX spectra of the corresponding elements of the sample are obtained by measuring the energy of x-rays emitted from the sample during e-beam bombardment. X-rays are produced as a result of ionization of an atom when the incident electrons have removed an inner shell electron.

When an ionized atom returns from its excited state to its ground state, an electron from a higher energy outer shell fills the vacant inner shell and then releases an amount of energy equal to the potential energy difference between the two shells. This energy, which is unique for every atomic transition, will be emitted either as an X-ray or as Auger electron. In EDAX analysis, the detector analyses these emitted X-ray photons from the sample, which can be utilized for quantitative and qualitative composition analysis (Postek *et al.,* 2001; Goodhew *et al.,* 2001).

2.12.4 Atomic Force Microscopy (AFM)

The atomic force microscope (AFM) or scanning force microscope is a very high resolution type of scanning probe microscope, with the demonstrated resolution of fractions of nanometre. It is more than 1000 times better the optical diffraction limit. In tapping mode, the cantilever is driven to oscillate up and down at near its resonance frequency by a small piezoelectric element mounted in the AFM tip holder (Binning *et al.,* 1986). The AFM has many advantages compared to scanning electron microscope (SEM).

The scanning electron microscope provides a two-dimensional projection or a two-dimensional image of a sample, the AFM provides a three-dimensional surface profile. The AFM has the disadvantage in image size compared to SEM. The SEM can image an area approximately square millimeters with a depth of field in the range of millimeters. The AFM can only image a maximum height approximately micrometres and a maximum scanning area of around 150 by 150 micrometres (Binning & Smith 1986).

Of importance in the AFM analysis is the quantification of the topography, that is, extent of homogeneity of the deposition. This homogeneity can be quantified in terms of the averages and median heights of the peaks, the roughness, and the standard deviation of the average height, the root mean square value of the roughness. Also of importance is the valleys that were formed during the deposition. Illustrations of peak and valley have been performed (Raposo *et. al.,* 2007; De Oliveira et. al., 2015).

For the purpose of this study the surface area is expressed as an (x, y) component and the peak height as the *z* component; thus the peak height is given by *z*(x, y), and for simplicity expressed as *z*. The average peak height is denoted by $\bar{z}$, the roughness is denoted by R_a, the mean roughness by R_m, the value that is in the "middle" of the distribution, with 50% of the scores having a value larger than the median, and 50% of the scores having a value smaller than the median, and the root mean square value by R_q. The formula for calculating the average height of the peaks, and for each of these parameters are given in equations 1.

$$\begin{aligned} \bar{z} &= \frac{1}{n}\sum_{x=1}^{n} z \\ R_m &= mean\ of\ z \ldots\ldots\ldots\ldots (a) \\ R_a &= \frac{1}{n}\sum_{x=1}^{n}(z-\bar{z}).\ldots\ldots\ldots (b) \\ R_q &= \sqrt{\frac{1}{n}\sum_{x=1}^{n}(z-\bar{z})} \ldots\ldots (c) \end{aligned} \qquad (1)$$

R_a and R_q are important parameters when determining the amplitude. In addition, R_q is an indication of the temporal changes that are experienced when a new surface layer is formed and of the spatial differences.

The number of peaks compared to the number of valleys is expressed by R_s, given in equations 2. c_p is the number of peaks and c_v is the number of valleys. Hence, it is a

$$\begin{aligned} &R_s = \frac{1}{n(R_q)^3}\sum_{i=1}^{n}(z_i - \bar{z})^3 \\ &R_s = 0 \Rightarrow c_p = c_v \dots\dots\dots\dots\dots\dots..(a) \\ &R_s > 0 \Rightarrow c_p > c_v \dots\dots\dots\dots\dots\dots.(b) \\ &R_s < 0 \Rightarrow c_p < c_v \dots\dots\dots\dots\dots\dots..(c) \end{aligned} \qquad (2)$$

measure of the profile symmetry about the mean line. For a value of zero, the height distribution is symmetrical or Gaussian. However, if the height distribution contains more peaks than valleys, then R_s is positive, and negative when the surface more planar and the valleys are predominant.

The sharpness of the surface is given by the Gaussian distribution and is denoted by R_k and given in equations 3. R_k thus corresponds to a measure of surface sharpness; when $R_k = 3$, then the distribution of the peaks and the valleys is Gaussian. Other cases for the value of R_k are given in the equation.

$$\begin{aligned} &R_k = \frac{1}{n(R_q)^4}\sum_{i=1}^{n}(z_i - \bar{z})^4 \\ &R_k = 3 \Rightarrow Gaussian\ distribution, mesokurtic \dots\dots\dots\dots\dots..(a) \\ &R_k > 3 \Rightarrow c_p > c_v \dots\dots\dots\dots\dots\dots\dots\dots\dots\dots\dots\dots\dots\dots\dots.\dots\dots\dots.(b) \\ &R_k < 3 \Rightarrow Surface\ is\ flat,\ platykurtic \dots\dots\dots\dots\dots\dots\dots\dots..(c) \end{aligned} \qquad (3)$$

The topography of the specimen can also be influenced by various artifacts (Raposo *et al.,* 2007, and references therein). In this study, Fourier filtering was applied and then the values of the parameters indicated in equations 1 to 3 were determined.

2.13 Analytical Techniques for Mechanical Properties

2.13.1 Fluorapatite

Fluorapatite, $Ca_{10}(PO_4)_6F_2$ is a widely spread form of calcium phosphate present particularly in biological material. Human hard tissues contain crystals structurally related to apatite (Leroy & Bres, 2001).

Because of its good biocompatibility, bioactivity and osteoconductivity with human body constituents, hydroxyapatite ($Ca_{10}(PO_4)_6(OH)_2$, HA) is widely used in the biomedical fields (Zhang & Darvell, 2010; Fathi & Hanifi, 2007). Despite these optimal properties, poor thermostability and poor mechanical properties of synthetic HA have limited its clinical applications (Kim *et al.*, 2009). Biological apatites contain various amounts of substitutions (i.e. F^-, CO_3^{2-}, Na^+, Mg^{2+}, Zn^{2+}) (Bianco *et al.*, 2009; Suchanek *et al.*, 2004). Recently, attention has been given to the modification of properties of apatites, such as bioactivity, biocompatibility and solubility with ionic substitutions. Fluorine-substituted HA ($Ca_{10}(PO_4)_6(OH)_xF_{2-x}$, HFA) and fluorapatite ($Ca_{10}(PO_4)_6F_2$, FA) have low solubility, good biocompatibility, high thermal and chemical stability (Bianco *et al.*, 2010; Bogdanov *et al.*, 2009). This makes it good alternative potential candidates to be used in dental implants and bone repair. Fluorine replacement can favor the crystallization of calcium phosphate, improve thermal stability and decrease the mineral dissolution (Kim *et al.*, 2009; Cheng *et al.*, 2003; Miao *et al.*, 2005).

The main components of the apatite family are hydroxyapatite (OHAp, $Ca_{10}(PO_4)_6(OH)_2$), chlorapatite (ClAp, $Ca_{10}(PO_4)_6Cl_2$), carbonated apatites and fluorapatite (FAp, $Ca_{10}(PO_4)_6F_2$). For the latter component, several applications in different areas are known. The existence of several natural minerals containing this component e.g., Durango, Mexico; Quebec, Canada; New Mexico or Connecticut, USA; Epirus, Greece (Bale, 1940; Hendricks *et al.*, 1932; Sudarsanan *et al.*, 1972) has led to their use in many applications. There are several methods for synthesis, which allows control of stoichiometry and/or morphology of the synthesized calcium phosphate (Elliott, 1998). In addition, FAp has been used in phosphorus chemistry, as a catalyser or a H_3PO_4 source (this represents 75% of natural apatite use), but also in the area of solid-state laser hosts (rare-earth doped FAp). In geology it was used as a probe of phosphorus activity in hydrothermal, metamorphic or magmatic processes.

FA is also the main calcium phosphate used in phosphated fertilisers. Apatites are also important in biology because they form the mineral part of bone and teeth and take part in the mineralization process. FAs are used as biocompatible materials for bone replacement and coating of bone prostheses. One of the components of FA is fluoride, which is often used therapeutically in order to prevent caries. In nature, fluoride can be found in soils, in minerals such as fluorine, hornblende, pegmatite and FA. Due to erosion, fluoride salts are also present in the atmosphere. The atmospheric concentration of fluoride salts depends on the presence of fluoride in the environment. Therefore, it is a function of the presence of fluoride in soils or in industrial waste. Fluoride is also present in water, especially in the oceans, or near mountainous or sedimentary areas. Water is also used as a medium of caries prevention, and so represents the main source of fluoride. Natural fluoride is fund in some foods, especially in plants, at different concentrations, independent of the soil concentration (Plouvier, 1997). All fluoride ingested is first taken up by the circulation and then in hard tissues (such as bone or dentin). The fixation of fluoride by bone and tooth depends on the supply of fluoride and the age of the subject. Bone is responsible for the homeostasis of fluoride in the organism. Fluoride is excreted by the kidneys, via a passive diffusion mechanism.

Magnesium (Mg^{2+}) is one of the most important cationic substitutions for calcium in biological apatites. Dentin, enamel and bone contain 1.23, 0.44, and 0.72 % of Mg^{2+}, respectively. Mg-substituted HA ceramics have been suggested for use in orthopædic and dental applications (Suchanek *et al.*, 2004). The formation and attachment of biomimetic Ca-P coatings in simulated body fluid (SBF) solution were strongly related to Mg^{2+} content and Mg-substitution improves the bioactivity of apatite in SBF (Barrere *et al.*, 2002; Kheradmandfard *et al.*, 2012). Keeping the above points in view, Mg^{2+} substituted FA bioceramics are expected to have better biocompatibility and biological properties than pure FA (Kheradmandfard *et al.*, 2012; Cai *et al.*, 2009).

This excretion represents 40 to 60% of the fluoride ingested. Fluoride plays an important role in caries prevention: it increases the resistance of the mineral to acid dissolution and decreases mineral solubility (Aoba, 1997). By substituting the OH^- ion in the apatite molecule during the development phase of dentin and enamel, fluoride fixes calcium, provides increased stability to the mineral structure, and promotes remineralization (Aoba, 1997).

Mechanical alloying (MA) is an effective way of preparing nanocrystalline or nanostructured materials, such as ceramics, composites and intermetallic compounds. MA method offers a simple, powerful and economical tool for fabrication of several advanced materials (Ali & Basu, 2010; Yang *et al.*, 2008; Shi *et al.*, 2008).

2.13.2 Simulated Body Fluids (SBF)

Simulated body fluid (SBF) is a solution with an ionic concentration close to that of human blood plasma, kept under mild conditions of pH and identical physiological temperature (Kokubo, 1991). SBF was first introduced by Kokubo et al. in order to evaluate the changes on a surface of a bioactive glass ceramic (Kokubo *et al.*, 1990). Later, cell culture media (such as DMEM, MEM, α-MEM[8], etc.), in combination with some methodologies adopted in cell culture, were suggested as an alternative to conventional SBF in assessing the bioactivity of materials (Lee *et al.*, 2011).

The historical development of synthetic or simulated body fluids (SBF, which claim to mimic a cellular human blood plasma) cannot be pictured accurately without mentioning the Ringer's solution of 1880 (Ringer & Physiol, 1882) and Hanks' balanced salt solution (HBSS) of 1949 (Hanks & Wallace 1949). SBF solutions developed by T. Kokubo between

---

[8] Dulbecco's Modified Eagle's Medium, Modified Eagle's Medium, Minimum Essential Medium

1990 and 2006 may be considered as being closely associated with EBSS and HBSS (Kokubo & Non-Cryst, 1990; Kokubo & Takadama, 2006).

The ionic concentrations of a cellular human blood plasma and some physiological solutions are compared in Table 2.8. HBSS and EBSS (Earl's Balanced Salt Solution) solutions, on the other hand, are commercially available today as either supplemented with glucose or with amino acids and vitamins, and are commonly used in tissue engineering or cell culture studies. Solutions such as HBSS and EBSS do help to maintain intra- and extracellular osmotic balance, provide cells with water and certain bulk inorganic ions essential for normal cell metabolism, and provide a buffering system to maintain the medium within the physiological pH range (7.2–7.6). The HCO_3^- concentration of the EBSS solution (i.e., 26.2 mM[9]) resembles that of human plasma (27 mM). On the other hand, the carbonate ion concentration of the HBSS solution is much lower than that (i.e., 4.2 mM). The SBF (simulated body fluid) solution resemble a Tris-HCl[10] buffered (at pH 7.4 and 37°C) HBSS solution whose Ca/P molar ratio was adjusted to 2.50, and whose Mg^{2+} concentration was increased from 0.81 (HBSS) to 1.5 mM (Kokubo & Non-Cryst, 1990). The original HBSS solution had a Ca/P molar ratio of 1.62, whereas the same ratio in EBSS was 1.80 (Devreker *et al.*, 2001; Karamalegos & Bolton, 1999).

Table 2.8: Ion concentrations of human plasma and synthetic solutions. The concentration is in millimolar (mM).

	Human Plasma	Ringer	EBSS	HBSS	Kokubo–SBF	Tas–SBF
Na^+	142	130	143.6	138	142	142
K^+	5	4	5.37	6.14	5	5
Ca^{2+}	2.5	1.4	1.8	1.26	2.5	2.5
Mg^{2+}	1.5	-	0.81	0.81	1.5	1.5
Cl^-	103	109	125.3	144.8	147.8	125
HCO_3^-	27	-	26.2	4.2	4.2	27
HPO_4^{2-}	1	-	1	0.78	1	1
SO_4^{2-}	0.5	-	0.81	0.81	0.5	0.5
Ca/P	2.5	-	1.8	1.62	2.5	2.5
Buffer	-	-	-	-	Tris	Tris
pH	7.4	6.5	7.2-7.6	6.7-6.9	7.4	7.4

---

[9] Millimolar concentration (mM).

[10] Tris(hydroxymethyl)aminomethane hydrochloride,

Chapter 3

Materials and Methods

3.1 Introduction

This chapter describes the experimental procedure and materials used in the study. This includes the choice and preparation of the materials. Various characterization techniques including PLD, XRD, EDS and AFM, were used to study the optical properties of the material.

3.2 Experimental design

3.2.1 The study involved the use of Co-Cr-Mo dental alloys

The dental alloys were purchased from American Elements, Los Angeles, USA, and were provided as a small disk (ASTM F75). All experimental procedures were performed at Cape Peninsula University of Technology (CPUT), iThemba LABS, Stellenbosch University and University of Western Cape (UWC). The chemical composition of Co-Cr-Mo alloy is shown in Table 3.1.

Table 3.1: Chemical composition (%) of Co-Cr-Mo alloys.

Element	%
Co	64
Cr	28
Mo	5
C	Max 0.35
Mn	Max 0.35
Si	Max 0.35

The alloy was acquired in cylindrical form with diameter of 2 cm and a height of 2 cm. The alloys were then cut using Colchester 5x20 Chipmaster Machine (Lathe, Colchester, UK) housed at the Material Research Department (MRD), iThemba LABS, Faure, South Africa, into 0.1cm height and the same diameter. The tablet was then cut into equal parts to form 1cm in diameter (Figure 3.1).

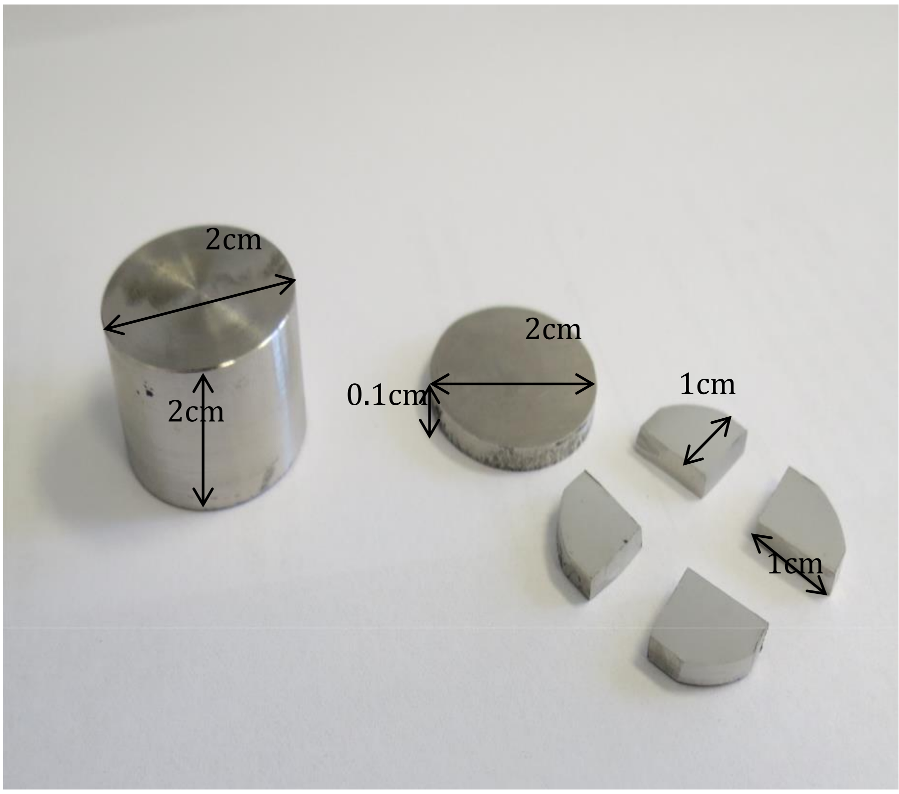

Figure 3.1: Illustration of the alloy before and after cutting the pieces.

3.2.2 Preparation of the nanopowder

The preparation of fluorapatite powder was performed according to Fathi *et al.*, (2009). The powder was prepared by mixing stoichiometric amounts of calcium hydroxide ($Ca(OH)_2$), phosphorous pentoxide (P_2O_5) and calcium fluoride (CaF_2). The mixing was performed in a planetary high-energy ball mill using a zirconium vial and zirconium balls (housed at Department of Chemical Engineering, Cape Peninsula University of Technology, Bellville, South Africa) with ball-to powder mass ratio of 35:1. The rotational speed was 300 rpm, and the mixing was done for a period of six hours. The fluorapatite nanopowder particles obtained had a size of approximately 35-65 nm (Figure 3.2 and 3.3).

Figure 3.2: Zirconium vial and zirconium balls used for fluorapatite preparation.

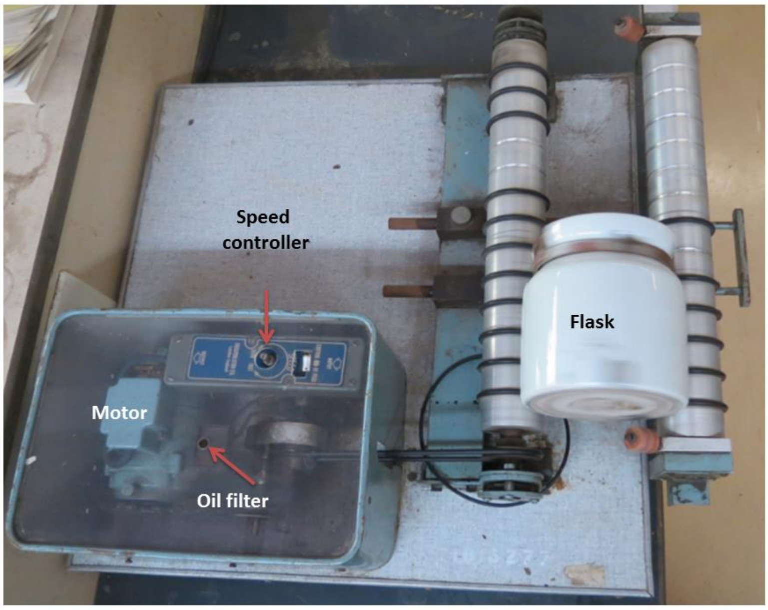

Figure 3.3: Porcelain laboratory scales Ball-Mill dimension.

3.2.3 Preparation of fluorapatite pellets

The pellet, with a diameter of 20 mm and a height of 3 mm, was prepared under the pressure of 12 tons for a period of 30 minutes using lab pellet presses, obtained from MRD iThemba LABS, (Figure 3.4).

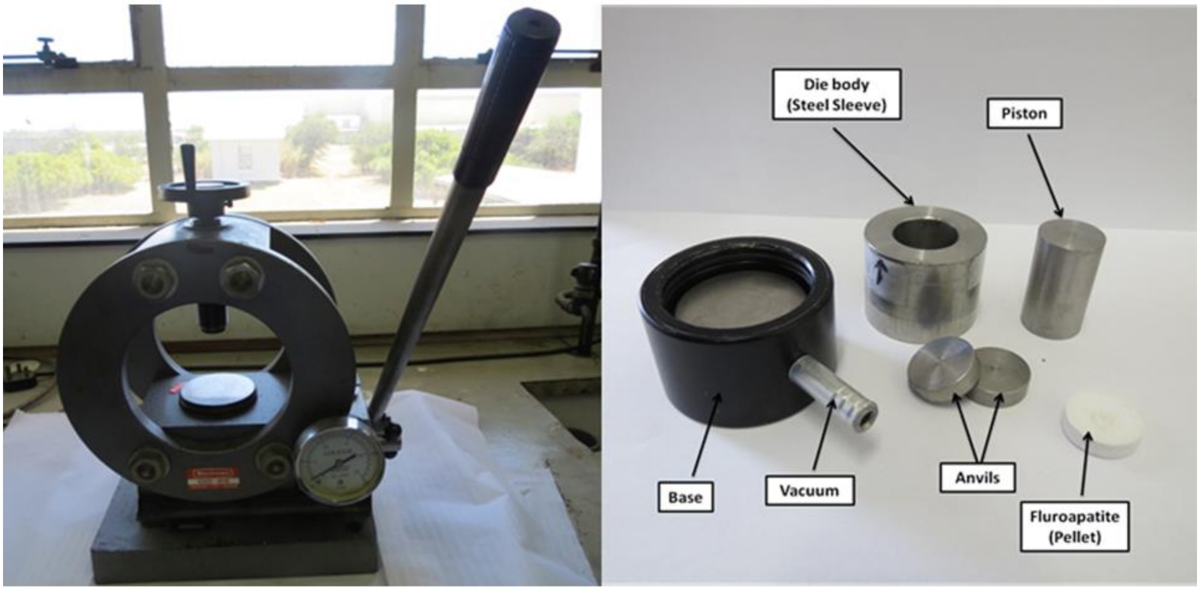

Figure 3.4: Lab Pellet Press (to the left) Beckman 00-25, Glenrothes Fife, Scotland, and its components (to the right).

3.3 Pulsed Laser Deposition (PLD)

The main goal of sample preparation process was to create uniform and homogeneous thin films on substrates.

3.3.1 Preparation of FA nanopowder on glass substrate

The glass substrates were chosen to optimize the procedure to be followed in the deposition of FA powder on Co-Cr-Mo, since the glass is less costly. Different energy, pressure and time were used in the optimization of the deposition protocol. The protocol described in Table 3.1 was set as a standard protocol. The glass substrate was cut in the form of square length of 1 cm, cleaned with distilled water and acetone for use in the analysis of PLD. The working distance between the target (FA powder) and glass substrate during laser deposition was kept at 3.8 cm.

In this case, the preparation of FA powder on glass substrate for each deposition were done at room temperature, laser energy of 130 mJ and pressure 7×10^{-9} MPa for a duration of 10 minutes. This laser power, pressure and time were chosen since it gave best results expected.

3.3.2 Preparation of FA powder on Co-Cr-Mo alloys using PLD

The alloys were each cut into four quarter section and were cleaned with acetone and distilled water prior to the deposition. The target-to-substrate distance was maintained at 3.8 cm. All of the depositions were performed at room temperature according to the procedure described in Table 3.2.

Table 3.2: Illustration of the difference laser energy, pressure and time used during deposition of each sample.

Sample	Laser energy (mJ)	Pressure	Deposition time
a	130	7×10^{-9}MPa	5 min
b	130	7×10^{-9}MPa	10 min
c	130	7×10^{-9}MPa	20 min
d	170	7×10^{-9}MPa	10 min
e	170	7×10^{-9}MPa	15 min

3.3.3 Deposition of Co-Cr-Mo alloy as a target on silicon substrate

The Co-Cr-Mo was also used as a target to verify if deposition can be performed by PLD for future use. The samples were prepared as described in section 3.2.1. The same procedure was followed as in Table 3.1. with a different laser power of 180 mJ, pressure 7×10^{-9} MPa and time 20 minutes. The PLD system is shown in Figure 3.5.

Figure 3.5: Pulsed Laser Deposition (PLD) system located in the Physics Department at the Stellenbosch University, Stellenbosch, South Africa.

3.4 Preparation of simulated body fluid (SBF)

The SBF was prepared with the ionic concentration nearly similar to the human blood plasma. The body fluid was prepared according to a procedure developed by Kokubo (Kokubo, 1990). The solution was prepared in the Department of Biomedical Sciences at CPUT.

Analytical reagent grade NaCl, $NaHCO_3$, KCl, $K_2HPO_4 \cdot 3H_2O$, $MgCl_2 \cdot 6H_2O$, $CaCl_2$, Na_2SO_4 were used in the preparation of SBF. The chemical reagents were dissolved in 1 L of double distilled water so as to have an ionic concentration of various inorganic ions similar to those of the human blood plasma. The ionic concentration of SBF as prepared by Kokubo and its comparison with human blood plasma are shown in Table 2.9. The SBF was prepared according to Table 3.3, which shows appropriate amounts of reagents added in double distilled water so as to have ionic concentration as mentioned (Ohtsuki, 1995; Prado da Silva *et al.*, 2001). Reagents were added, one after another, to ensure complete dissolution. HCl was added to maintain the pH of the solution at 7.4. The temperature of the solution was maintained at 37^{0}C.

Table 3.3: Reagents used for preparing SBF (1 L, pH 7.4), (Ohtsuki, 1995).

Order	Reagent	Amount (g/l)
1	NaCl	7.996 ± 0.005 g
2	$NaHCO_3$	0.350 ± 0.005 g
3	KCl	0.224 ± 0.005 g
4	$K_2HPO_4 \cdot 3H_2O$	0.228 ± 0.005 g
5	$MgCl_2 \cdot 6H_2O$	0.305 ± 0.005 g
6	1 M-HCl	40.00 ± 0.05ml
7	$CaCl_2$	0.278 ± 0.005 g
8	Na_2SO_4	0.071 ± 0.005 g
9	$(CH_2OH)_3CNH_2$	6.057 ± 0.005 g

3.5 Analytical techniques

3.5.1 X-ray diffraction analysis (XRD)

X-ray diffraction was used to characterize the crystalline structure and phases of material used in the study. In addition, it provides information with regards to the chemical compounds of material. A Bruker D8 Advance XRD tool with Cu K_{α} source wavelength of 1.54 Å housed at the Materials Research Department (MRD), iThemba LABS, Faure, South Africa, was used (Figure 3.6). The instrument has a Vantec detector of 2000 for detecting deviation angles and wide range of materials. It characterizes the crystal structure, and solid phases Materials, and other structural parameters, such as the average grain size, crystallization and X-rays defects strain, crystal diffraction peaks.

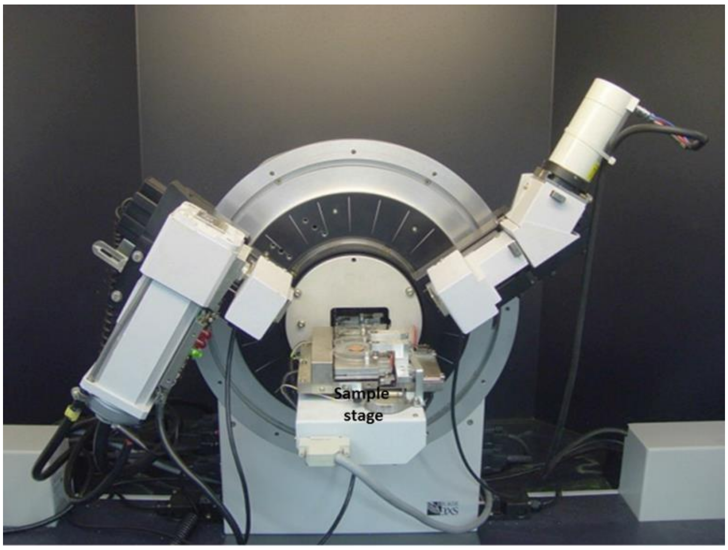

Figure 3.6: The Bruker D8 Advance XRD instrument in Department of Materials Research (MRD), iThemba LABS, Faure, South Africa.

3.5.2 Scanning electron microscopy (SEM)

The SEM (Auriga Carl Zeiss, Germany) was used to determine the surface morphology of the dental material. The instrument is housed at Physics Department at University of the Western Cape, Bellville, South Africa (Figure 3.7).

3.5.3 Energy Dispersive X-ray Spectroscopy (EDS)

Energy Dispersive X-ray Spectroscopy (EDS) was used to determine the chemical composition of the dental material. Elemental mapping and atomic composition of the alloys were performed using Energy Dispersive X-ray Spectroscopy (EDS), which is interfaced with

SEM. Atomic qualitative and quantities information from the specimen can be supplied by an EDS system.

It relies on the investigation of a sample through interactions between electromagnetic radiation and matter, analyzing x-rays emitted by the matter in response to being hit with charged particles. Its characterization capabilities are due in large part to the fundamental principle that each element has a unique atomic structure allowing X-rays that are characteristic of an element's atomic structure to be identified uniquely from each other.

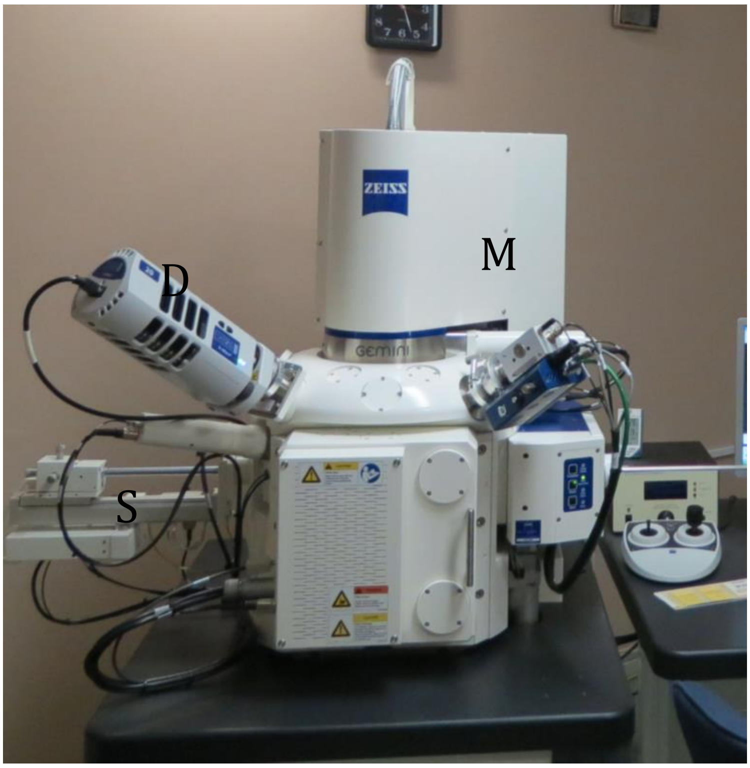

Figure 3.7: Scanning Electron Microscopy (SEM) that was used to determine the surface morphology and the Energy Dispersive analysis of X-rays is located in the Department of physics science at the University of the Western Cape, Bellville, South Africa.

3.5.4 Atomic force microscopy (AFM)

The AFM (Nanosurf Easyscan2 compact) was used to trace the surface topography of the dental material. The AFM provides three-dimensional surface images of the sample with high resolution, by measuring forces between a sharp probe (¡10 nm) and surface at very short distance (0.2-10 nm).

AFM is a high-resolution surface imaging technique which works by scanning a sharp probe over the surface of a specimen, while measuring the forces experienced by the probe.

In the most commonly used imaging mode, the probe and sample are brought in contact and the probe is scanned over the surface while the interaction force is kept constant.

The manufacturer's Gwydion computational software, version 2.36, was used to convert the data into high-resolution 3-D surface images of the alloys. The AFM analyses were performed in the Department of Electrical and Electronic Engineering at the Stellenbosch University, Stellenbosch, South Africa, and is shown in figure 3.8.

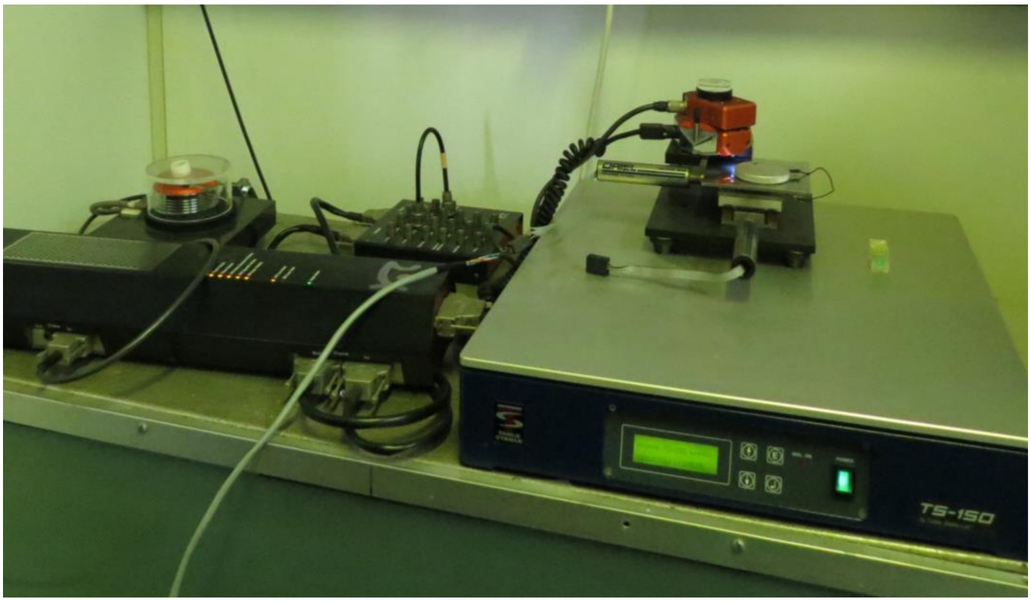

Figure 3.8. The Nanosurf Easyscan2 compact AFM measurement in the Geology Department, at the Stellenbosch University, Stellenbosch, South Africa.

Chapter 4

Results and Discussions

4.1 Introduction

In this chapter the data, resulting from the application of the analytical techniques are presented as images and plots of spectra.

4.2 X-ray diffraction (XRD) spectra and data sheets based on the Joint Committee of Powder Diffraction Standards (JCPDS) used in the study

The XRD spectra and JCPDS data sheet are shown in the following figures. The first two figures display the spectrum and data sheet for calcium hydroxide, $Ca(OH)_2$, figures 4.1 and 4.2, the succeeding figures for calcium fluoride (CaF_2), figures 4.3 and 4.4, then for phosphorus pentoxide, $(P_2O_5)_2$, figures 4.5 and 4.6, and afterwards, fluorapatite, $Ca_5(PO_4)_3F$, figures 4.7 and 4.8.

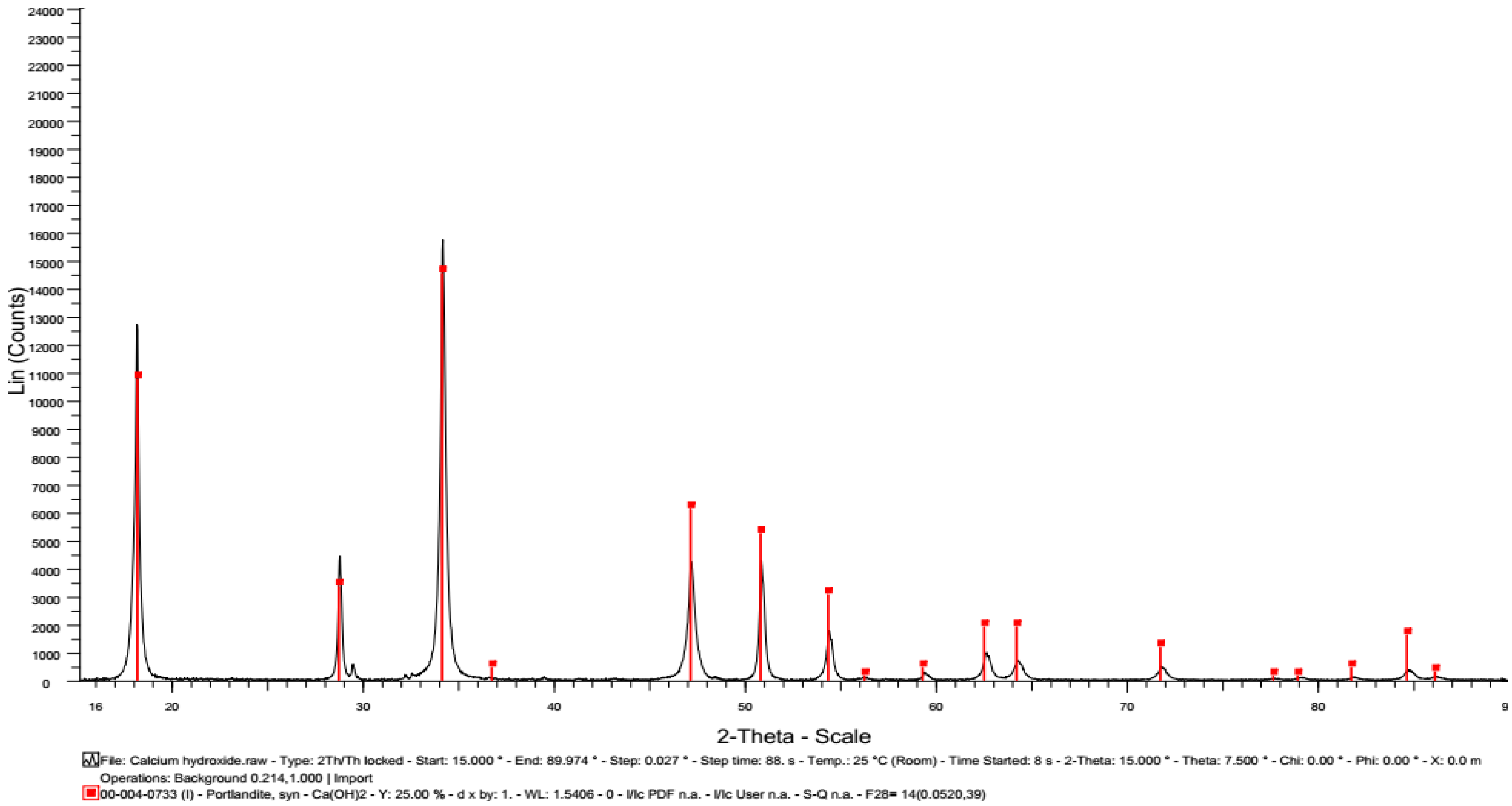

Figure 4.1 X-ray diffraction spectrum of calcium hydroxide, $Ca(OH)_2$.

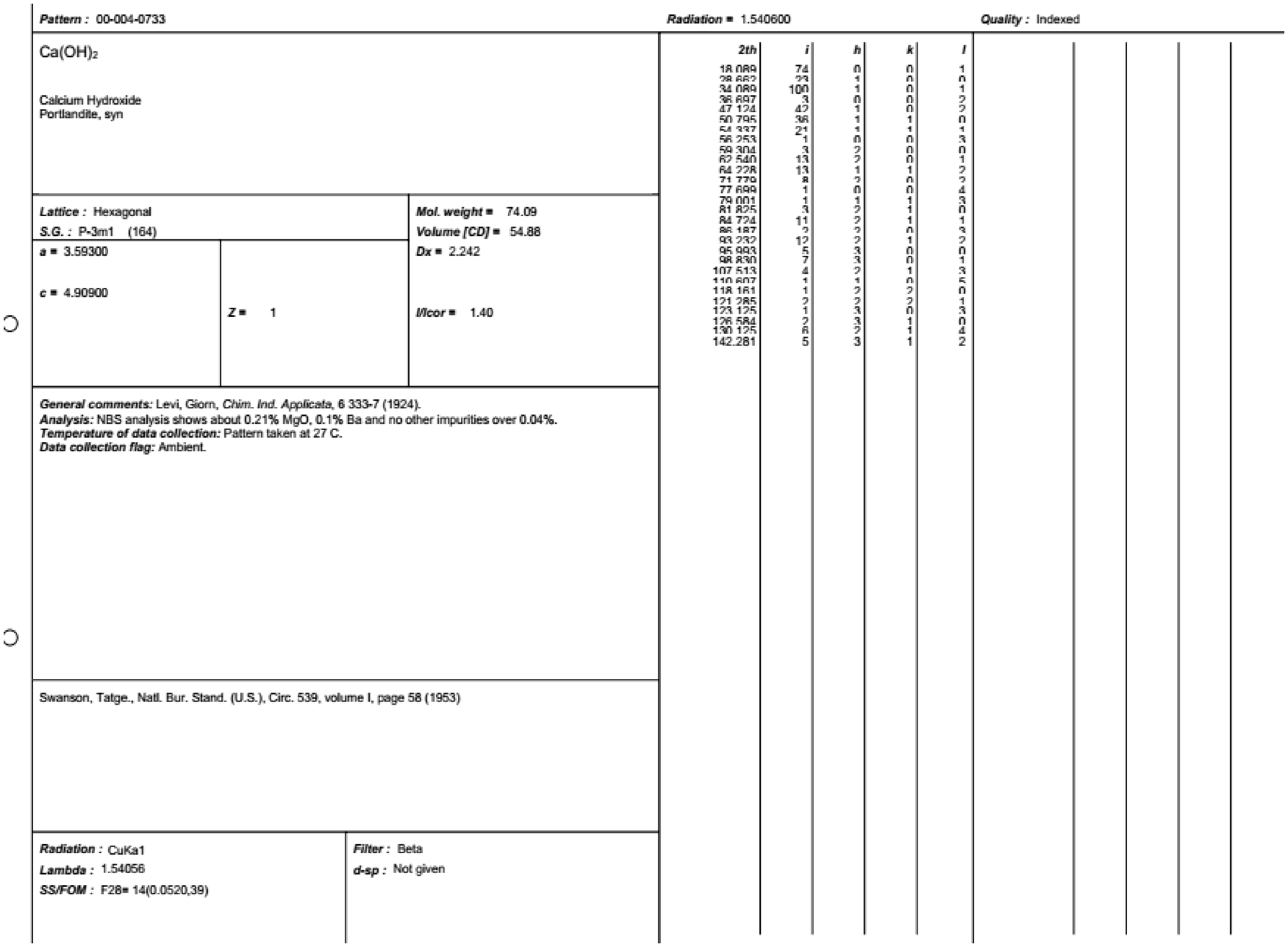

Pattern : 00-004-0733

Radiation = 1.540600

Quality : Indexed

$Ca(OH)_2$

Calcium Hydroxide
Portlandite, syn

Lattice : Hexagonal
S.G. : P-3m1 (164)
a = 3.59300
c = 4.90900
Z = 1
Mol. weight = 74.09
Volume [CD] = 54.88
Dx = 2.242
I/Icor = 1.40

General comments: Levi, Giorn, *Chim. Ind. Applicata*, 6 333-7 (1924).
Analysis: NBS analysis shows about 0.21% MgO, 0.1% Ba and no other impurities over 0.04%.
Temperature of data collection: Pattern taken at 27 C.
Data collection flag: Ambient.

Swanson, Tatge., Natl. Bur. Stand. (U.S.), Circ. 539, volume I, page 58 (1953)

Radiation : CuKa1
Lambda : 1.54056
SS/FOM : F28= 14(0.0520,39)
Filter : Beta
d-sp : Not given

2th	*i*	*h*	*k*	*l*
18.089	74	0	0	1
28.662	23	1	0	0
34.089	100	1	0	1
36.697	3	0	0	2
47.124	42	1	0	2
50.795	36	1	1	0
54.337	21	1	1	1
56.253	1	0	0	3
59.304	3	2	0	0
62.540	13	2	0	1
64.228	13	1	1	2
71.779	8	2	0	2
77.699	1	0	0	4
79.001	1	1	1	3
81.825	3	2	1	0
84.724	11	2	1	1
86.187	2	2	0	3
93.232	12	2	1	2
95.993	5	3	0	0
98.830	7	3	0	1
107.513	4	2	1	3
110.607	1	1	0	5
118.161	1	2	2	0
121.285	2	2	2	1
123.125	1	3	0	3
126.584	2	3	1	0
130.125	6	2	1	4
142.281	5	3	1	2

Figure 4.2 JCDPS sheet of calcium hydroxide, $Ca(OH)_2$.

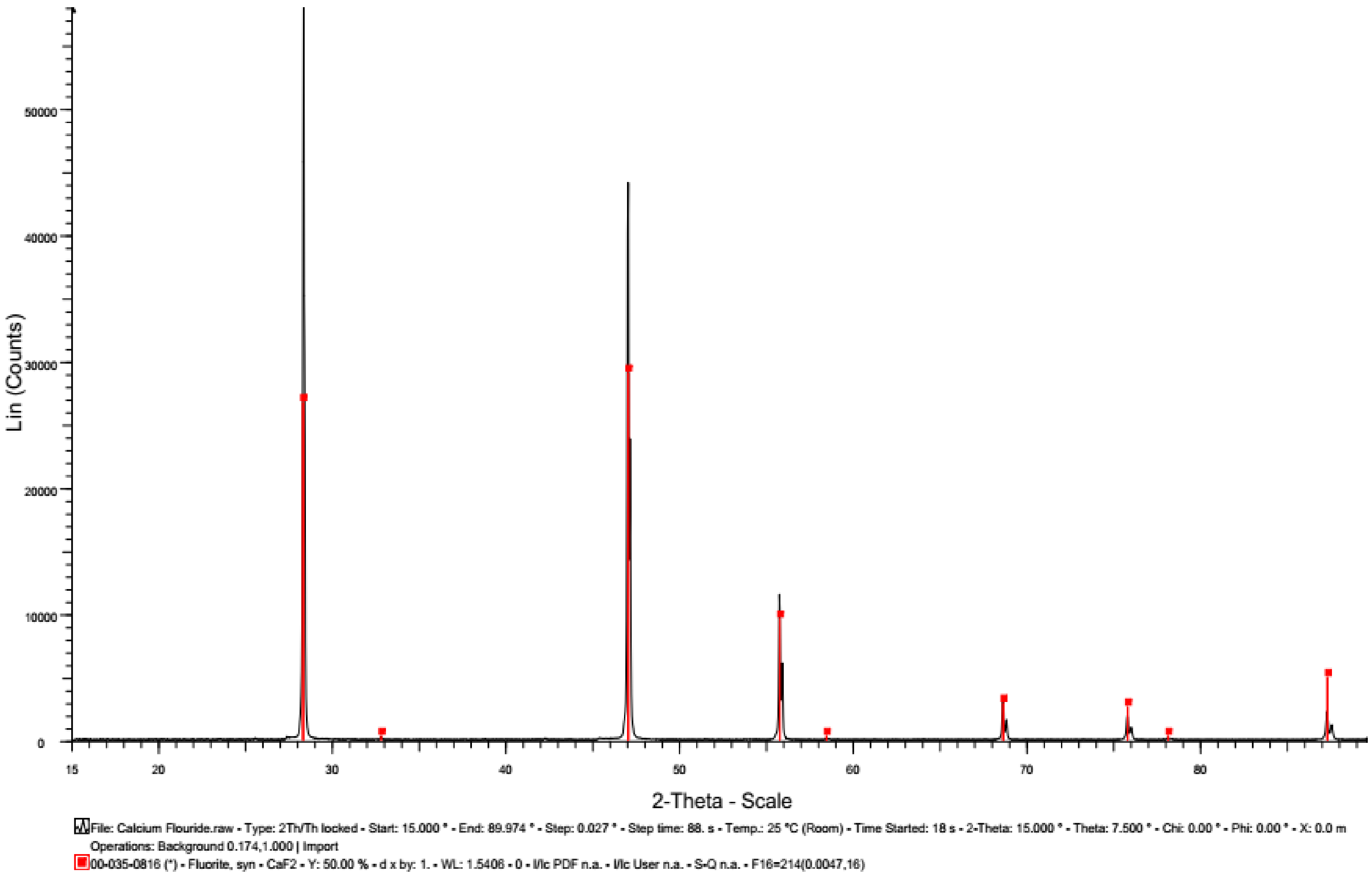

Figure 4.3 X-ray diffraction spectrum of calcium fluoride, CaF_2.

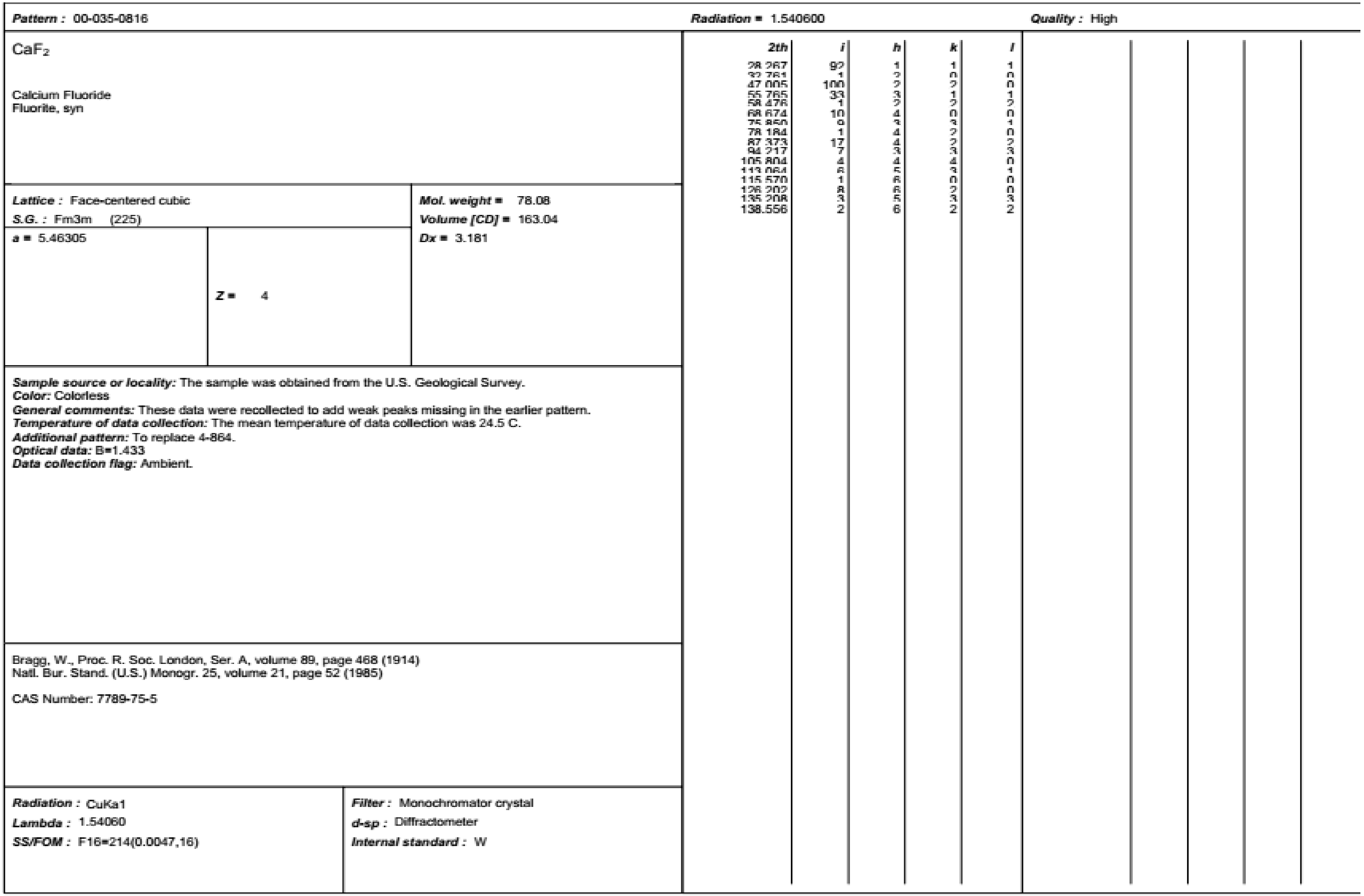

Pattern : 00-035-0816

Radiation = 1.540600

Quality : High

CaF_2

Calcium Fluoride
Fluorite, syn

Lattice : Face-centered cubic
S.G. : Fm3m (225)
a = 5.46305
Z = 4

Mol. weight = 78.08
Volume [CD] = 163.04
Dx = 3.181

Sample source or locality: The sample was obtained from the U.S. Geological Survey.
Color: Colorless
General comments: These data were recollected to add weak peaks missing in the earlier pattern.
Temperature of data collection: The mean temperature of data collection was 24.5 C.
Additional pattern: To replace 4-864.
Optical data: B=1.433
Data collection flag: Ambient.

Bragg, W., Proc. R. Soc. London, Ser. A, volume 89, page 468 (1914)
Natl. Bur. Stand. (U.S.) Monogr. 25, volume 21, page 52 (1985)

CAS Number: 7789-75-5

Radiation : CuKa1
Lambda : 1.54060
SS/FOM : F16=214(0.0047,16)

Filter : Monochromator crystal
d-sp : Diffractometer
Internal standard : W

2th	*i*	*h*	*k*	*l*
28.267	92	1	1	1
32.761	1	2	0	0
47.005	100	2	2	0
55.765	33	3	1	1
58.476	1	2	2	2
68.674	10	4	0	0
75.850	9	3	3	1
78.184	1	4	2	0
87.373	17	4	2	2
94.217	7	3	3	3
105.804	4	4	4	0
113.064	6	5	3	1
115.570	1	6	0	0
126.202	8	6	2	0
135.208	3	5	3	3
138.556	2	6	2	2

Figure 4.4 JCDPS sheet of calcium fluoride, CaF_2.

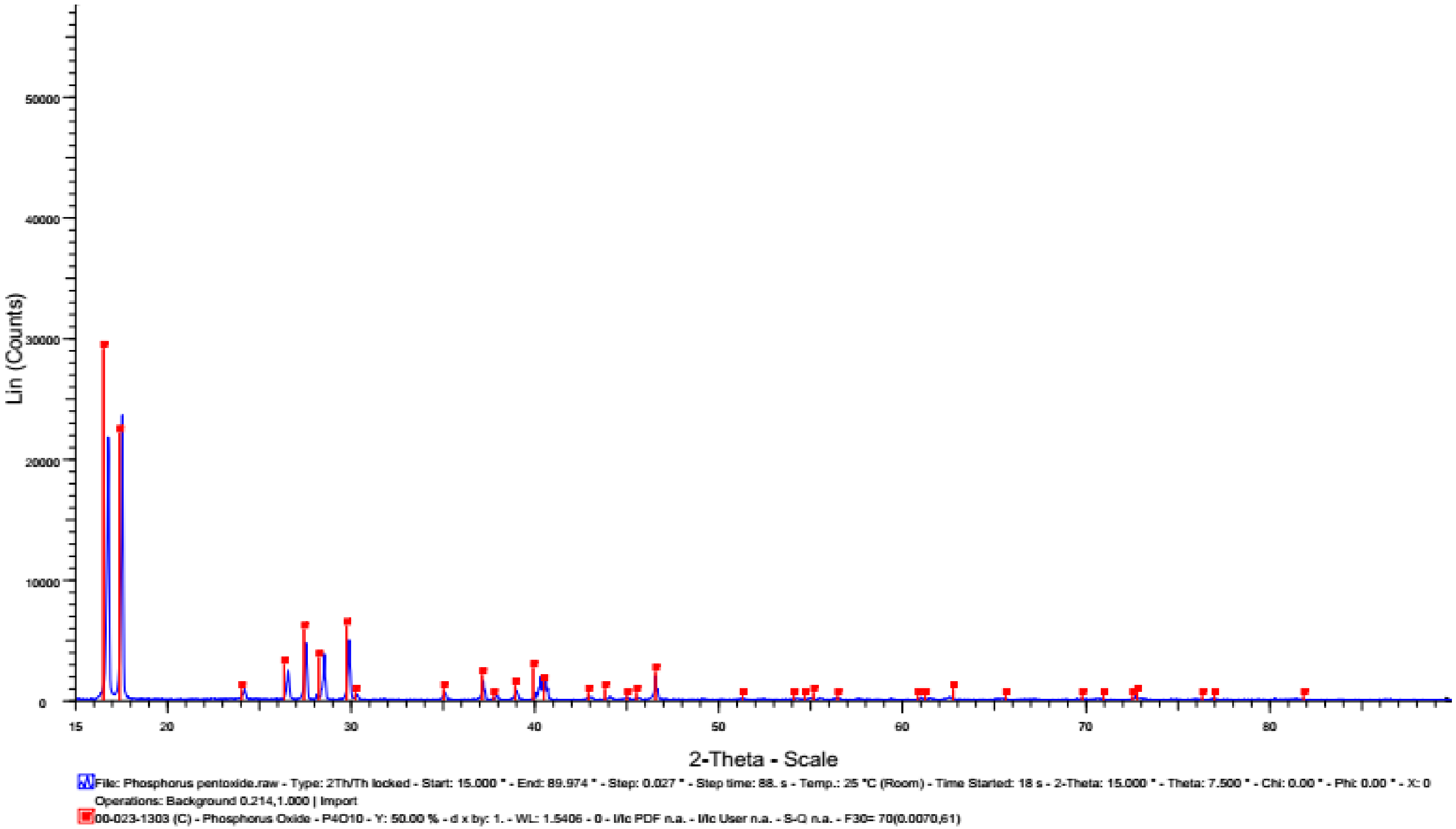

Figure 4.5 X-ray diffraction spectrum of phosphorus pentoxide, $(P_2O_5)_2$.

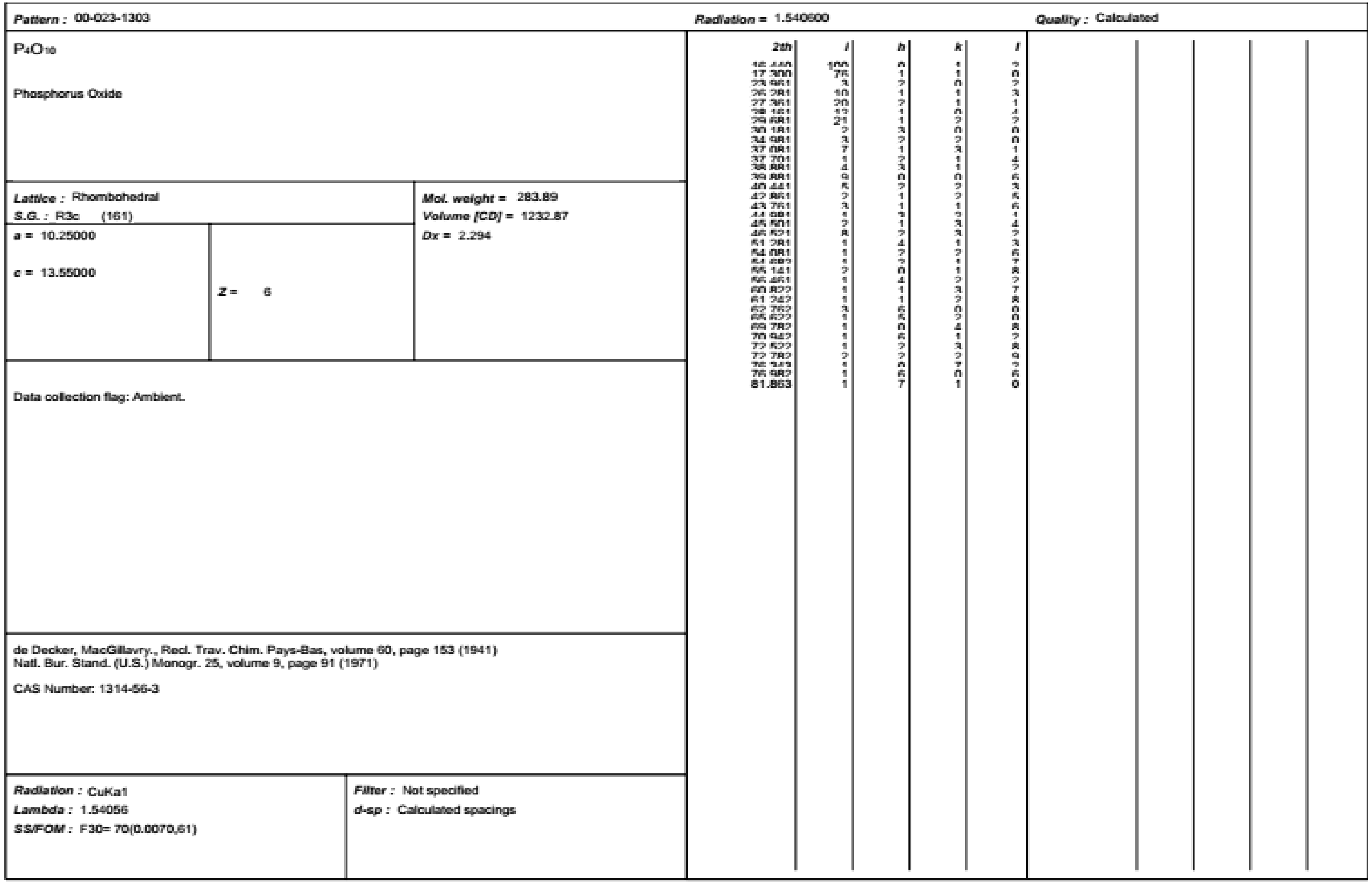

Pattern : 00-023-1303

Radiation = 1.540600

Quality : Calculated

P_4O_{10}

Phosphorus Oxide

Lattice : Rhombohedral

S.G. : R3c (161)

a = 10.25000

c = 13.55000

Z = 6

Mol. weight = 283.89

Volume [CD] = 1232.87

Dx = 2.294

Data collection flag: Ambient.

de Decker, MacGillavry., Recl. Trav. Chim. Pays-Bas, volume 60, page 153 (1941)
Natl. Bur. Stand. (U.S.) Monogr. 25, volume 9, page 91 (1971)

CAS Number: 1314-56-3

Radiation : CuKa1

Lambda : 1.54056

SS/FOM : F30= 70(0.0070,61)

Filter : Not specified

d-sp : Calculated spacings

2th	*i*	*h*	*k*	*l*
16.440	100	0	1	2
17.300	76	1	1	0
23.981	3	2	0	2
26.281	10	1	1	3
27.361	20	2	1	1
28.161	12	1	0	4
29.681	21	1	2	2
30.181	2	3	0	0
34.981	3	2	2	0
37.081	7	1	3	1
37.701	1	2	1	4
38.881	4	3	1	2
39.881	9	0	0	6
40.441	5	2	2	3
42.861	2	1	2	5
43.761	3	1	1	6
44.981	1	3	2	1
45.501	2	1	3	4
46.521	8	2	3	2
51.281	1	4	1	3
54.081	1	2	2	6
54.682	1	2	1	7
55.141	2	0	1	8
56.461	1	4	2	2
60.822	1	1	3	7
61.242	1	1	2	8
62.762	3	6	0	0
65.622	1	5	2	0
69.782	1	0	4	8
70.942	1	6	1	2
72.522	1	2	3	8
72.782	2	2	2	9
75.343	1	0	7	2
76.982	1	6	0	6
81.863	1	7	1	0

Figure 4.6 JCDPS sheet of phosphorus pentoxide, $(P_2O_5)_2$.

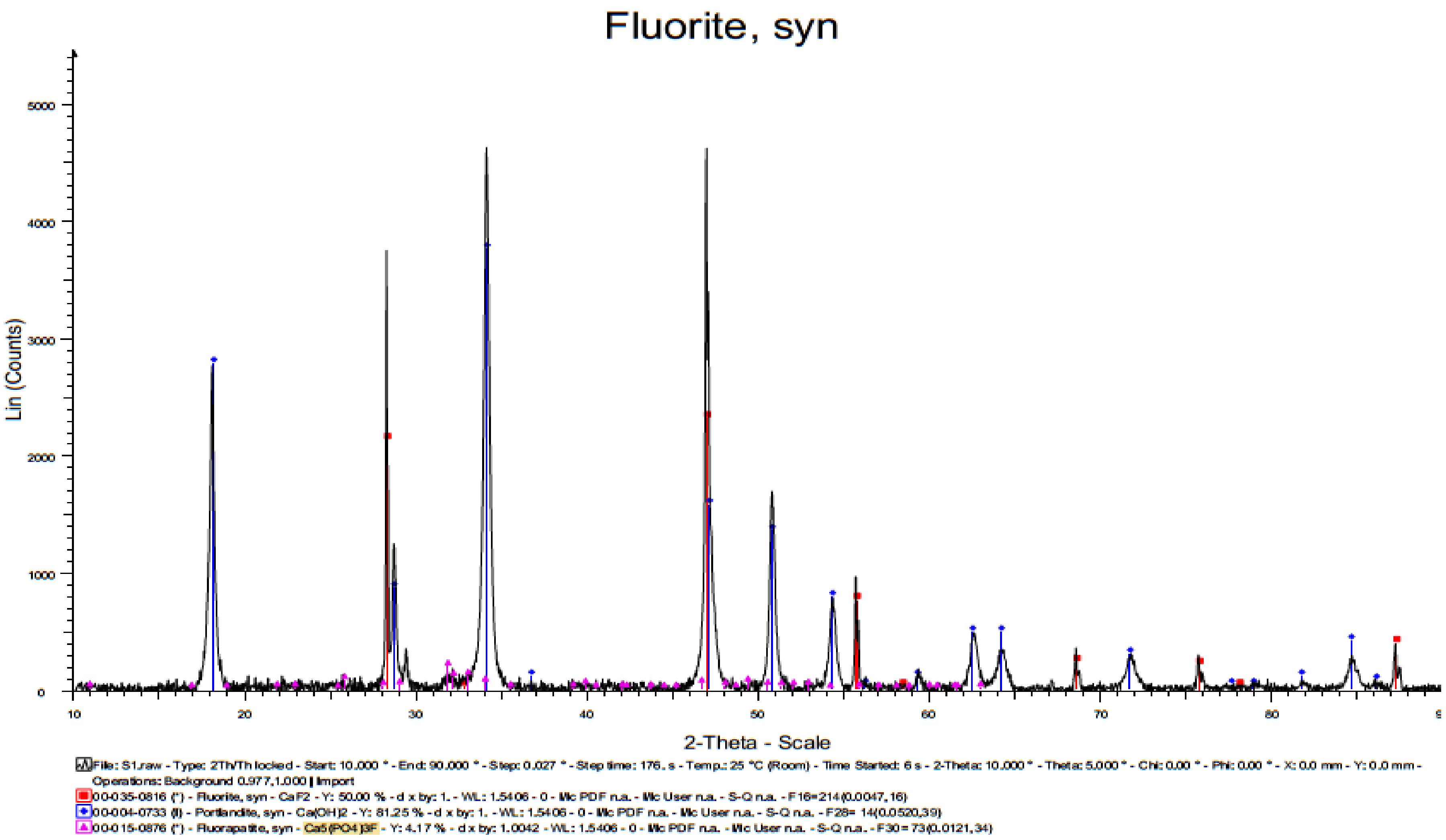

Figure 4.7 X-ray diffraction spectrum of fluorapatite.

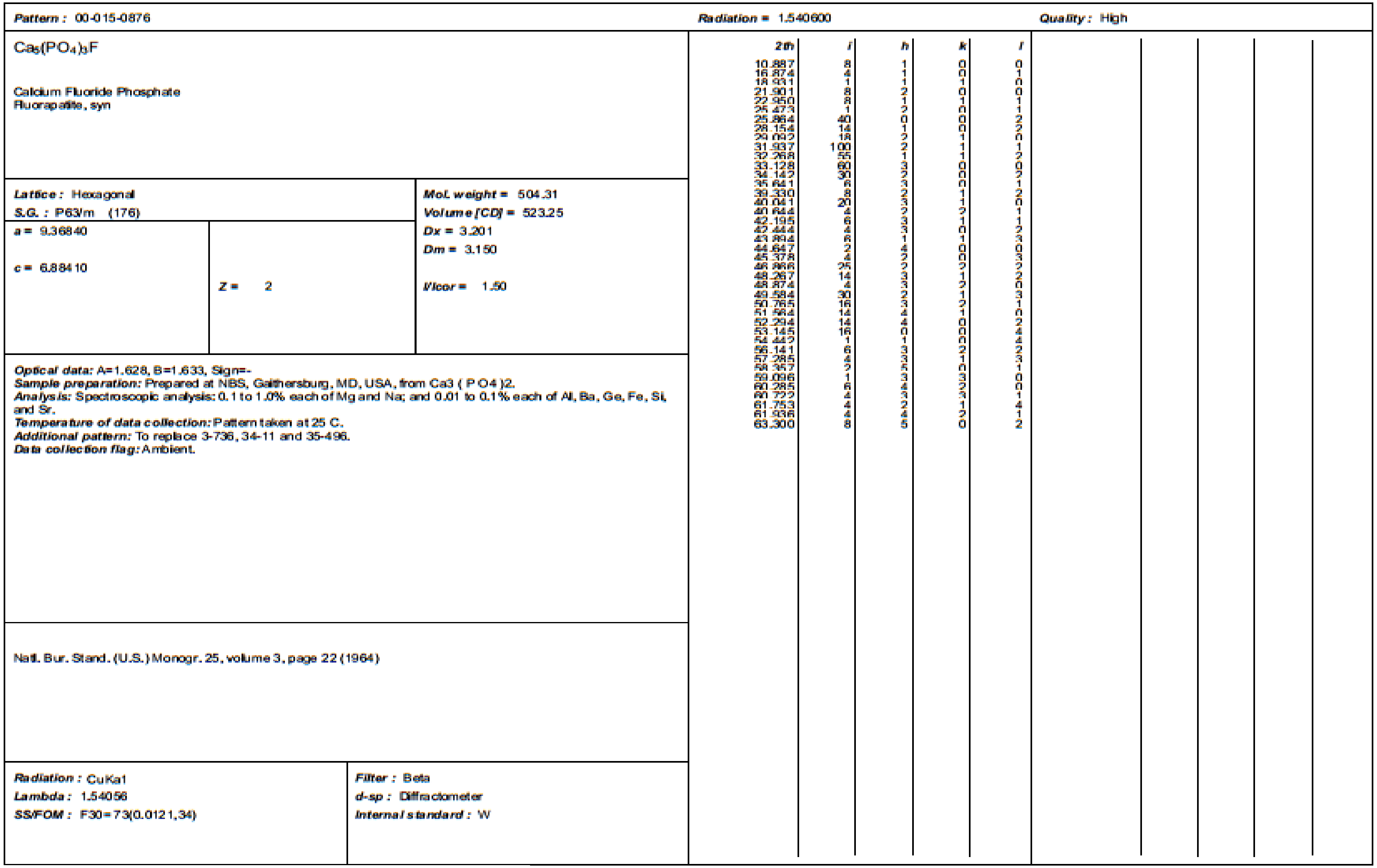

Pattern : 00-015-0876

Radiation = 1.540600

Quality : High

$Ca_5(PO_4)_3F$

Calcium Fluoride Phosphate
Fluorapatite, syn

Lattice : Hexagonal
S.G. : P63/m (176)
a = 9.36840
c = 6.88410
Z = 2

Mol. weight = 504.31
Volume [CD] = 523.25
Dx = 3.201
Dm = 3.150
I/Icor = 1.50

Optical data: A=1.628, B=1.633, Sign=-
Sample preparation: Prepared at NBS, Gaithersburg, MD, USA, from Ca3 (P O4)2.
Analysis: Spectroscopic analysis: 0.1 to 1.0% each of Mg and Na; and 0.01 to 0.1% each of Al, Ba, Ge, Fe, Si, and Sr.
Temperature of data collection: Pattern taken at 25 C.
Additional pattern: To replace 3-736, 34-11 and 35-496.
Data collection flag: Ambient.

Natl. Bur. Stand. (U.S.) Monogr. 25, volume 3, page 22 (1964)

Radiation : CuKa1
Lambda : 1.54056
SS/FOM : F30=73(0.0121,34)

Filter : Beta
d-sp : Diffractometer
Internal standard : W

2th	i	h	k	l
10.887	8	1	0	0
16.874	4	1	0	1
18.931	1	1	1	0
21.901	8	2	0	0
22.950	8	1	1	1
25.473	1	2	0	1
25.864	40	0	0	2
28.154	14	1	0	2
29.092	18	2	1	0
31.937	100	2	1	1
32.268	55	1	1	2
33.128	60	3	0	0
34.142	30	2	0	2
35.641	6	3	0	1
39.330	8	2	1	2
40.041	20	3	1	0
40.644	4	2	2	1
42.195	6	3	1	1
42.444	4	3	0	2
43.994	6	1	1	3
44.647	2	4	0	0
45.378	4	2	0	3
46.866	25	2	2	2
48.267	14	3	1	2
48.874	4	3	2	0
49.584	30	2	1	3
50.765	16	3	2	1
51.564	14	4	1	0
52.294	14	4	0	2
53.145	16	0	0	4
54.442	1	1	0	4
56.141	6	3	2	2
57.285	4	3	1	3
58.357	2	5	0	1
59.096	1	3	3	0
60.285	6	4	2	0
60.722	4	3	3	1
61.753	4	2	1	4
61.936	4	4	2	1
63.300	8	5	0	2

Figure 4.8 JCDPS sheet of fluorapatite

4.3 Analysis of the specimens before immersion into simulated body fluid (SBF)

4.3.1 X-ray diffraction analysis of Co-Cr-Mo alloy coated with fluorapatite, $Ca_{10}(PO_4)_6F_2$.

The plot as a spectrum of the X-ray diffraction data obtained by the irradiation of the specimen of which the synthesized fluorapatite powder that has been deposited onto Co-Cr-Mo by pulsed laser deposition is shown in figure 4.9. The laser beam energy was 130 mJ and the pressure was maintained at 7×10^{-9} MPa. The deposition time was 15 minutes.

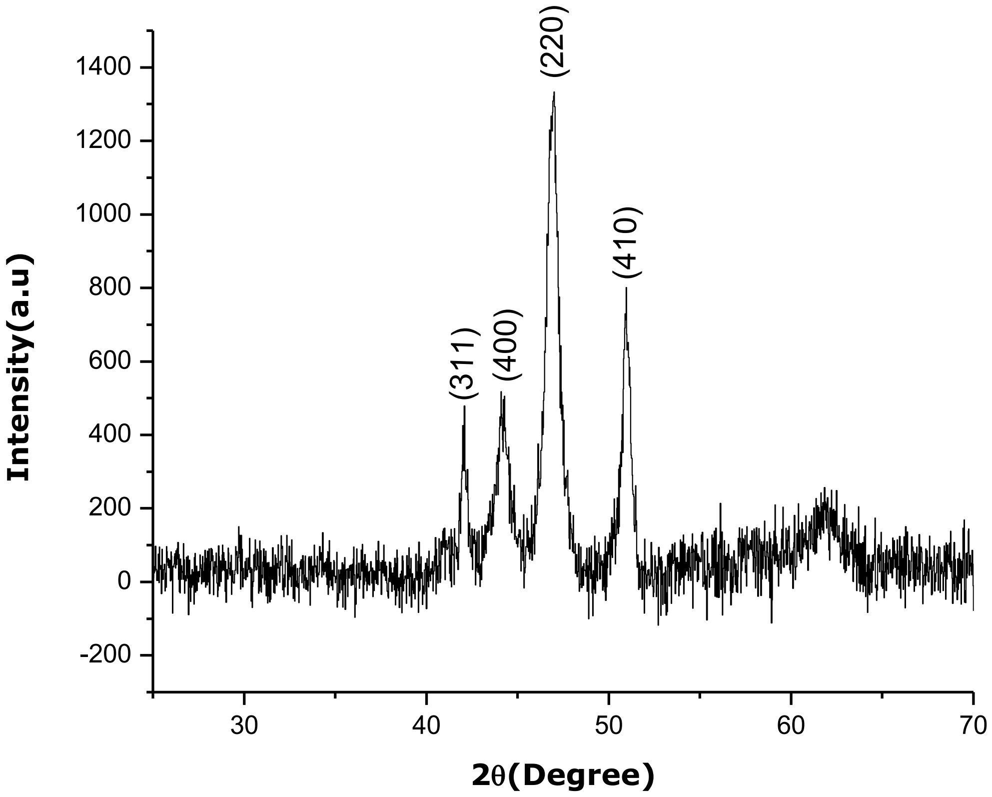

Figure 4.9 The plot as a spectrum of the X-ray diffraction data obtained by the irradiation of the specimen of which the synthesized fluorapatite powder that has been deposited onto Co-Cr-Mo by pulsed laser deposition. The laser beam energy was 130 mJ and the pressure was maintained at 7×10^{-9} MPa. The exposure time was five minutes. The 2θ was varied from a minimum of 10^0 to 100^0.

Distinct diffraction peaks identified are the (311), (400), (220) and (410). The lattice planes reveal that the as–prepared nanocrystals have a cubic structure. As seen in figure 4.13, the (220 CaF_2) reflection is the strongest peak. All the peaks were different, some were sharp and others broad. If the peak is sharp the full width at half maximum (fwhm) is small and the grain size is large. However, if the peak is broad, then the fwhm will be large and the grain size will be small. Hence, the deposited layer has a mixture of small and large grains.

The plot as a spectrum of the X-ray diffraction data obtained by the irradiation of the specimen of which the synthesized fluorapatite powder that has been coated onto the Co-Cr-Mo by pulsed laser deposition, is shown in figure 4.10. The laser beam energy was 130 mJ and the pressure was maintained at 7×10^{-9} MPa. In this instance the irradiation time was 10 minutes. XRD patterns with distinct diffraction peaks, identified to be (400) and (222) are indicated. The (222 CaF_2) reflection is the strongest peak. The fwhm of the peaks indicate that the deposited layer consists of a mixture of small and large grains.

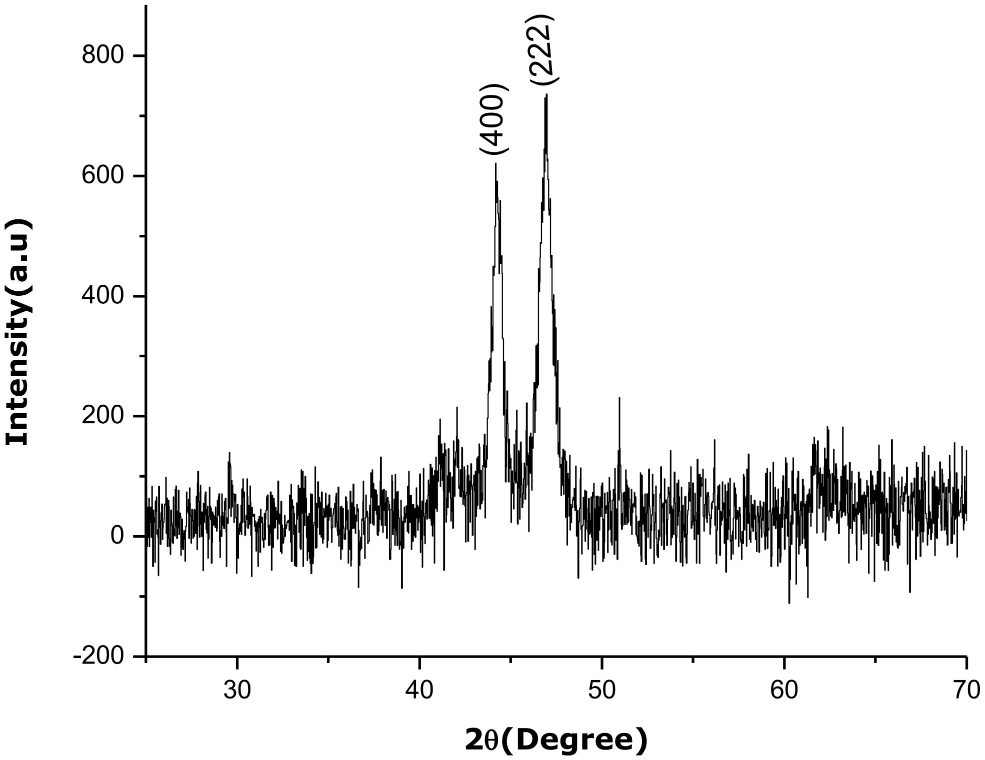

Figure 4.10 The plot as a spectrum of the X-ray diffraction data obtained by the irradiation of the specimen of which the synthesized fluorapatite nanopowder that has been coated onto Co-Cr-Mo by pulsed laser deposition. The laser beam energy was 130 mJ and the pressure was maintained at 7×10^{-9} MPa. The exposure time was 10 minutes. The 2θ was varied from a minimum of 10^0 to 100^0.

The plot as a spectrum of the X-ray diffraction data obtained by the irradiation of the specimen of which the synthesized fluorapatite nanopowder that has been coated onto Co-Cr-Mo by pulsed laser deposition, is shown in figure 4.11. The laser beam energy was 130 mJ and the pressure was maintained at 7×10^{-9} MPa. The irradiation time in this instance was 20 minutes. XRD patterns with distinct diffraction peaks, identified to be (400) and (222) are indicated. The (222 CaF_2) reflection is the strongest peak. The fwhm of the peaks indicate that the deposited layer consists of a mixture of small and large grains.

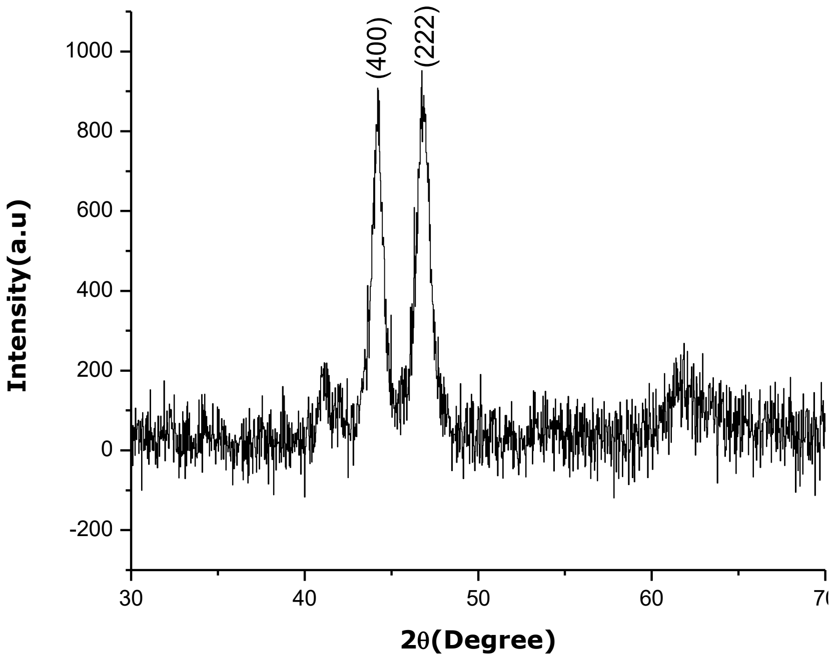

Figure 4.11 The plot as a spectrum of the X-ray diffraction data obtained by the irradiation of the specimen of which the synthesized fluorapatite nanopowder that has been coated onto Co-Cr-Mo by pulsed laser deposition. The laser beam energy was 130 mJ and the pressure was maintained at 7×10^{-9} MPa. The exposure time was 20 minutes.

In figure 4.12 is shown the plot as a spectrum of the X-ray diffraction data obtained by the irradiation of the specimen of which the synthesized fluorapatite nanopowder that has

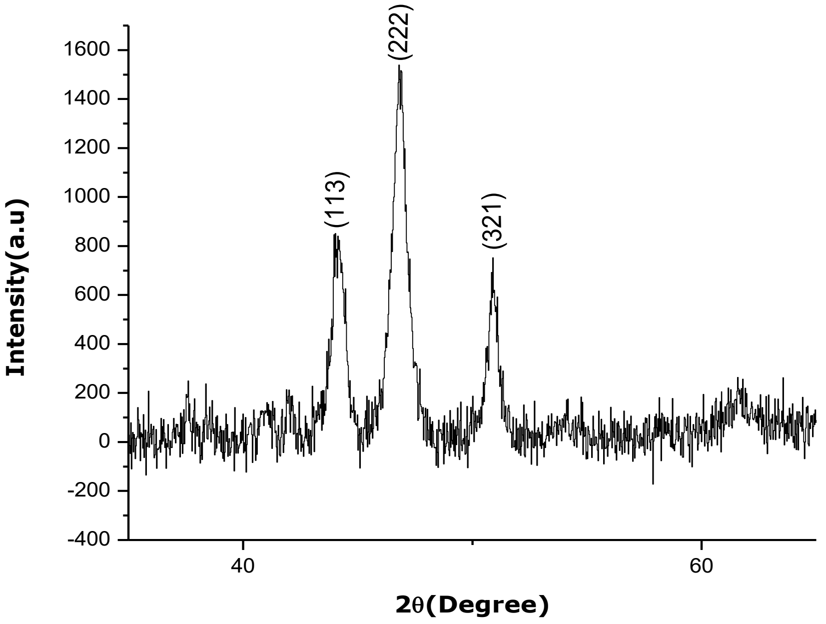

Figure 4.12 The plot as a spectrum of the X-ray diffraction data obtained by the irradiation of the specimen of which the synthesized fluorapatite nanopowder that has been coated onto Co-Cr-Mo by

pulsed laser deposition. The laser beam energy was 170 mJ and the pressure was maintained at 7×10^{-9} MPa. The irradiation time was 10 minutes.

been coated onto Co-Cr-Mo by pulsed laser deposition. The laser beam energy was 170 mJ and the pressure was maintained at 7×10^{-9} MPa. The exposure time was 10 minutes. The 2θ was varied from a minimum of 10^0 to 100^0, where necessary.

XRD patterns with distinct diffraction peaks, identified to be (113), (222) and (321) are indicated. The (222 CaF_2) reflection is the strongest peak. The fwhm of the peaks indicate that the deposited layer consists of a mixture of small and large grains.

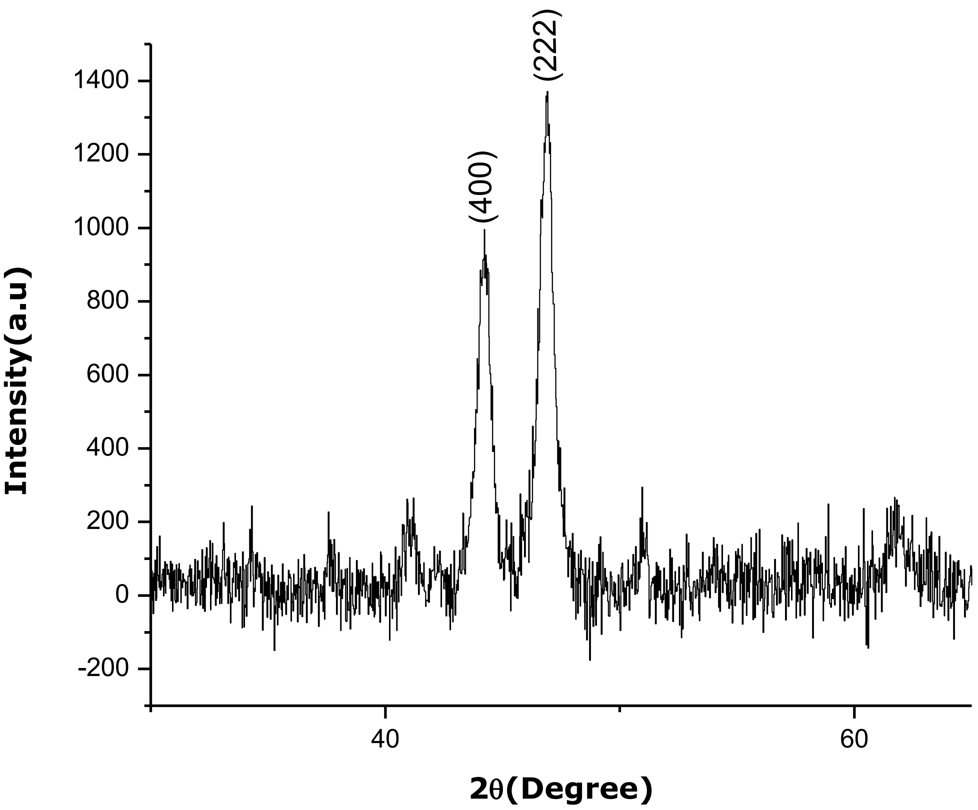

Figure 4.13 The plot as a spectrum of the X-ray diffraction data obtained by the irradiation of the specimen of which the synthesized fluorapatite nanopowder that has been coated onto Co-Cr-Mo by pulsed laser deposition. The laser beam energy was 170 mJ and the pressure was maintained at 7×10^{-9} MPa. The exposure time was 20 minutes.

In figure 4.13 is shown the plot as a spectrum of the X-ray diffraction data obtained by the irradiation of the specimen of which the synthesized fluorapatite nanopowder that has been coated onto Co-Cr-Mo by pulsed laser deposition. The irradiation time period was then increased to 20 minutes. The laser beam energy was 170 mJ and the pressure was maintained at 7×10^{-9} MPa. The 2θ was varied from a minimum of 10^0 to 100^0. XRD patterns with distinct diffraction peaks, identified to be (400) and (222) are indicated. The (222 CaF_2)

reflection is the strongest peak. The fwhm of the peaks indicate that the deposited layer consists of a mixture of small and large grains.

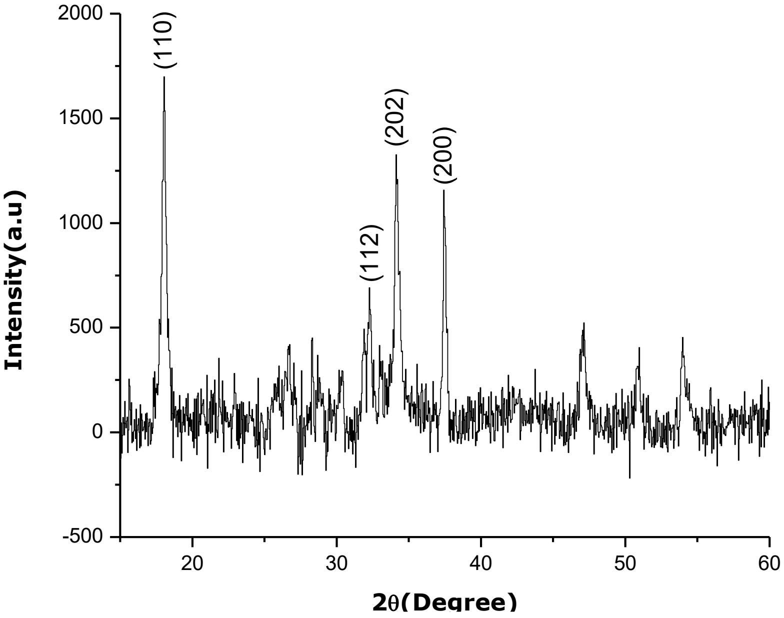

Figure 4.14 The plot as a spectrum of these X-ray diffraction data obtained by the irradiation of the specimen of which the synthesized fluorapatite nanopowder that has been coated onto a glass substrate by pulsed laser deposition. The exposure time period was 20 minutes. The laser beam energy was 170 mJ and the pressure was maintained at 7×10^{-9} MPa. The 2θ was varied from a minimum of 10^0 to 100^0.

In figure 4.14 is shown the plot as a spectrum of the X-ray diffraction data obtained by the irradiation of the specimen of which the synthesized fluorapatite nanopowder that has been coated onto a glass substrate by pulsed laser deposition. The irradiation time period was then increased to 20 minutes. The laser beam energy was 170 mJ and the pressure was maintained at 7×10^{-9} MPa. The 2θ was varied from a minimum of 10^0 to 100^0.

XRD patterns with distinct diffraction peaks, identified to be (110), (112), (202) and (200) are indicated. The (202 CaF_2) reflection is the strongest peak. The fwhm of the peaks indicate that the deposited layer consists of a mixture of small and large grains.

4.3.2 Microstructural topology analysis by scanning electron microscopy (SEM)

Electron micrographs of the microstructural topologies of the specimens in which fluorapatite nanopowder was coated onto the Co-Cr-Mo alloy by pulsed laser deposition are shown in figures 4.15 to 4.21. The laser energies were 130 mJ and 170 mJ and the pressure was maintained at 7×10^{-9} MPa. The exposure times varied from five to 20 minutes. The micrographs were obtained by irradiating the specimens with a beam of electrons of energy

5 keV. The irradiation live-time was 120 seconds. The surface area scanned was approximately 10μm×10μm and where necessary, a larger area was selected. The magnification was 9000× and the working distance was kept at 4.2±0.2 mm.

From figures 4.15 to 4.21, which indicate the deposition of fluorapatite in the alloy at energy 130 mJ, it is noticeable that the density of the deposition increased significantly and is therefore correlated to the exposure time period when the fluorapatite is deposited on the Co-Cr-Mo alloy. It is not at this stage of the analysis ascertainable if this increase in density can be linearly correlated to the exposure time period. In the instance where the energy was 170 mJ, a significant in the density was also observed. The electron micrograph of the surface area of the specimen of deposition of fluorapatite onto glass is shown in figure 4.21.

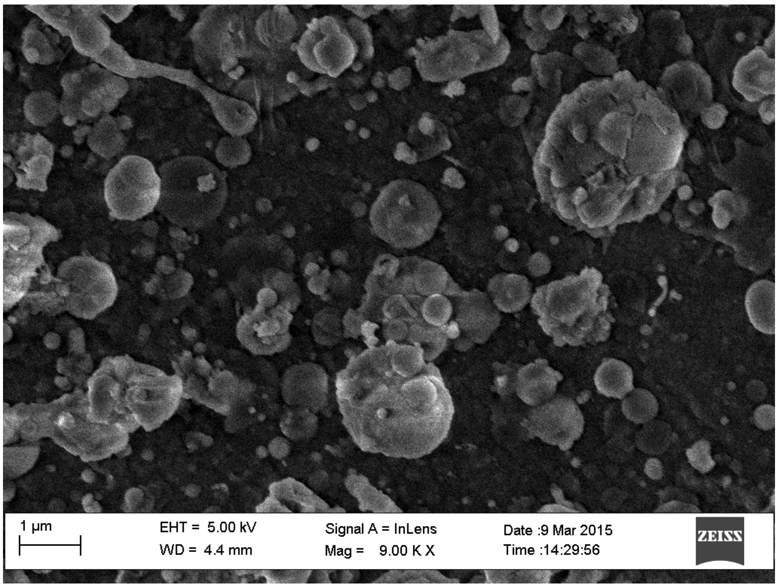

Figure 4.15 Electron micrograph of the microstructural topology of the specimen in which fluorapatite nanopowder was coated onto Co-Cr-Mo alloy by pulsed laser deposition. The laser energy was 130 mJ and the pressure was maintained at 7×10^{-9} MPa. The exposure time was five minutes. The micrograph was obtained by irradiating the specimen with a beam of electrons of energy 5 keV. The irradiation live-time was 120 seconds and the working distance was kept maintained at 4.2±0.2 mm. The surface area scanned was 10μm×10μm and where necessary, a larger area was selected.

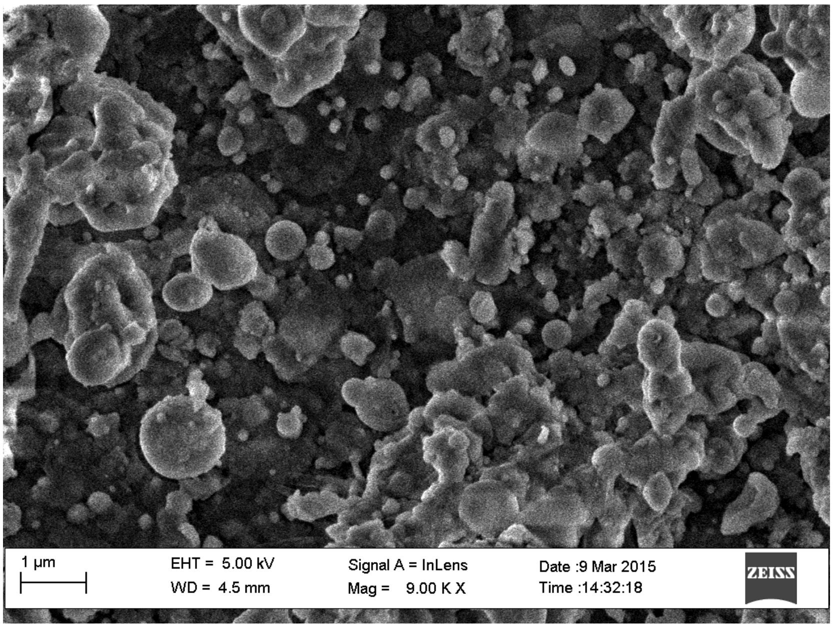

Figure 4.16 Electron micrograph of the microstructural topology of the specimen in which fluorapatite nanopowder was coated onto Co-Cr-Mo alloy by pulsed laser deposition. The laser energy was 130 mJ and the pressure was maintained at 7×10^{-9} MPa. The exposure time was 10 minutes. The micrograph was obtained by irradiating the specimen with a beam of electrons of energy 5 keV. The irradiation live-time was 120 seconds and the working distance was kept maintained at 4.2 ± 0.2 mm. The surface area scanned was 10µm×10µm and where necessary, a larger area was selected.

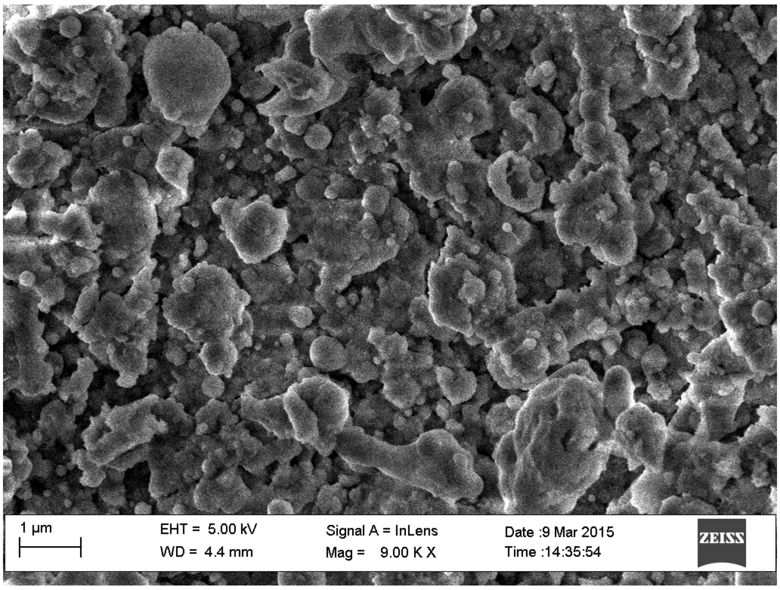

Figure 4.17. Electron micrograph of the microstructural topology of the specimen in which fluorapatite nanopowder was coated onto Co-Cr-Mo alloy by pulsed laser deposition. The laser energy was 130 mJ and the pressure was maintained at 7×10^{-9} MPa. The exposure time was 20 minutes. The micrograph was obtained by irradiating the specimen with a beam of electrons of energy 5 keV. The irradiation live-time was 120 seconds and the working distance was kept maintained at 4.2 ± 0.2 mm. The surface area scanned was 10µm×10µm and where necessary, a larger area was selected.

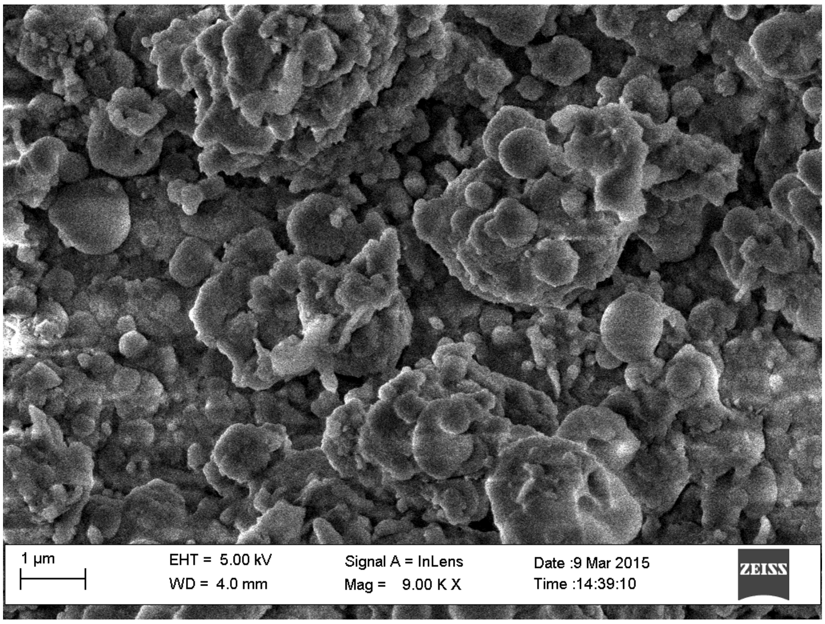

Figure 4.18. Electron micrograph of the microstructural topology of the specimen in which fluorapatite nanopowder was coated onto Co-Cr-Mo alloy by pulsed laser deposition. The laser energy was 170 mJ and the pressure was maintained at 7×10^{-9} MPa. The exposure time was 10 minutes. The micrograph was obtained by irradiating the specimen with a beam of electrons of energy 5 keV. The irradiation live-time was 120 seconds and the working distance was kept maintained at 4.2±0.2 mm. The surface area scanned was 10μm×10μm and where necessary, a larger area was selected.

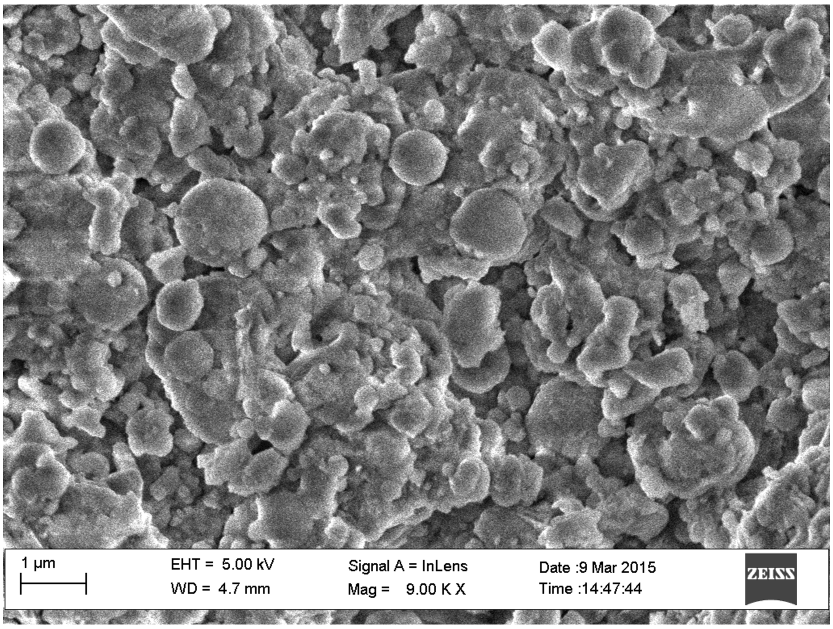

Figure 4.19 Electron micrograph of the microstructural topology of the specimen in which fluorapatite nanopowder was coated onto Co-Cr-Mo alloy by pulsed laser deposition. The laser energy was 170 mJ and the pressure was maintained at 7×10^{-9} MPa. The exposure time was 15 minutes. The micrograph was obtained by irradiating the specimen with a beam of electrons of energy 5 keV. The irradiation live-time was 120 seconds and the working distance was kept maintained at 4.2±0.2 mm. The surface area scanned was 10μm×10μm and where necessary, a larger area was selected.

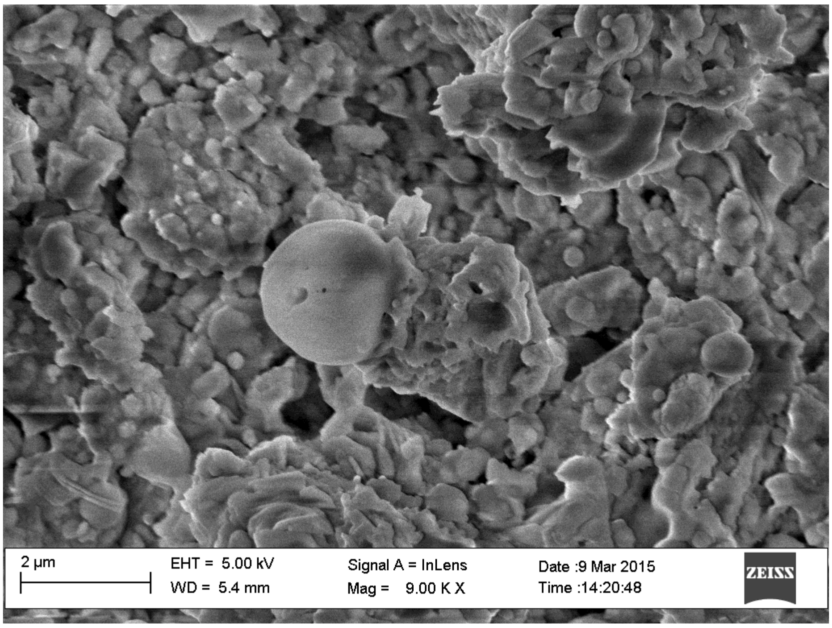

Figure 4.20 Electron micrograph of the microstructural topology of the specimen in which fluorapatite nanopowder was coated onto a glass substrate by pulsed laser deposition. The laser energy was 130 mJ and the pressure was maintained at 7×10^{-9} MPa. The exposure time was 10 minutes. The micrograph was obtained by irradiating the specimen with a beam of electrons of energy 5 keV. The irradiation live-time was 120 seconds and the working distance was kept maintained at 4.2±0.2 mm. The surface area scanned was 10µm×10µm and where necessary, a larger area was selected.

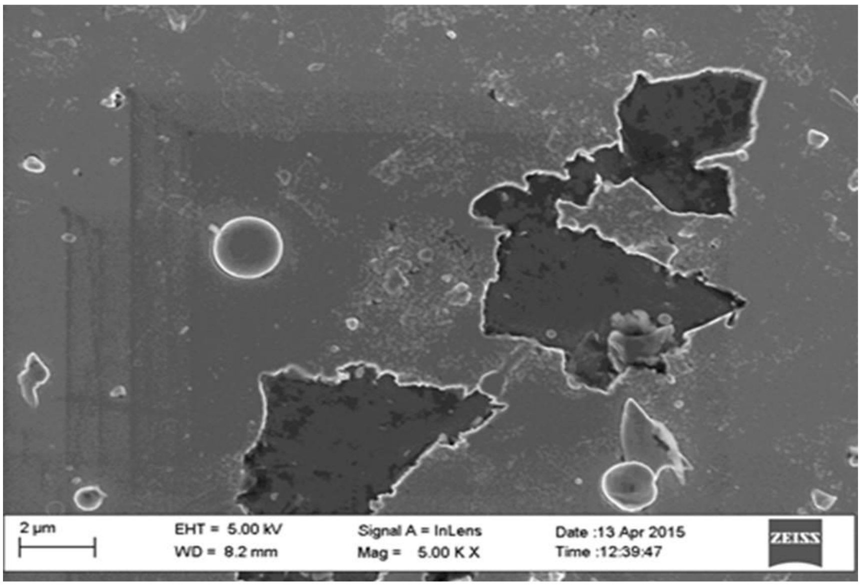

Figure 4.21 Electron micrograph of the microstructural topology of the specimen in which Co-Cr-Mo was coated onto a silicon substrate by pulsed laser deposition. The laser energy was 180 mJ and the pressure was maintained at 7×10^{-9} MPa. The exposure time was 20 minutes. The micrograph was obtained by irradiating the specimen with a beam of electrons of energy 5 keV. The irradiation live-time was 120 seconds and the working distance was kept maintained at 4.2±0.2 mm. The surface area scanned was 10µm×10µm and where necessary, a larger area was selected.

4.3.3 Energy dispersive analysis of X-rays (EDAX) analysis

The energy dispersive analysis of X-rays (EDAX) analysis (shown in figures 4.22 to 4.28) of the specimens in which fluorapatite nanopowder was coated onto the Co-Cr-Mo alloy by pulsed laser deposition are shown in figures 4.22 to 4.28. The laser energy was 130 mJ and 170 mJ and the pressure was maintained at 7×10^{-9} MPa. The exposure times varying from five to 20 minutes. The micrographs were obtained by irradiating the specimens with a beam of electrons of energy 5 keV. The irradiation live-time was 120 seconds. The surface area scanned was approximately 10μm×10μm and where necessary, a larger area was selected.

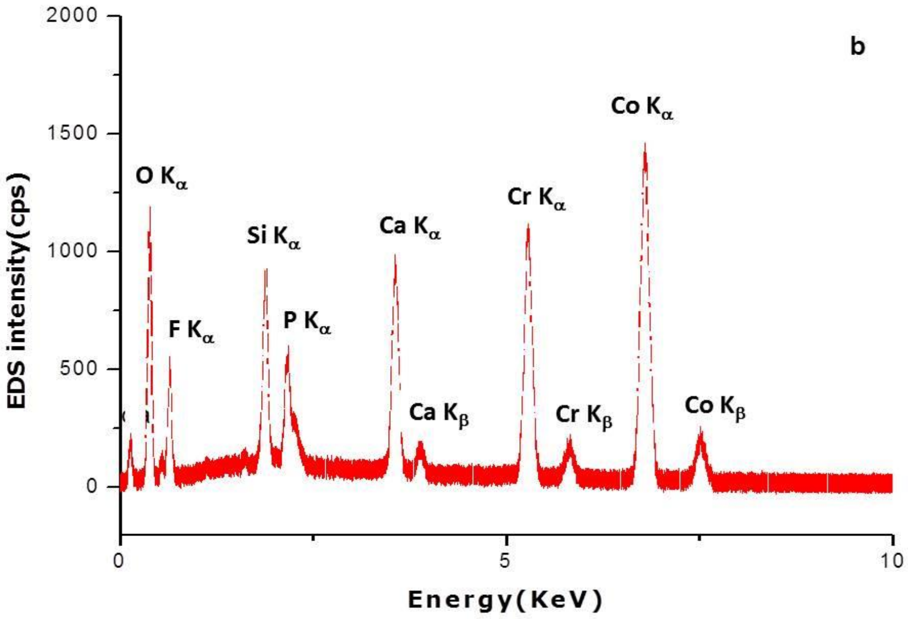

Figure 4.22 The energy dispersive analysis of X-rays (EDAX) analysis of the specimen in which fluorapatite nanopowder was coated onto Co-Cr-Mo alloy by pulsed laser deposition. In the specimen preparation the laser energy was 130 mJ and the pressure was maintained at 7×10^{-9} MPa. The exposure time in the specimen preparation was five minutes. The EDAX analysis was obtained by irradiating the specimen with a beam of electrons of energy 20 keV. The irradiation live-time was 120 seconds. The data were measured with a silicon ultra-thin window (SUTW).

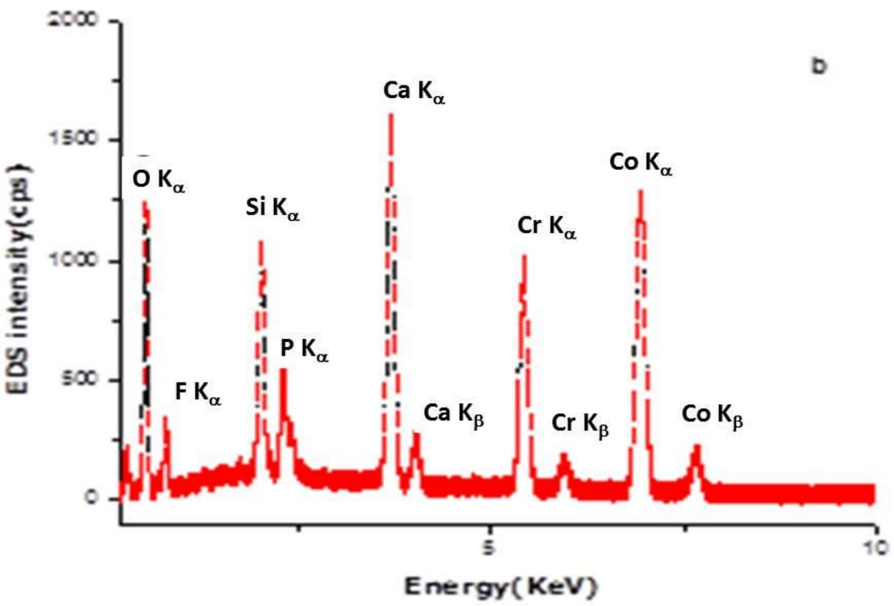

Figure 4.23 The energy dispersive analysis of X-rays (EDAX) analysis of the specimen in which fluorapatite nanopowder was coated onto Co-Cr-Mo alloy by pulsed laser deposition. In the specimen preparation the laser energy was 130 mJ and the pressure was maintained at 7×10^{-9} MPa. The exposure time in the specimen preparation was 10 minutes. The EDAX analysis was obtained by irradiating the specimen with a beam of electrons of energy 20 keV. The irradiation live-time was 120 seconds. The data were measured with a silicon ultra-thin window (SUTW).

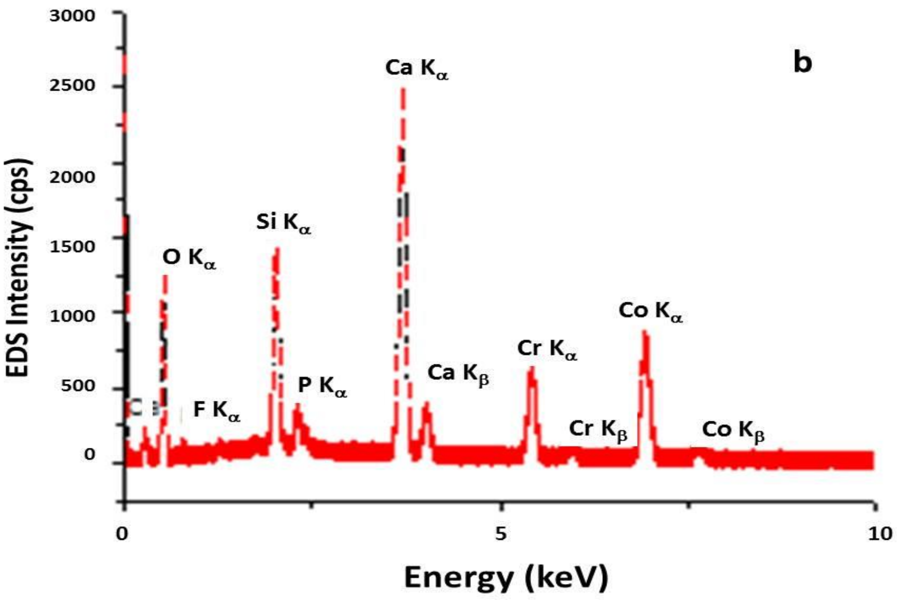

Figure 4.24 The energy dispersive analysis of X-rays (EDAX) analysis of the specimen in which fluorapatite nanopowder was coated onto Co-Cr-Mo alloy by pulsed laser deposition. In the specimen preparation the laser energy was 130 mJ and the pressure was maintained at 7×10^{-9} MPa. The exposure time in the specimen preparation was 20 minutes. The EDAX analysis was obtained by irradiating the specimen with a beam of electrons of energy 20 keV. The irradiation live-time was 120 seconds. The data were measured with a silicon ultra-thin window (SUTW).

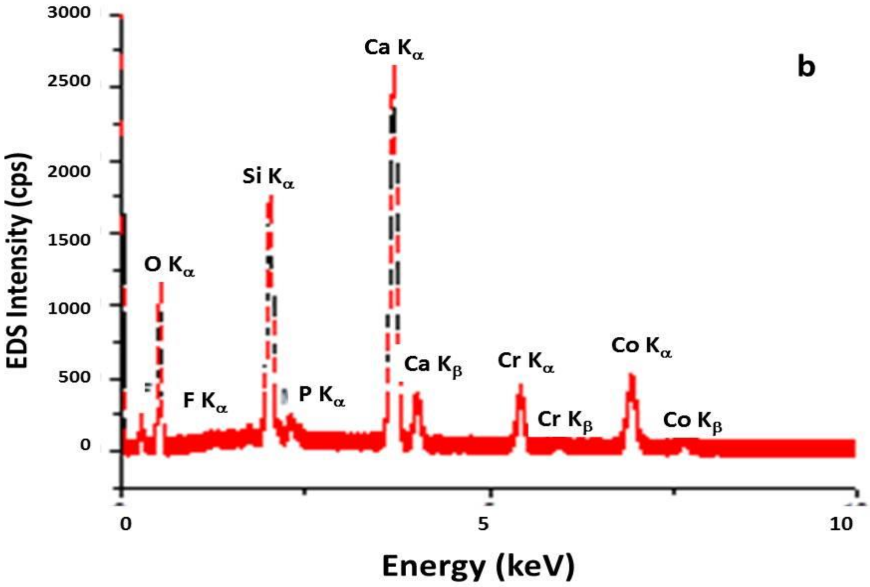

Figure 4.25 The energy dispersive analysis of X-rays (EDAX) analysis of the specimen in which fluorapatite nanopowder was coated onto Co-Cr-Mo alloy by pulsed laser deposition. In the specimen preparation the laser energy was 170 mJ and the pressure was maintained at 7×10^{-9} MPa. The exposure time in the specimen preparation was 10 minutes. The EDAX analysis was obtained by irradiating the specimen with a beam of electrons of energy 20 keV. The irradiation live-time was 120 seconds. The data were measured with a silicon ultra-thin window (SUTW).

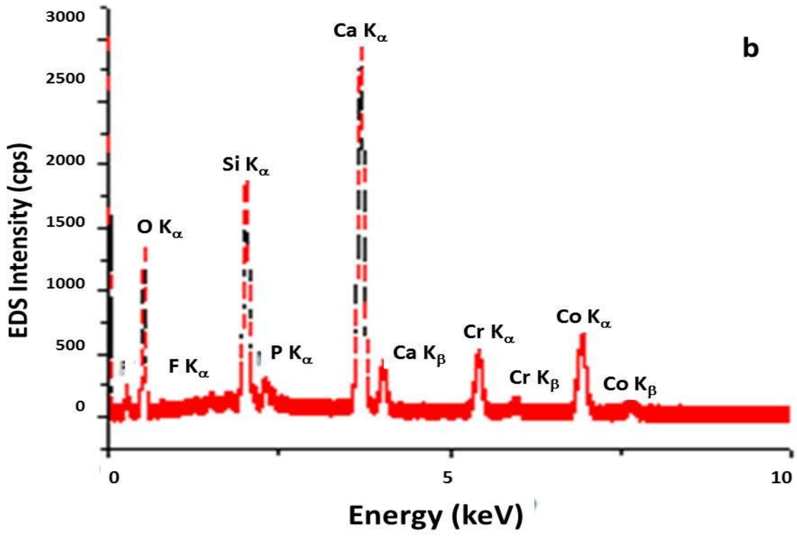

Figure 4.26 The energy dispersive analysis of X-rays (EDAX) analysis of the specimen in which fluorapatite nanopowder was coated onto Co-Cr-Mo alloy by pulsed laser deposition. In the specimen preparation the laser energy was 170 mJ and the pressure was maintained at 7×10^{-9} MPa. The exposure time in the specimen preparation was 15 minutes. The EDAX analysis was obtained by irradiating the specimen with a beam of electrons of energy 20 keV. The irradiation live-time was 120 seconds. The data were measured with a silicon ultra-thin window (SUTW).

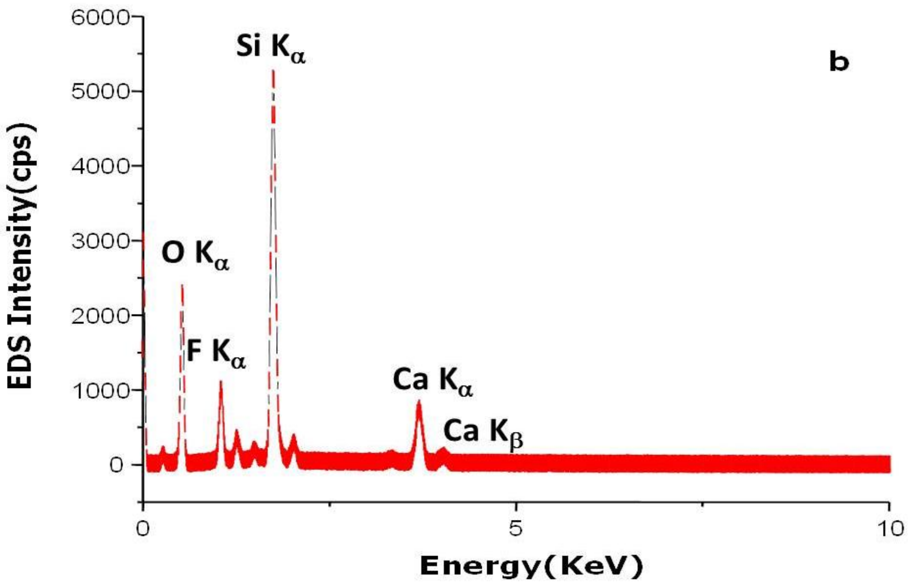

Figure 4.27 The energy dispersive analysis of X-rays (EDAX) analysis of the specimen in which fluorapatite nanopowder was coated onto a glass substrate by pulsed laser deposition. In the specimen preparation the laser energy was 130 mJ and the pressure was maintained at 7×10^{-9} MPa. The exposure time in the specimen preparation was 10 minutes. The EDAX analysis was obtained by irradiating the specimen with a beam of electrons of energy 20 keV. The irradiation live-time was 120 seconds. The data were measured with a silicon ultra-thin window (SUTW).

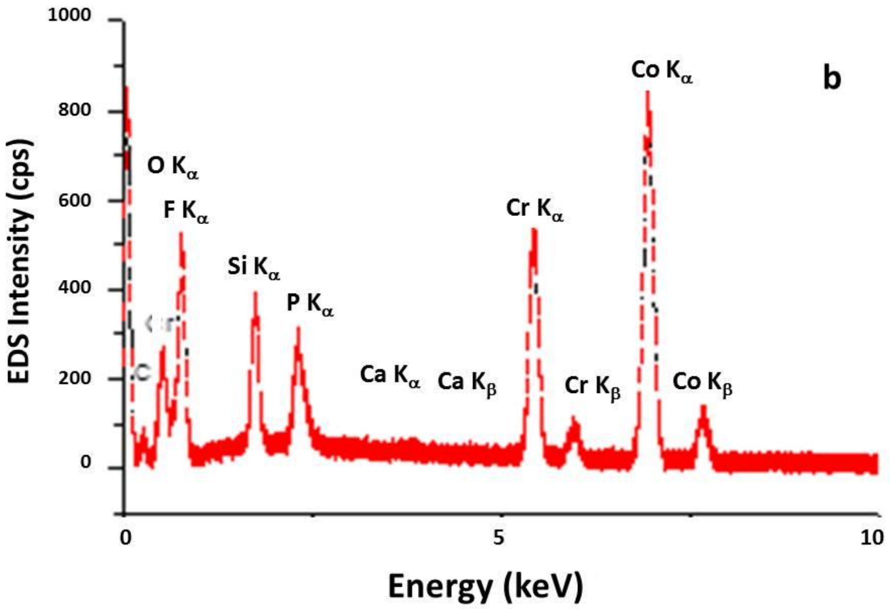

Figure 4.28 The energy dispersive analysis of X-rays (EDAX) analysis of the specimen in which Co-Cr-Mo alloy was deposited on a silicon substrate by pulsed laser deposition. In the specimen preparation the laser energy was 180 mJ and the pressure was maintained at 7×10^{-9} MPa. The exposure time in the specimen preparation was 20 minutes. The EDAX analysis was obtained by irradiating the specimen with a beam of electrons of energy 20 keV. The irradiation live-time was 120 seconds. The data were measured with a silicon ultra-thin window (SUTW).

At constant laser beam energy, it is expected that the thickness of the deposited layer will increase with increase in exposure time. In addition, the energy of the electron beam was kept constant at 20 keV and hence the thickness of the layer can be evaluated by considering the ratio of concentration of Ca which is present in the fluorapatite matrix, to the concentration of Cr which is present in the alloy matrix.

Thus, as the beam penetrates the deposited layer, it samples the concentration at depth. A small ratio of Ca to Cr will be indicative of a very thin layer. Neglecting the full width at half maximum of the peaks, this ratio can be calculated based on the intensity of the K_α lines of these elements. For an exposure time of five minutes, this ratio is 0.91; for an exposure time of 10 minutes the ratio is 1.63 and for 20 minutes, the ratio is 5.00. From these calculations it is evident that the growth in thickness of the layer is correlated, and however not linearly.

Since Ca might be present in glass, although be it is small concentrations, the ratio of the concentration of Cato that of Cr cannot be used to evaluate the thick thickness of the layer. The oxygen concentration can also not be used since it is present in the glass. From figure 4.27, and quantification with the manufacturer computational software, the intensity of the peak of the P K_α line is very small. Thus only the intensity of the K_α line of F can be used. Since the concentration of F in the fluorapatite is relatively small, 2%, the ratio of its concentration with that of Si present in the glass matrix should be relatively big. This ratio is approximately 6 and hence the thickness of the layer of fluorapatite deposited in the glass is relatively thick.

4.3.4 Atomic force microscopic analysis, rendered as a three dimensional (3-D) image, of the degree of surface roughness.

The microstructural topologies of the specimens that have been shown before only entails the 2-dimensional image of the surface. More so, the extent of the roughness can therefore not be evaluated. For this reason, atomic force microscopic analyses were performed. These 3-dimensional images are shown in figures 4.29 to 4.35.

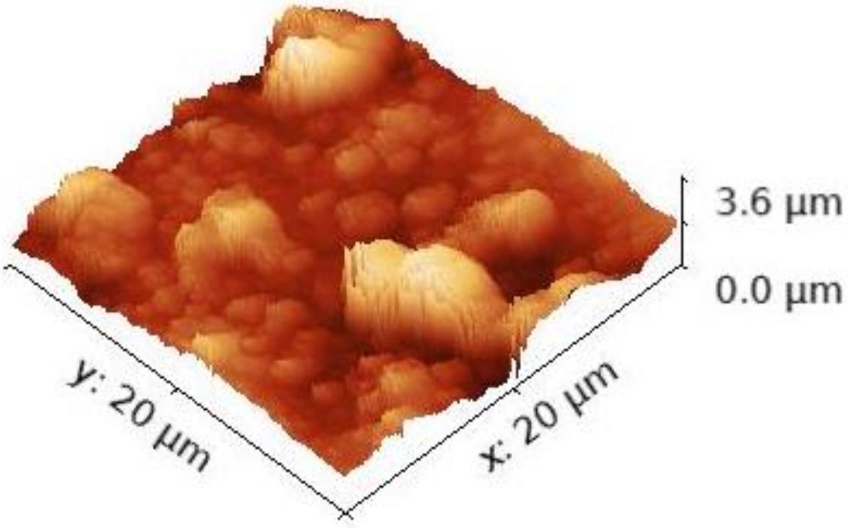

Figure 4.29 Atomic force microscopic analysis, rendered as a three dimensional (3-D) image, of the degree of surface roughness of the specimens in which fluorapatite was deposited onto a Co-Cr-Mo alloy by pulsed laser deposition. During the deposition, the laser energy was 130 mJ and the pressure was maintained at 7×10^{-9} MPa and during which the exposure time was five minutes.

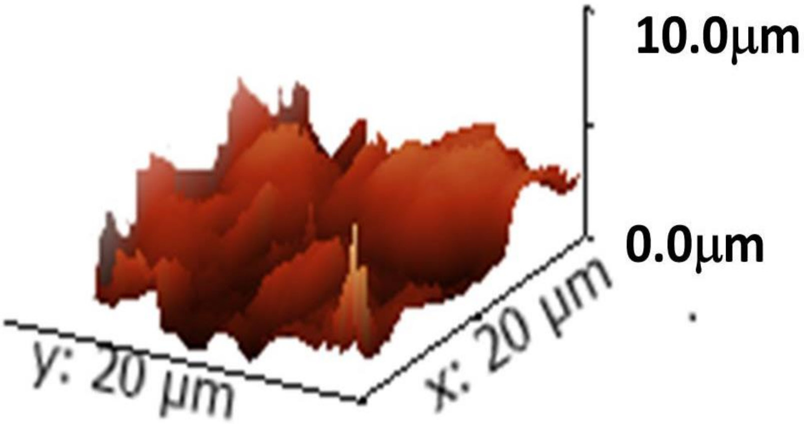

Figure 4.30 Atomic force microscopic analysis, rendered as a three dimensional (3-D) image, of the degree of surface roughness of the specimens in which fluorapatite was deposited onto a Co-Cr-Mo alloy by pulsed laser deposition. During the deposition, the laser energy was 130 mJ and the pressure was maintained at 7×10^{-9} MPa and during which the exposure time was 10 minutes.

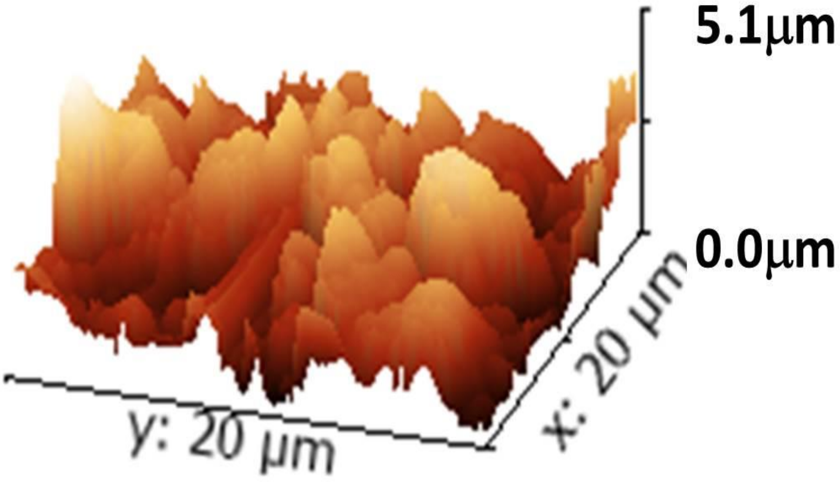

Figure 4.31 Atomic force microscopic analysis, rendered as a three dimensional (3-D) image, of the degree of surface roughness of the specimens in which fluorapatite was deposited onto a Co-Cr-Mo alloy by pulsed laser deposition. During the deposition, the laser energy was 130 mJ and the pressure was maintained at 7×10^{-9} MPa and during which the exposure time was 20 minutes.

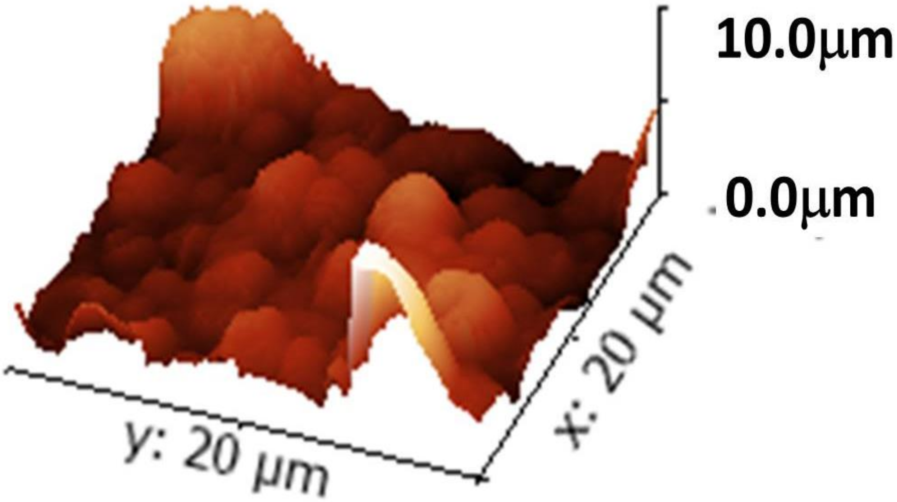

Figure 4.32 Atomic force microscopic analysis, rendered as a three dimensional (3-D) image, of the degree of surface roughness of the specimens in which fluorapatite was deposited onto a Co-Cr-Mo alloy by pulsed laser deposition. During the deposition, the laser energy was 170 mJ and the pressure was maintained at 7×10^{-9} MPa and during which the exposure time was 10 minutes.

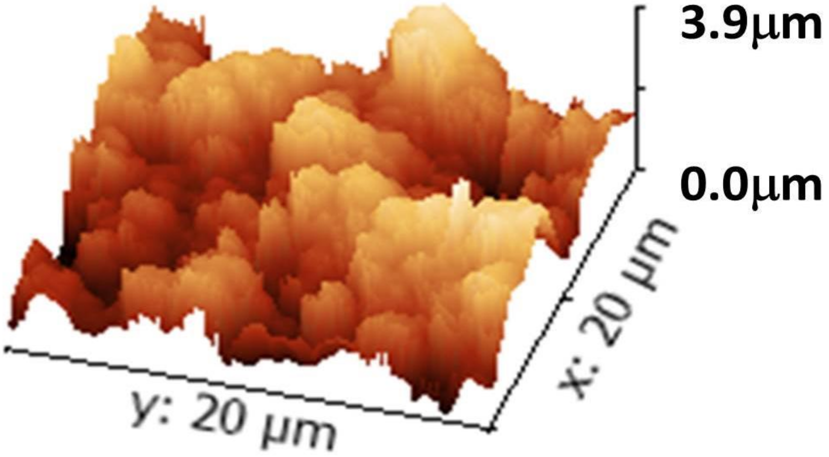

Figure 4.33 Atomic force microscopic analysis, rendered as a three dimensional (3-D) image, of the degree of surface roughness of the specimens in which fluorapatite was deposited onto a Co-Cr-Mo alloy by pulsed laser deposition. During the deposition, the laser energy was 170 mJ and the pressure was maintained at 7×10^{-9} MPa and during which the exposure time was 15 minutes.

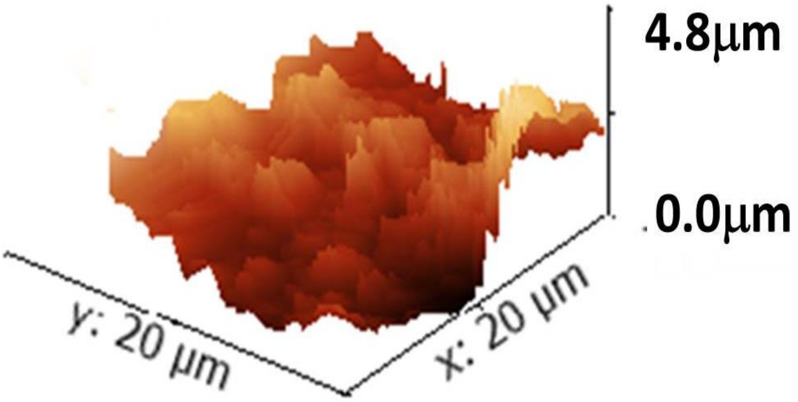

Figure 4.34 Atomic force microscopic analysis, rendered as a three dimensional (3-D) image, of the degree of surface roughness of the specimens in which fluorapatite was deposited onto a glass substrate by pulsed laser deposition. During the deposition, the laser energy was 130 mJ and the pressure was maintained at 7×10^{-9} MPa and during which the exposure time was 10 minutes.

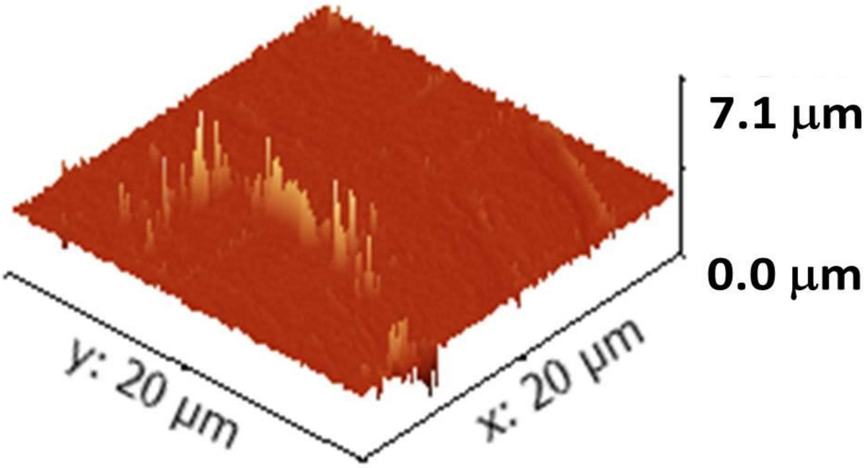

Figure 4.35 Atomic force microscopic analysis, rendered as a three dimensional (3-D) image, of the degree of surface roughness of the specimens in which Co-Cr-Mo alloy was deposited onto a silicon substrate by pulsed laser deposition. During the deposition, the laser energy was 180 mJ and the pressure was maintained at 7×10^{-9} MPa and during which the exposure time was 20 minutes.

The parameters determined based on equations 1, 2 and 3, are discussed in **table 4.1** on **page 79**. The was done to ease the comparison of the values in the case of the before and after submersion into the SBF.

4.4 Instrumental analysis of the specimens after immersion into simulated body fluid (SBF)

4.4.1 Microstructural topology analysis by scanning electron microscopy (SEM)

Electron micrographs of the microstructural topologies of the specimens in which fluorapatite nanopowder was coated onto the Co-Cr-Mo alloy by pulsed laser deposition are shown in figures 4.36 to 4.41. The laser energies were 130 mJ and 170 mJ and the pressure was maintained at 7×10^{-9} MPa. The exposure times varied from five to 20 minutes. The micrographs were obtained by irradiating the specimens with a beam of electrons of energy 5 keV. The irradiation live-time was 120 seconds. The surface area scanned was approximately 10µm×10µm and where necessary, a larger area was selected. The magnification was 9000× and the working distance was kept at 4.2±0.2 mm.

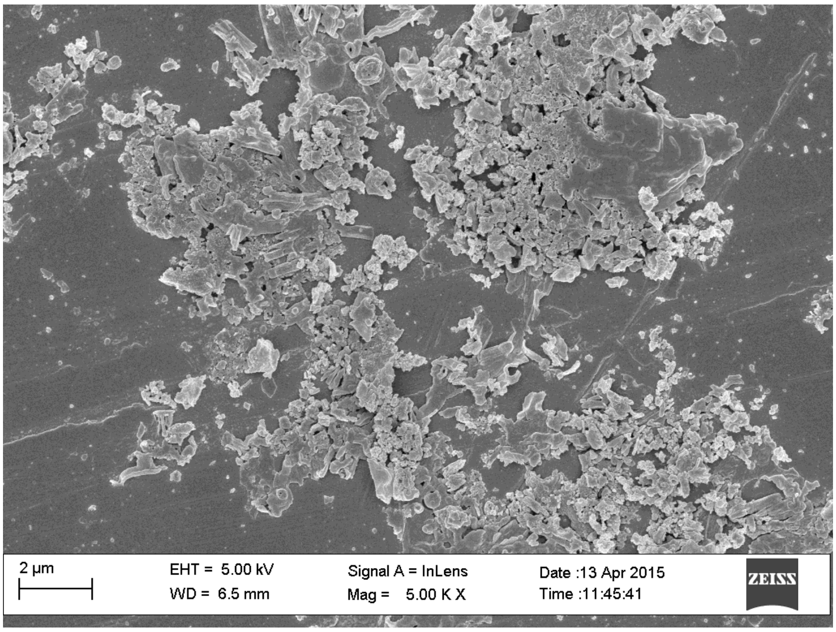

Figure 4.36 Electron micrograph of the microstructural topology of the specimen in which fluorapatite nanopowder was coated onto Co-Cr-Mo alloy by pulsed laser deposition. The laser energy was 130 mJ and the pressure was maintained at 7×10^{-9} MPa. The exposure time was five minutes. The micrograph was obtained by irradiating the specimen with a beam of electrons of energy 5 keV. The irradiation live-time was 120 seconds and the working distance was kept maintained at 4.2ffi0.2 mm. The surface area scanned was 10µm×10µm and where necessary, a larger area was selected.

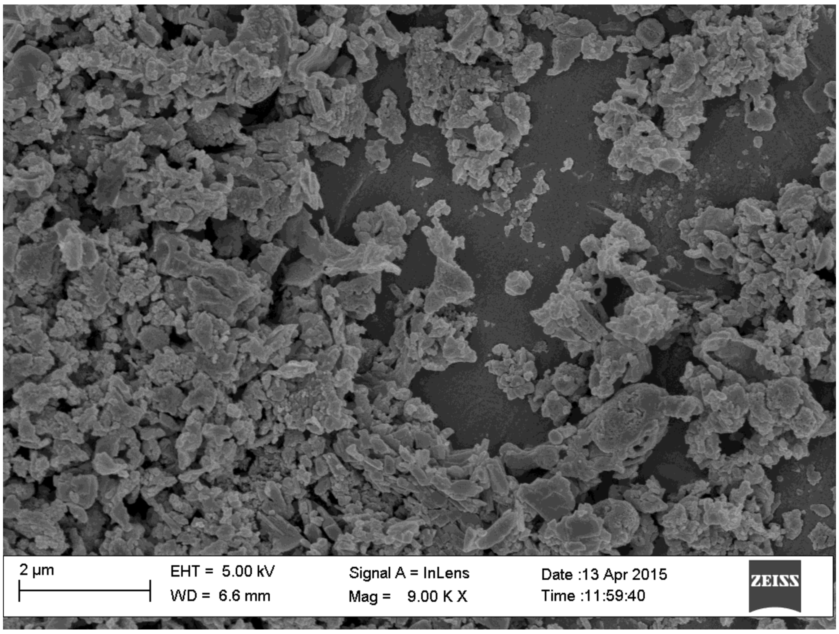

Figure 4.37 Electron micrograph of the microstructural topology of the specimen in which fluorapatite nanopowder was coated onto Co-Cr-Mo alloy by pulsed laser deposition. The laser energy was 130 mJ and the pressure was maintained at 7×10^{-9} MPa. The exposure time was 10 minutes. The micrograph was obtained by irradiating the specimen with a beam of electrons of energy 5 keV. The irradiation live-time was 120 seconds and the working distance was kept maintained at 4.2ffi0.2 mm. The surface area scanned was 10µm×10µm and where necessary, a larger area was selected.

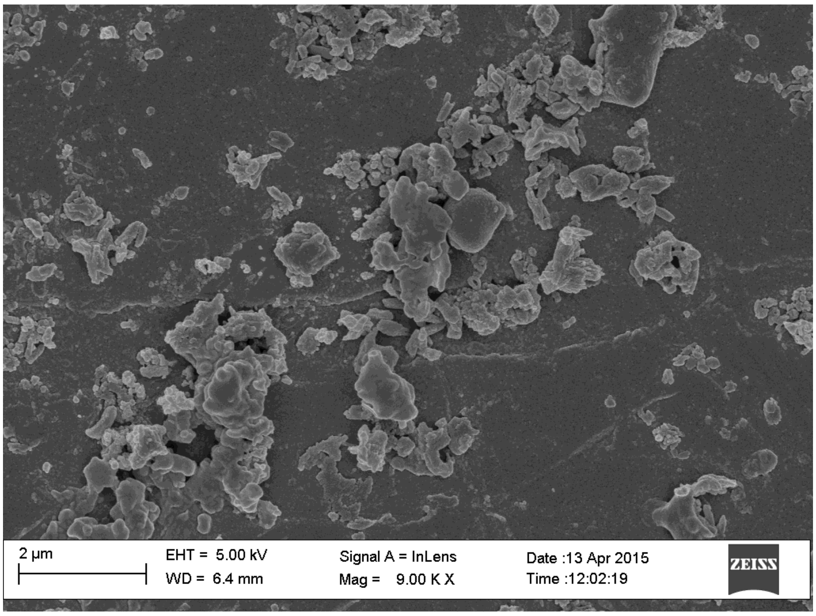

Figure 4.38 Electron micrograph of the microstructural topology of the specimen in which fluorapatite nanopowder was coated onto Co-Cr-Mo alloy by pulsed laser deposition. The laser energy was 130 mJ and the pressure was maintained at 7×10^{-9} MPa. The exposure time was 20 minutes. The micrograph was obtained by irradiating the specimen with a beam of electrons of energy 5 keV. The irradiation live-time was 120 seconds and the working distance was kept maintained at 4.2ffi0.2 mm. The surface area scanned was 10µm×10µm and where necessary, a larger area was selected.

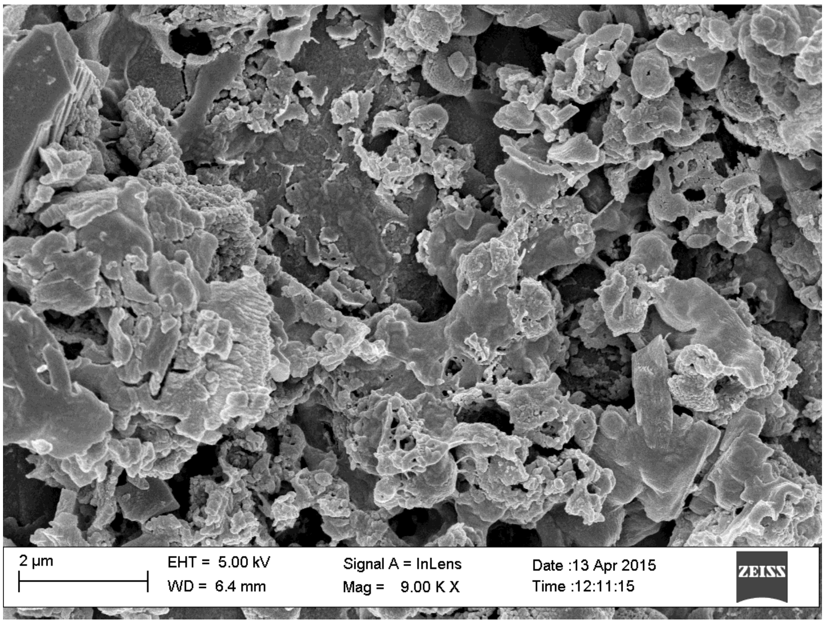

Figure 4.39 Electron micrograph of the microstructural topology of the specimen in which fluorapatite nanopowder was coated onto Co-Cr-Mo alloy by pulsed laser deposition. The laser energy was 170 mJ and the pressure was maintained at 7×10^{-9} MPa. The exposure time was 10 minutes. The micrograph was obtained by irradiating the specimen with a beam of electrons of energy 5 keV. The irradiation live-time was 120 seconds and the working distance was kept maintained at 4.2±0.2 mm. The surface area scanned was 10µm×10µm and where necessary, a larger area was selected.

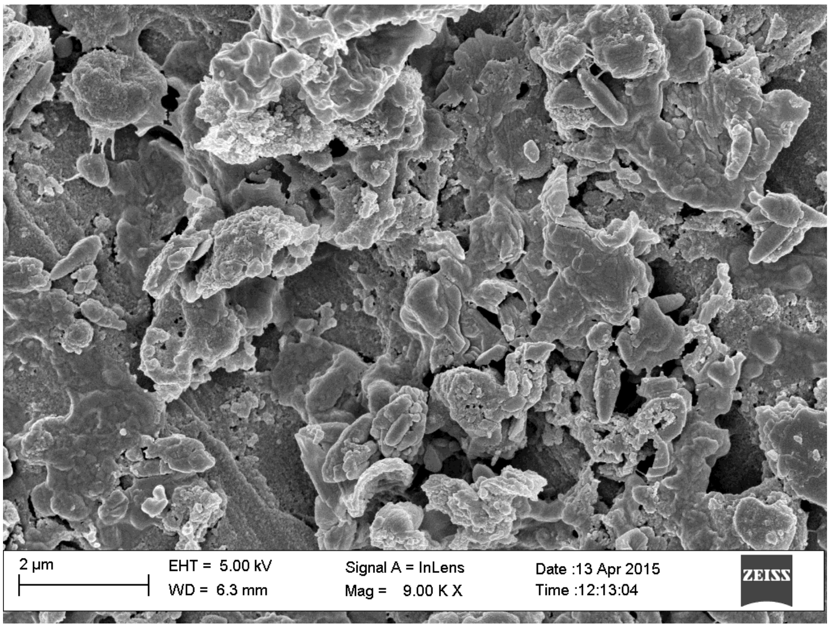

Figure 4.40 Electron micrograph of the microstructural topology of the specimen in which fluorapatite nanopowder was coated onto Co-Cr-Mo alloy by pulsed laser deposition. The laser energy was 170 mJ and the pressure was maintained at 7×10^{-9} MPa. The exposure time was 15 minutes. The micrograph was obtained by irradiating the specimen with a beam of electrons of energy 5 keV. The irradiation live-time was 120 seconds and the working distance was kept maintained at 4.2±0.2 mm. The surface area scanned was 10μm×10μm and where necessary, a larger area was selected.

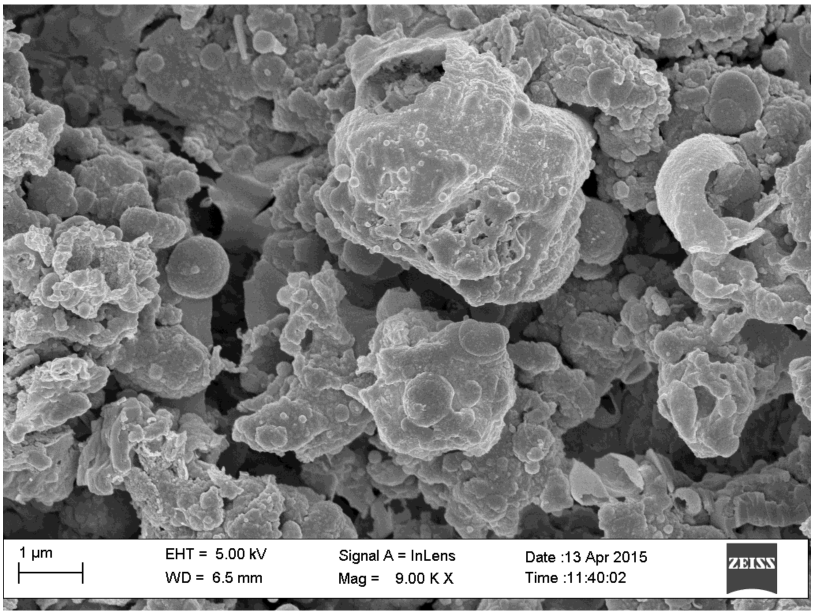

Figure 4.41 Electron micrograph of the microstructural topology of the specimen in which fluorapatite nanopowder was coated onto a glass substrate by pulsed laser deposition. The laser energy was 130 mJ and the pressure was maintained at 7×10^{-9} MPa. The exposure time was 10 minutes. The micrograph was obtained by irradiating the specimen with a beam of electrons of energy 5 keV. The irradiation live-time was 120 seconds and the working distance was kept maintained at 4.2±0.2 mm. The surface area scanned was 10μm×10μm and where necessary, a larger area was selected.

A significant degree of agglomeration occurred in the specimen prepared at 130mJ energy and an exposure time period of five minutes. Voids (only the Co-Cr-Mo alloy surface visible) areas were observed. This is indicative of the depletion of the deposited layer. A similar phenomenon occurred in the instance of the specimen prepared at the same energy but for an exposure time of 10 minutes. The extent of depletion of the deposited layer is however not as extensive as in the case of the specimen irradiated for five minutes. As the layer thickness increased, the extent of depletion of the deposited layer decreased.

4.4.2 Energy dispersive analysis of X-rays (EDAX) analysis

The energy dispersive analysis of X-rays (EDAX) analysis (shown in figures 4.34 to 4.39) of the specimens in which fluorapatite nanopowder was coated onto the Co-Cr-Mo alloy by pulsed laser deposition are shown in figures 4.34 to 4.39. The laser energy was set at 130 mJ and 170 mJ and the pressure was maintained at 7×10^{-9} MPa. The exposure times varied from five to 20 minutes. The micrographs were obtained by irradiating the specimens with a beam of electrons of energy 5 keV. The irradiation live-time was 120 seconds. The surface area scanned was approximately 10μm×10μm and where necessary, a larger area was selected.

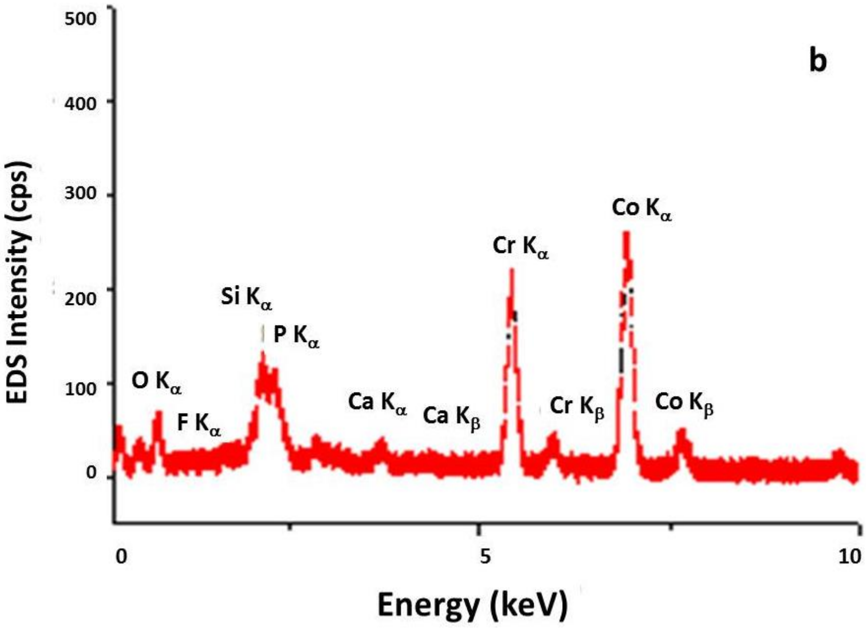

Figure 4.42 The energy dispersive analysis of X-rays (EDAX) analysis of the specimen in which fluorapatite nanopowder was coated onto Co-Cr-Mo alloy by pulsed laser deposition. In the specimen preparation the laser energy was 130 mJ and the pressure was maintained at 7×10^{-9} MPa. The exposure time in the specimen preparation was five minutes. The EDAX analysis was obtained by irradiating the specimen with a beam of electrons of energy 20 keV. The irradiation live-time was 120 seconds. The data were measured with a silicon ultra-thin window (SUTW).

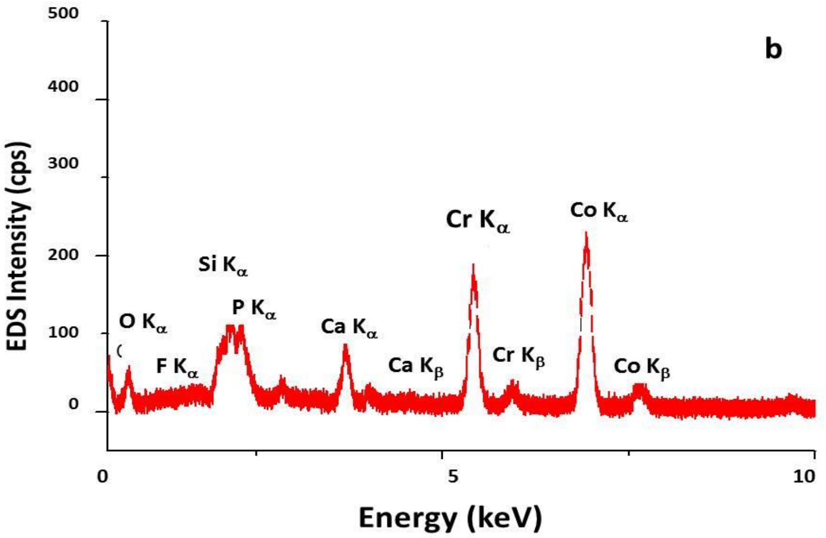

Figure 4.43 The energy dispersive analysis of X-rays (EDAX) analysis of the specimen in which fluorapatite nanopowder was coated onto Co-Cr-Mo alloy by pulsed laser deposition. In the specimen preparation the laser energy was 130 mJ and the pressure was maintained at 7×10^{-9} MPa. The exposure time in the specimen preparation was 10 minutes. The EDAX analysis was obtained by irradiating the specimen with a beam of electrons of energy 20 keV. The irradiation live-time was 120 seconds. The data were measured with a silicon ultra-thin window (SUTW).

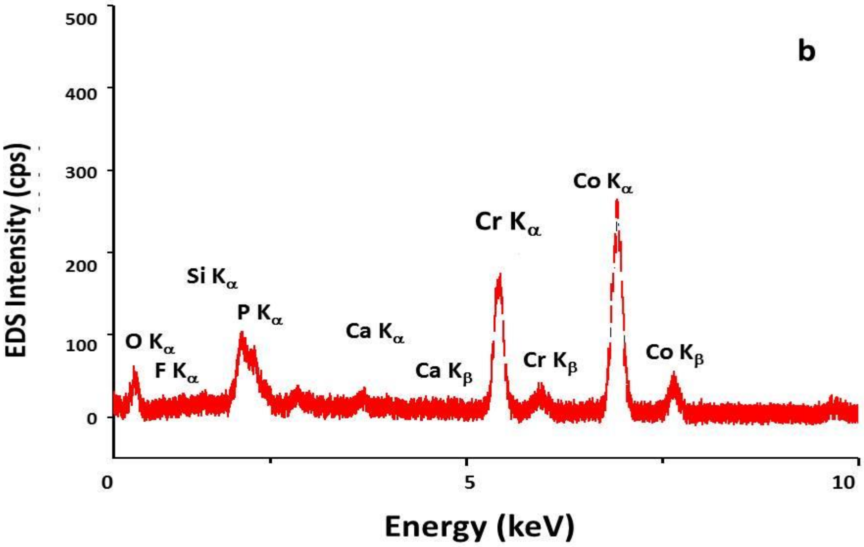

Figure 4.44 The energy dispersive analysis of X-rays (EDAX) analysis of the specimen in which fluorapatite nanopowder was coated onto Co-Cr-Mo alloy by pulsed laser deposition. In the specimen preparation the laser energy was 130 mJ and the pressure was maintained at 7×10^{-9} MPa. The exposure time in the specimen preparation was 20 minutes. The EDAX analysis was obtained by irradiating the specimen with a beam of electrons of energy 20 keV. The irradiation live-time was 120 seconds. The data were measured with a silicon ultra-thin window (SUTW).

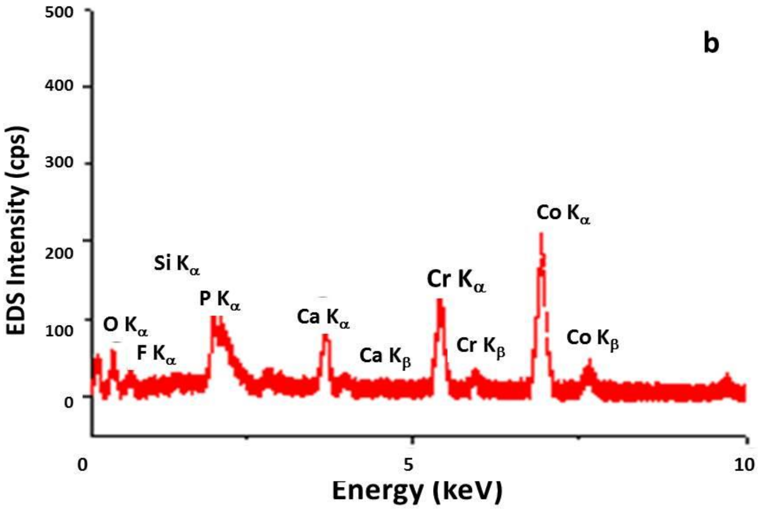

Figure 4.45 The energy dispersive analysis of X-rays (EDAX) analysis of the specimen in which fluorapatite nanopowder was coated onto Co-Cr-Mo alloy by pulsed laser deposition. In the specimen preparation the laser energy was 170 mJ and the pressure was maintained at 7×10^{-9} MPa. The exposure time in the specimen preparation was 10 minutes. The EDAX analysis was obtained by irradiating the specimen with a beam of electrons of energy 20 keV. The irradiation live-time was 120 seconds. The data were measured with a silicon ultra-thin window (SUTW).

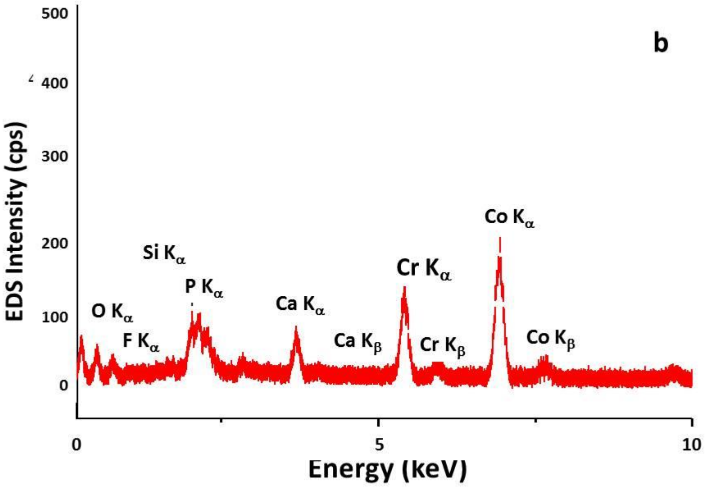

Figure 4.46 The energy dispersive analysis of X-rays (EDAX) analysis of the specimen in which fluorapatite nanopowder was coated onto Co-Cr-Mo alloy by pulsed laser deposition. In the specimen preparation the laser energy was 170 mJ and the pressure was maintained at 7×10^{-9} MPa. The exposure time in the specimen preparation was 15 minutes. The EDAX analysis was obtained by irradiating the specimen with a beam of electrons of energy 20 keV. The irradiation live-time was 120 seconds. The data were measured with a silicon ultra-thin window (SUTW).

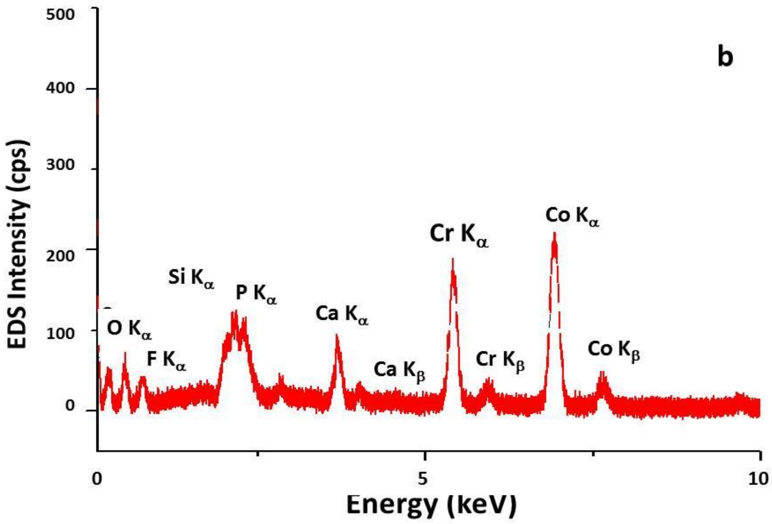

Figure 4.47 The energy dispersive analysis of X-rays (EDAX) analysis of the specimen in which fluorapatite nanopowder was coated onto a glass substrate by pulsed laser deposition. In the specimen preparation the laser energy was 130 mJ and the pressure was maintained at 7×10^{-9} MPa. The exposure time in the specimen preparation was 10 minutes. The EDAX analysis was obtained by irradiating the specimen with a beam of electrons of energy 20 keV. The irradiation live-time was 120 seconds. The data were measured with a silicon ultra-thin window (SUTW).

Concomitant with the discussion of page 68-69 of this study, the ratio of the concentration of Ca to Cr is for practical purposes significantly large as the Ca concentration is less than 0.5%. This indicates that since void areas were distinguished SEM analysis and with the EDAX analysis, the Ca concentration is virtually zero, the deposited layer was either by dissolution or by dislocation, transferred to the simulated body fluid.

The decrease in the extent of depletion (page 68-69) is also concomitant with the increase in the comparative concentration ratio of the concentration of Ca to that of Cr. Thus, 1) before the specimen, prepared at 130 mJ and five minutes exposure, was immersed into the SBF, the concentration ratio of Ca to Cr was 0.91; which, after immersion into the SBF is greater than 200; 2) before the specimen, prepared at 130 mJ and 10 minutes exposure, was immersed into the SBF, the concentration ratio of Ca to Cr was 5.0; which, after immersion into the SBF is 0.5; and 3) before the specimen, prepared at 130 mJ and five minutes exposure, was immersed into the SBF, the concentration ratio of Ca to Cr was 1.63; which, after immersion into the SBF is now approximately 2.2.

From these results it can be deduced that the exposure time should be increased so that a thicker layer can be deposited and the energy of the laser beam should be greater than or equivalent to 170 mJ.

4.4.3 Atomic force microscopic analysis, rendered as a three dimensional (3-D) image, of the degree of surface roughness

The microstructural topologies of the specimens that have been shown before only entails the 2-dimensional image of the surface.

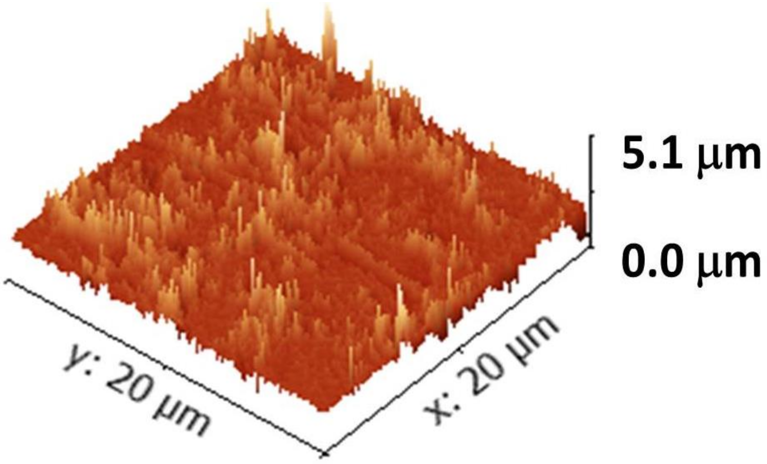

Figure 4.48 Atomic force microscopic analysis, rendered as a three dimensional (3-D) image, of the degree of surface roughness of the specimens in which fluorapatite was deposited onto a Co-Cr-Mo alloy by pulsed laser deposition. During the deposition, the laser energy was 130 mJ and the pressure was maintained at 7×10^{-9} MPa and during which the exposure time was five minutes.

More so, the extent of the roughness can therefore not be evaluated. For this reason, atomic force microscopic analyses were performed. These 3-dimensional images, are shown in figures 4.48 to 4.53.

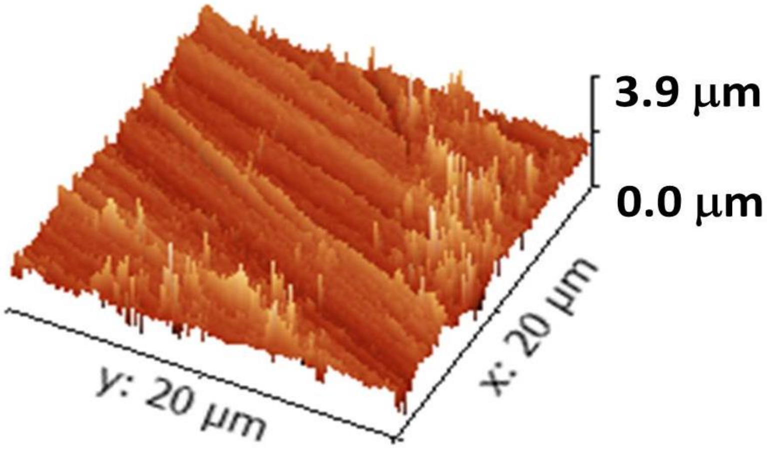

Figure 4.49 Atomic force microscopic analysis, rendered as a three dimensional (3-D) image, of the degree of surface roughness of the specimens in which fluorapatite was deposited onto a Co-Cr-Mo alloy by pulsed laser deposition. During the deposition, the laser energy was 130 mJ and the pressure was maintained at 7×10^{-9} MPa and during which the exposure time was 10 minutes.

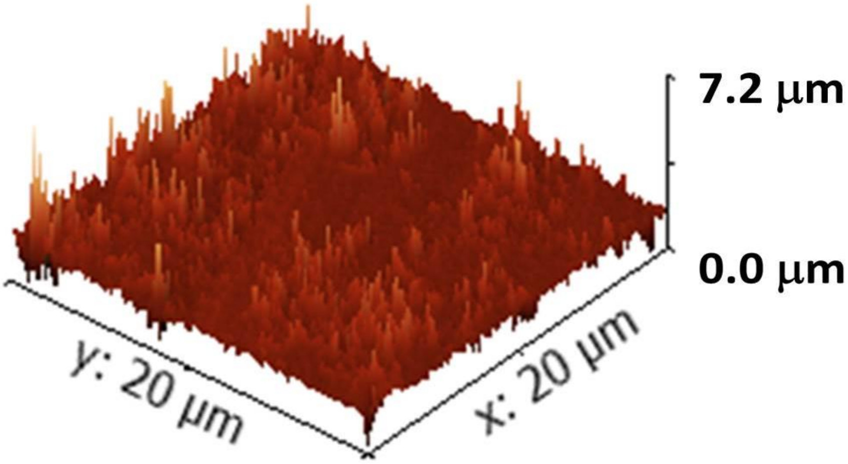

Figure 4.50 Atomic force microscopic analysis, rendered as a three dimensional (3-D) image, of the degree of surface roughness of the specimens in which fluorapatite was deposited onto a Co-Cr-Mo alloy by pulsed laser deposition. During the deposition, the laser energy was 130 mJ and the pressure was maintained at 7×10^{-9} MPa and during which the exposure time was 20 minutes.

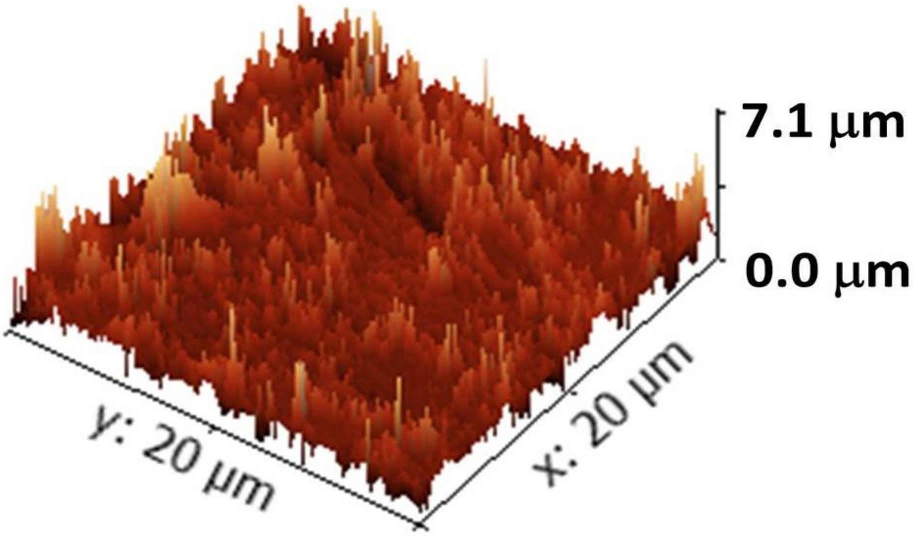

Figure 4.51 Atomic force microscopic analysis, rendered as a three dimensional (3-D) image, of the degree of surface roughness of the specimens in which fluorapatite was deposited onto a Co-Cr-Mo alloy by pulsed laser deposition. During the deposition, the laser energy was 170 mJ and the pressure was maintained at 7×10^{-9} MPa and during which the exposure time was 10 minutes.

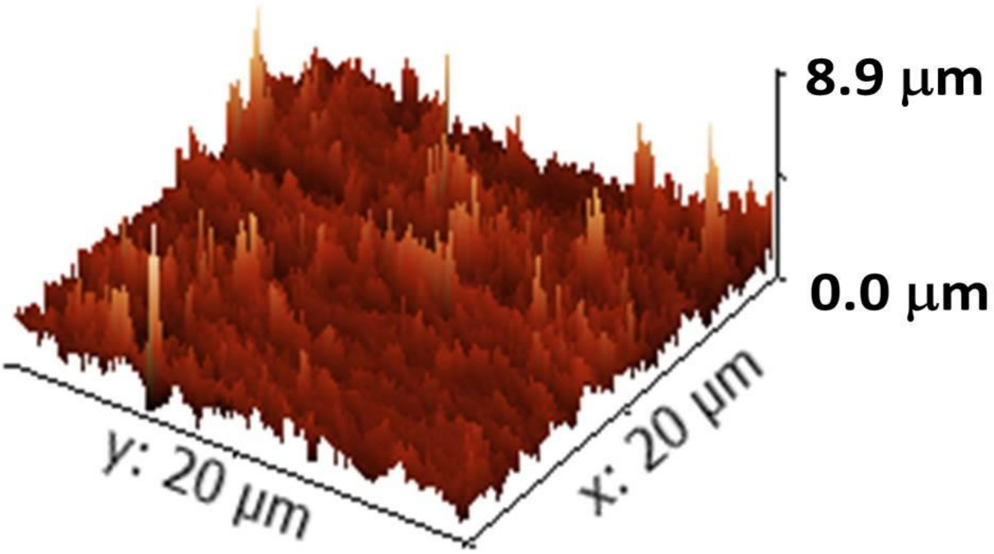

Figure 4.52 Atomic force microscopic analysis, rendered as a three dimensional (3-D) image, of the degree of surface roughness of the specimens in which fluorapatite was deposited onto a Co-Cr-Mo alloy by pulsed laser deposition. During the deposition, the laser energy was 170 mJ and the pressure was maintained at 7×10^{-9} MPa and during which the exposure time was 15 minutes.

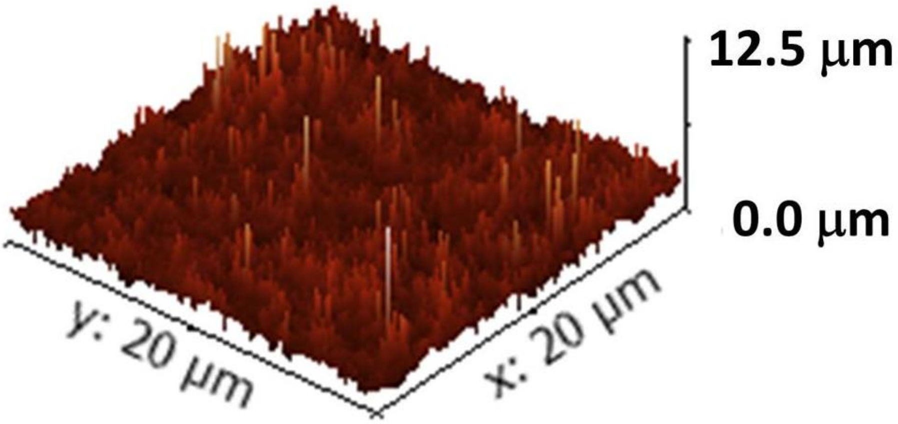

Figure 4.53 Atomic force microscopic analysis, rendered as a three dimensional (3-D) image, of the degree of surface roughness of the specimens in which fluorapatite nanopowder was coated onto a glass substrate by pulsed laser deposition. During the deposition, the laser energy was 130 mJ and the pressure was maintained at 7×10^{-9} MPa and during which the exposure time was 10 minutes.

Comparing figure 4.29 with figure 4.48 the estimated surface roughness increased from 1.75μm to 2.70μm. This translated to an increase of more than 50% in the surface roughness. This decrease is concomitant with the results obtained in the SEM and EDAX analysis. However, as the thickness of the deposited layer increased, the extent of surface roughness decreased. Similar results were obtained in the comparison of figure 4.30 with figure 4.49, figure 4.31 with figure 4.50 and figure 4.32 with figure 4.51.

Table 4.1: Comparison of AFM parameters $\bar{z}$, R_a, R_m, R_q, R_s and R_k, of specimens before and after immersion in simulated body fluid. The unit of energy is mJ and the time was measured in minutes. of the difference laser energy, pressure and time used during deposition of each sample. $\bar{z}$, R_a, R_m *and* R_q are expressed in nanometers.

Sample	*Energy*	*Time*	$\bar{z}$	R_a	R_m	R_q	R_s	R_k
				Before immersion in simulated body fluid				
Co-Cr-Mo	130	5	425	439	433	584	1.31	1.41
Co-Cr-Mo	130	10	722	719	713	1085	2.57	41.21
Co-Cr-Mo	130	20	715	703	710	868	0.49	-0.002
Co-Cr-Mo	170	10	970	964	960	1346	1.94	6.02
Co-Cr-Mo	170	15	620	647	671	790	0.19	0.51
Glass	130	10	2250	2180	2100	2453	0.5	-1.32
				After immersion in simulated body fluid				
Co-Cr-Mo	130	5	420	400	440	676	0.93	5.67
Co-Cr-Mo	130	10	345	370	332	518	0.09	3.46
Co-Cr-Mo	130	20	480	465	475	684	0.27	7.22
Co-Cr-Mo	170	10	790	747	755	1063	0.55	4.13
Co-Cr-Mo	170	15	845	824	810	1095	0.53	3.87
Glass	130	10	860	821	885	1170	0.39	4.31

For all values of confidence level of 95% (α=0.05) is assumed and is expressed as

$$0.95x_i \leq x_i \leq 1.05x_i \qquad (4)$$

For all data the difference between the $\bar{z}$, R_a and R_m values are not significant.

With respect to the depositions at 130 mJ; for five minutes, there is a significant increase in the R_q values. This indicates that temporal changes occurred during the surface formation. However, temporal changes that occurred during the irradiation times of 10 and 20 minutes indicate a decrease R_q. However, the difference in temporal changes in the surface formation compared with the irradiation time is parabolic in nature. Similar trends were also found for R_s and R_k. The parabolic nature of these trends are shown in figures 4.54, 4.55 and 4.56.

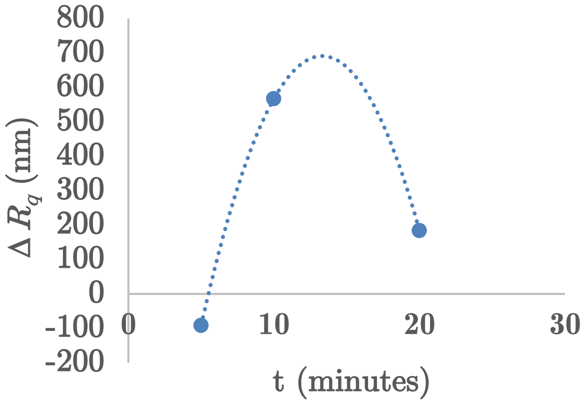

Figure 4.54. Plot of the difference in R_q against the irradiation time, t.

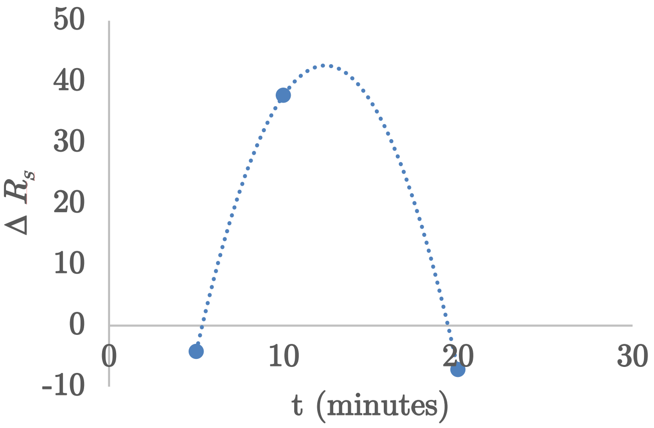

Figure 4.55. Plot of the difference in R_s against the irradiation time, t.

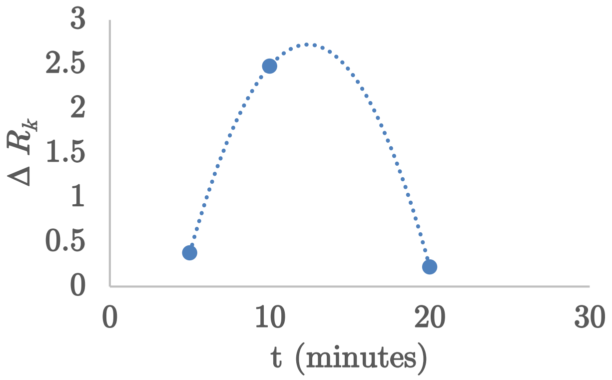

Figure 4.56. Plot of the difference in R_k against the irradiation time, t.

From the trends it is deduced that the optimal times for irradiation are respectively 13.2, 13.9 and 14.1 minutes.

For the depositions performed at 170 mJ for duration of 10 and 20 minutes on the Co-Cr-Mo substrate, the AFM parameters have similar trends as those deposited at 130 mJ.

Chapter 5

Conclusions and Recommendations

5.1 Conclusions

The main goals of the research work were: 1) to successfully coating the dental alloy Co-Cr-Mo with a fluorapatite nanocomposite thin-film using the pulsed laser deposition technique at various energies and exposure time durations and 2) to evaluate their bioactivity by immersing the specimens into a simulated body fluid for a period of 14 days and so systematically investigate how the thicknesses of the layers grow at these parameters.

It was found that:

1. At low laser beam energies, the surface roughness is relatively high and the roughness decreases with an increase in beam energy; and
2. an increase in the exposure time causes a decrease in surface roughness, with the proviso that exposure times should be greater than five minutes.;

It was however necessary to ensure that the laser energy for the FA deposition onto the Co-Cr-Mo alloy is optimized for the pressure. For best specimen preparation, the laser deposition of FA onto a simple glass substrate with different laser powers, and duration of deposition time and constant room temperature (RT). Even being able to get the average energy of laser 130-170 mJ and the average time of deposition of 5-20 minutes, this is the main role for the preparation of the protocol on precipitation FA of Co-Cr-Mo thin-films on glass substrate of the cheap price and easy to deals with the materials and to obtain the good results in other deposition processes or conditions.

In this study, the samples were synthesized from a compound in the infinity of small content of apatite fabrication FA infinitely complex at the initial stage by ball milling shown for the size of 55-65 nm, in which was used in the laser deposition process, making into solid-state cylindrical pellet with the diameter of 2 cm.

Evidence by the PLD deposition of FA content of Co-Cr-Mo by nanocomposite thin-film at RT with the change of laser power and the duration of deposition time results were also a play a major role of the thin-films become soften with uniform coating on the substrate.

The coated thin-films materials were immersed into the SBF solution for 14 days, and it is clearly noticeable that it can be converted successfully to biologically active type Co-Cr-Mo add FA nanometer thin-films by PLD.

The similar results were obtained in the present study when the FA content was increased by adding it in concentrations of 10, 15, 20% for Co-Cr-Mo nanocomposite alloys.

Synthesized materials were systematically characterized using of non-destructive surface analytic techniques such as X-ray probes (XRD), electron microscopic (SEM) with stoichiometry/compositional analysis EDS and atom probe based AFM were used in the present study.

1- The obtained FA nanopowders which were synthesized by 6 h of ball-milling under optimized mechanical alloying parameters including 300 rpm of rotation speed, ball to powder weight ratio equal to 35, and 8 balls with 20 mm in diameter.

2- The PLD deposition method used for high intensity laser beam fluence allows the deposition of thin dense film, the composition (stoichiometry) of which is close to that of initial targets, on the simple glass substrate, Co-Cr-Mo alloys and silicon substrate. The crystalline structure of the films far from equilibrium and does not correspond to the FA nanopowders of the initial targets.

3- Thin films with various dopant concentrations were fabricated and examined using the atomic force microscopy (AFM), for the film deposited on Co-Cr-Mo alloys bumps asymmetrically show so that it is more surface smoothness as the average 10 - 20 minutes sedimentation and laser energy 130 - 170 mJ and deposition chamber pressure 7×10^{-9} MPa. The surface morphological images from SEM shows that increased sedimentation time and the laser energy and the pressure were stable when 7×10^{-9} MPa FA nanopowder be more intense and spread on a regular basis. On the contrary, whenever the time of deposition and the energy of the laser deposition and less time pressure is reduced sedimentation FA nanopowder be heterogeneous and with varying density of on the sample areas.

5.2 Recommendations

Based on finding of this study the following are recommendation:

Many questions still remain regarding the *in vivo* effects of these materials. Even if the body's response to modified (laser treated) alone is better understood, the matrix in which coated composite films are likely alter possible desired response in near future. Thus more in depth *in vitro* and *in vivo* studies are needed to assess the potential of FA and suitable doped metal composites for dental/bone graft or other *in vivo* applications.

1- Chrome is a Co-Cr-Mo alloys of interest in compensation teeth and bones and the development of this alloy and approval of life has become is very necessary because of very high their qualities and features.

2- The *in vivo* study is a need to provide evidence of Co-Cr-Mo alloys can provide a useful service for patients who are using such alloys.

3- It should be needed for further investigation to improve the compatibility of these alloys compounds infinitesimally of FA nanopowder.

4- Clinical trials should be conducted at various intervals of immersion of the specimens into SBF, to make sure the output, which is obtained from this study and compared previous studies.

5- Laser entry in many fields supports used in future studies to develop and study dental based alloys and development of efficiency, using pulsed laser deposition (PLD) technique have shown good results in the precipitation of FA nanopowder.

6- *In vivo* study are needed to support laboratory data, in order to provide evidence that FA nanometer particle-sized powder may can meaningfully provide a useful service for the patients and the improvement of the tooth and restoration longevity.

Chapter 6

References

Anusaice, K.J. 2003. Informatics systems to assess and apply clinical research on dental restorative materials. *Advances in Dental Research*, vol. 17(1), pp. 43-48.

Ali, M. & Basu, P. 2010. Mechanochemical synthesis of nano-structured TiC from Ti2 powders. *Journal of Alloys and Compounds,* vol. 500(2), pp. 220-223.

Amoruso, S., Ausanio, G., Delisio, C., Iannotti, V., Vitiello, M., Wang, X. & Lanotte, L. 2005. Synthesis of nickel nanoparticles and nanoparticles magnetic films by femtosecond laser ablation in vacuum. *Applied Surface Science*, vol. 247(1-4), pp. 71-75.

Amoruso, S., Sambri, A., Vitiello, M. & Wang, X. 2006. Propagation of LaMnO3 laser ablation plume in oxygen gas. *Applied Surface Science*, vol. 252(13), pp. 4712-4716.

Aoba, T. 1997. The effect of fluoride on apatite structure and growth. *Critical Reviews in Oral Biology & Medicine*, vol. 8(2), pp.136-153.

Asgar, K. & Allan, F.C. 1968. Microstructure and physical propertiesof alloys for partial denture casting. *Journal of Dental Research*, vol. 47(2), pp. 180-197.

Asgar, K. & Peyton, F.A. 1961. Effect of microstructure on the physical properties of Co-base alloys. *Journal of Dental Research*, vol. 40(1), pp. 63-72.

Bale, W.F. 1940. A comparative Roentgen-Ray diffraction study of several natural apatites and the apatite-like constituent of bone and teeth substance, *American Journal of Roentgenology*, vol. 43, pp. 735-747.

Baran, G.R. 2002. Cast and wrought base metal alloys. *Restorative Dental Materials*. 11th edition, St. Louis. Mosby.

Barrere, F., van Blitterswijk, C.A., deGroot, K. & Layrolle, P. 2002. Nucleation of biomimetic, Ca-P coatings on Ti_6Al_4V from a SBF5 solution: Influence of magnesium. *Biomaterials*, vol. 23(10), pp. 2211-2220.

Bauer, S.P., Schmuki, K., VON DER MARK. & Park, J. 2012. Engineering biocompatible implants surfaces. *Progress in Materials Science*, vol. 58(3), pp. 261-326.

Ben Ayed, F., Bouaziz, J. & Bouzouita, K. 2001. Calcination and sintering of FA under argon atmosphere. *Journal of Alloys and Compounds*, vol. 322(1-2), pp. 238-245.

Ben Ayed, F., Bouaziz, J. & Bouzouita, K. 2006. Mechanical resistance of fluorapatite. *Annales De Chimie-Science Des Matériaux*, vol, 31(4), pp. 393-406.

Ben Ayed, F., Bouaziz, J., Khattech, I. & Bouzouita, K. 2001. Produit de solubilité apparent de la fluorapatite frittée. *Annales De Chimie-Science Des Matériaux*, vol. 26(6), pp. 75-86.

Bianco, A., Cacciotti, I., Lombaedi. M., Montanaro, L., Bemporad, E. & Sebastiani, M. 2010. F-substituted hydroxyapatite nanopowder: Thermal stability, sintering behavior and mechanical properties. *Ceramics International*, vol. 36(1), pp. 313-122.

Bianco, A., Cacciotti, I., Lombardi, M. & Montanaro, L. 2009. Si-substituted hydroxyapatite nanopowders: Synthesis, thermal stability and sinter-ability. *Materials Research Bulletin*, vol. 44(2-4), pp. 345-354.

Binnig, G & Smith, D. P. E. 1986. Single-tube three-dimensional scanner for scanning tunneling microscopy. *Review of Scientific Instruments*, vol. 57(8), pp. 1688-1689.

Bogdanov, B.I., Pashev, P.S., Hristov, J.H. & Markovska, I.G. 2009. Bioactive fluorapatite-containing glass ceramics. *Ceramics International*, vol. 35(4), pp. 313-122.

Braic, M., Balaceanu, M., Vladescu, A., Kiss, A., Braic, V., Epurescu, G., Moldovan, A., Birjega, R. & Dinescu, M. 2007. Preparation and characterization of titanium oxynitride thin films. *Applied Surface Science*, vol. 253(19), pp. 8210-8214.

Budak, I., Kosec, B. & Sokovic, M. 2012. Application of contemporary engineering techniques and technologies in the field of dental prosthetics. *Journal of Achievements in Materials and Manufacturing Engineering*, vol 54(2), pp. 233-241.

Bui, N. & Dabosi. F. 1981. *Comportement electrochimique en milieu salin de quelques alliages dentaires a base de nickel etde cobalt.* CIMD80/Pcy ed. Metallurgie dentaire. Paris.

Bumgardner, J.D. & Lucas, L.C. 1993. Surface analysis of nickel-chromium dental alloys. *Dental Materials*, vol. 9(4), pp. 252-259.

Cai, Y., Zhang, S., Zeng, X., Wang, Y., Qian, M. & Weng, W. 2009. Improvement of bioactivity with magnesium and fluorine ions incorporated hydroxyapatite coating via sol-gel deposition on Ti_6Al_4V alloys. *Thin Solid Films*, vol. 517(17), pp. 5347-5351.

Cheng, K., Han, G., Weng, W., Qu, H., Du, P., Shen, G., Yang, J. & Ferreira, J.M.F. 2003. Sol-gel derived fluoridated hydroxyapatite films. *Materials Reseach Bulletin*, vol. 38(1,1), pp. 89-97.

Chrisey, D. & Hubler, G.K. 1994. *Pulsed Laser Deposition of Thin Films*, Wiley, New York, USA.

Craig, R.G. 2004. *Restorative Dental Materials*. 11th ed. Mosby, St. Louis, USA.

Craig, R.G., Powers, J.M. & Wataha, J.C. 2000. *Dental Materials: Properties and Manipulation*. 7th ed. Mosby, Missouri, pp. 229-231.

Cullity, B.D. 1978. *Elements of X-ray Diffraction*, 2nd Edition, pp. 81-99. Addison-Wesley Publishing Company, New York, USA.

Davis, J.R. (Ed), 2003. *Handbook of Materials for Medical Devices.* ASM International, DOI: 10.1361, pp.31-37.

DeBoer, B.G., Sakthivel, A., Cagle, J.R. & Young, R.A. 1991. Determination of the antimony substitution site in calcium fluorapatite form powder X-ray diffraction data. *Acta Crystallographica*, vol. 47(5), pp. 683-692.

Devreker, F., Hardy, K., Van den Bergh, M., Vannin, S.A., Emiliani, S. & Englert, Y. 2001. Amino acids promote human blastocyst development *in vivo*. *Human Reproduction*, vol. 16(4), pp. 749-756.

Dobrzański, L.A. 2007. *Metallography of non-ferrous metals*, The Silesian University of Technology Publishing, Gliwice.

Eichner, K. 1983. Anwendung von metall-legierungen in der Zahnheilkunde-ein Űberblick. *ZWR - Das Deutsche Zahnärzteblatt*, vol. 92(2), pp. 28-36.

Elliott, J.C. 1998. *Structure and chemical properties of calcium phosphate*. In: Bres E, Hardouin P eds, Calcium Phosphate Materials–Fundamentals. Sauramps Medical, Montpellier, France, pp. 25-66.

Espevik, S. & Øilo, G. 1979. Oxidation of noble metal alloys for porcelain veneer crown. *Journal of Dental Research*, vol. 37(6), pp. 323-328.

Fathi, M.H. & Hanifi, A. 2007. Evaluation and characterization of nanostructure hydroxyapatite powder prepared by simple sol-gel method. *Materials Letters*, vol. 61(18), pp. 3978-3983.

Finkelstein, M.J. & Nancollas, G.H. 1980. Trace fluoride and its role in enamel mineralization. *Journal of Biomedical Materials Research,* vol 14(4), pp. 533-535.

Fleet, M.E. & Pan, Y. 1997. Site preference of rare earth elements in fluorapatite: Binary (LHREE+HREE)-substituted crystals. *American Mineralogist*, vol. 82(9-10), pp. 870-877.

Flinn, R.A. & Trojan, P.K. 1986. *Metallic structures. Engineering materials and their applications.* 3rd edition, Houghton Mifflin, New York, USA.

Gerstrofer, J.G., Sauer, H.K. & Pässler, K. 1991. Ion release from Ni--Cr--Mo and Co--Cr--Mo casting alloys. *International Journal of Prosthodontics*, vol. 4(2), pp. 152-158.

Giacchi, J.V., Morando, C.N., Fornaro, O. & Palacio, H.A. 2010. Microstructural characterization of as-cast biocompatible Co-Cr-Mo alloys. *Materials Characterization*, vol. 61(1), pp. 53-61.

Goodhew, P.J., Humpreys, T. & Branland, R. 2001. *Electron Microscopy & Analysis* 3rd edition, Taylor & Francis Group, New York, USA.

Granchi, G., Ciapetti, S., Stea, L., Savarino, F., Filippini, A., Sudanese, G., Zinghi, G. & Montanaro, L. 1999. Cytokine release in mononuclear cells of patients with Co-Cr hip prosthesis. *Biomaterials*, vol 20(12), pp. 1079-1086.

Hanks, C.T., Wataha, J.C. & Sun, Z.L. 1996. *In vitro* models of biocompatibility. *Dental Materials*, vol. 12(3), pp. 186-193.

Hanks, J.H. & Wallace, R.E. 1949. Relation of oxygen and temperature in the preservation of tissues by refrigeration. *Journal of Biology and Medicine*, vol. 71(2), pp. 196-200.

Haudin, J.M. & Perrin, M.Y. 1981. Role des elements d'addition (B, Si, Al, Be) sur la structure des alliages nickel-chrome. CIMD 80/Pyc ed. *Metallurgie Dentaire*, Paris.

Haynes, D.R., Crotti, T.N., Haywood, M.R. & Biomed, J. 2000. Corrosion of and changes in biological effects of cobalt chrome alloy and 316L stainless steel prosthetic particles with age. *Journal of Biomedical Materials Research*, vol. 49(2), pp. 167-175.

Hendricks, S.B., Jefferson, M.E. & Mosley, V.M. 1932. The crystal Structures of some natural and synthetic apatitelike substances. *Zeitschrift für Kristallographie-Crystalline Materials*, vol. 81(1), pp. 352-369.

Herö, H., Syverud, M., Gjönnes, J. & Horst, J.A. 1984. Ductility and structure of some cobalt-base dental casting alloys. *Biomaterials*, vol. 5(4), pp. 201-208.

Hildebrand, H, F., Veron, C., & Martin, P. 1989. Nickel, chromium, cobalt dental alloys and allergic reactions: an overview. *Biomaterials*, vol. 10(8), pp. 545-548.

Horovitz, M.B., Neto, F.B., Garbogini, A. & Tschiptschin, A.P. 1996. Nitrogen bearing martensitic stainless steels: Microstructure and properties. *The Iron and Steel Institute of Japan International*, vol. 36(7), pp. 840-845.

Huang, P., Salinas--Rodriguez, A. & Lopez, H.F. 1999. Tribological behaviourof cast and wrought Co-Cr-Mo implant alloys. *Journal of Materials Science & Technology*, vol 15(11), pp. 1324-1330.

Hughes, J.M., Cameron, M. & Crowley, K.D. 1991. Ordering of divalent cations in the apatite structure: Crystal structure refinements of natural Mn-and Sr-bearing apatite. *American Mineralogist*, vol. 76, pp. 1857-1862.

Hussain, S. 2009. *Investigation of Structural and Optical Properties of Nanoceystalline Zn,* MSc. Thesis. (Available online, 04/11/2009).

Karamalegos, C. & Bolton, V.N. 1999. A prospective comparison of in house and commercially prepared Earles balanced salt solution in human *in vitro* fertilization. *Human Reprodution*, vol. 14(7), pp. 1842-1846.

Kawasaki, M., Takahashi, K., Maeda, T., Tsuchiya, R., Shinohara, M., Ishiyama, O., Yonezawa, T., Yoshimoto, M. & Koinuma, H. 1994. Atomic control of the $SrTiO_3$ crystal surface. *Science*, vol. 226(5190), pp. 1540-1542.

Kheradmandfard, m., Fathi, M.H., Ahangarian, M. & Mohammadi Zahrani, E. 2012. *In vitro* bioactivity evaluation of magnesinm-substituted fluorapatite nanopowders. *Ceramics International*, vol. 38(1), pp. 169-175.

Kiel, M., Krauze, A. & Marciniak, L 2008. Corrosion resistance of metallic implants used in bone surgery. *Archives of Materials Science and Engineering*, vol. 30(2), pp. 77-80.

Kim, S.J., Bang, H.G., Song, J.H. “& Park, S.Y. 2009. Effect of fluoride additive on the mechanical properties of hydroxyapatite/alumina composites. *Ceramics International*, vol. 35(4), pp. 1647-1650.

Klawitter, J.J., Weinstein, A.M. & Peterson, L.J 1977. Fabrication and characterization of Co-Cr-Mo alloy dental implants. *Journal of Dental Research*, vol 56(5), pp. 474-480.

Kliner, T., Dempsey, A.J., Pilliar, R.M. & Weatherly, G.C. 1987. The effects of nitrogen additions to a cobalt--chromium surgical implant alloy, Part 1: Processing and microstructure, *Journal of Materials Science*, vol. 22(2), pp. 565-574.

Kohn, D.H. 2002. Mechanical properties. *Restorative Dental Materials.* 11th edition, St. Louis. Mosby.

Kojima, S. 1980. Investigations of sag-resistance of precious alloys for porcelain firing. Effect of Fe, In and Sn addition on the distortion at high temperature. *Journal of Digital Asset Management*, vol. 22, pp. 21-36.

Kokubo, T. & Nan-Cryst, J. 1990. Surface chemistry of bioactive glass-ceramics. *Journal of Nao-Crystalline Solids*, vol. 120(1-3), pp. 138-151.

Kokubo, T. & Takadama, H. 2006. How useful is SBF in predicting *in vivo* bone bioactivity? *Biomaterials*, vol. 27(15), pp. 2907-2915.

Kokubo, T. 1991. Bioactive glass ceramics: properties and applications. *Biomaterials*, vol. 12(2), pp. 155-163.

Kokubo. T., Kushitani, H., Sakka, S., Kitsugi, T. & Yamamuro, T. 1990. Soluations able to reproduce *in vivo* surface-structure changes in bioactive glass-ceramic A-W. *Journal of Biomedical Materials Research*, vol. 24(6), pp. 721-734.

Koster, G., Kropman, B.L., Rijnders, G., Blank, D.H.A. & Rogalla, H. Appl. 1998. Quasi-ideal strontium titanate crystal surfaces through formation of strontium hydroxide. *Applied Physics Letters*, vol. 73(20), pp. 2920-2922.

Krishna, B.V., Bosa, S. & Bandyopadhyay, A. 2007. Low stiffness porous Ti structures for load-bearing implants. *Acta Biomaterialia*, vol. 3(6), pp. 997-1006.

Lee, J., Leng, Y., Chow, K., Ren, F., X., Wang, K. & Lu, X. 2011. Cell culture medium as an alternative to conventional simulated body fluid. *Acta Biomaterialia*, vol. 7(6), pp. 2615-1622.

Lee, J., Lucas, L., O'Neal, J., Lacefield, W. & Lemons, J. 1985. In vitro corrosion analyses of nickel-base alloys. *Journal of Dental Research*, vol. 64, pp. 317.

Lee, S.H., Takahashi, E., Nomura, N. & Chiba, A. 2006. Effect of carbon addition on microstructure and mechanical properties of a wrought Co-Cr-Mo implant alloy. *Materials Transactions*, vol. 47(2), pp. 287-291.

Leroy, N. & Bres, E. 2001. Structure and substitutions fluorapatite. *European Cells and Materials*, vol. 2(1473-2262), pp. 36-48.

Losertová, M. 2012. *Progresivní materiály. Vydání první.* Vysoká škola báňská – Technická univerzita Ostrava.

Manaranche, C. & Hornberger, H. 2007. A proposal for the classification of dental alloys according to their resistance to corrosion. *Dental Materials*, vol. 23(11), pp. 1428-1437.

Marozau, I., Shkabko, A., Dinescu, G., Döbeli, M., Lippert, T., Logvinovich, D., Malle-pell, M., Schneider, C. W., Weidenkaff, A & Wokaun, A. 2009. Pulsed laser deposition and characterization of nitrogen-substituted $SrTiO_3$ thin films. *Applied Surface Science*, vol. 225(10), pp. 5252-5255.

McLean, J.W. 1983. The metal-ceramic restoration. *Dental Clinics of North America*, vol. 27(4), pp. 747-761.

Menzel, J., Kirschner, W. & Stein, G. 1996. High nitrogen containing Ni-free austenitic steels for medical applications. *The Iron and Steel Institute of Japan International*, vol. 36(7), pp. 893-900.

Meyer, J.M. 1977. Corrosion resistance of nickel-chromium dental casting alloys. *Corrosion Science*, vol. 17(12), pp. 971-982.

Meyer, J.M., Payan, J. & Nallay, J.N. 1979. Evaluation of alternative alloys to precious ceramic alloys. 1. Mechanical properties. *Journal of Oral Rehabilitation*, vol. 6(3), pp. 291-309.

Miao, S., Weng, W., Cheng, K., Du, P., Shen, G., Han. G. & Zhang, S. 2005. Sol-gel preparation of Za-doped fluoridated hydroxyapatite films. *Surface and Coatings Technology*, vol. 198(1-3), pp. 223-226.

Milošev, I. 2009. Metallic materials for biomedical. *Pure and Applied Chemistry*, vol. 83(2), pp. 309-324.

Miyake, M., Ishigaki, K. & Suzuki, T. 1986. Structure refinements of Pb^{2+} ion-exchanged apatites by X-ray powder pattern-fitting. *Journal of Solid Chemistry*, vol. 61, pp. 230-235.

Montenegro, M.J., Conder, K., Döbeli, M., Lippert, T., Willmott, P.R. & Wokaun, A. 2006. Pulsed reactive crossed beam laser ablation of $La_{0.6}Ca_{0.4}CoO_3$ using ^{18}O: Where does the oxygen come from? *Applied Surface Science*, vol. 252(13), pp. 4642-4646.

Moffa, J.P. 1983. Alternative dental casting alloys. *Dental Clinics of North America - Journal*, vol. 27 (4), pp. 733-746.

Montero-Ocampo, C., Talavela, M. & Lopez, H. 1999 Effect of alloy preheating on the mechanical properties of as-cast Co-Cr-Mo-C alloys. *Metallurgical and Materials Transactions: A*, vol. 30(3), pp. 611-620.

Mori, M., Yamanaka, K., Mastsumoto, H. & Chiba, A. 2010. Evolution of cold-rolled microstructures of biomedical Co-Cr-Mo alloys with and without N doping. *Materials Science and Engineering: A*, vol. 528(2), pp. 614-621.

Morris, H.F., Manz, M., Stoffer, W. & Weir, D. 1992. Casting alloys: the materials and "The Clinical Effects". *Advances in Dental Research*, vol. 6, pp. 28-31.

Mueller, H.J., Lenke, J.W. & Bapna, M.S. 1988. Surface analysis of tarnished dental alloys. *Scanning Microscopy*, vol. 2(2), pp. 777-787.

Neilson, J.P. & Tuccillo, J.J. 1966. Grain size in cast alloys. *Journal of Dental Research*, vol. 45(3), pp. 946-949.

Ohtsuki, C., Aoki, Y., Kokubo, T., Bando, Y., Neo, M., Nakamura, T & Ceram. J. 1995. Transmission electron microscopic observation of glass-ceramic A-W and apatite layer formed on its surface in a simulated body fluid. *Journal of the Ceramic Society of Japan*, vol. 103 (5), pp. 449-454.

Ohura, K., Nakamura, T., Yamamuro, T., Kokubo, T., Ebisaw, A.Y. & Kotoura, Y. 1991. Bane-bonding ability of P_2O_5-free $CaO{\cdot}SiO_2$ glasses. *Journal of Biomedical Materials Research*, vol. 25(3), pp. 357-365.

Plouvier, V. 1997. *Etude au niveau de deux sites régionaux*. Université Lille 2, France.

Postek, M. T. P., Howard, K.S., Johnson, A.T. & McMiche, K.L. 2001. *Scanning Electron Microscopy*, Ladd Research Industries, 83 Holly court, Williston, USA.

Powers, J.M. & Sakaguchi, R.L. 2006. *Craig's Restorative Dental Materials*. Mosby Publishing 12th edition, Missouri, USA.

Ramírez-Vidaurri, L.E., Castro-Román, M., Herrera-Trejo, M., García-López, C.V. & Almanza-Casas, E. 2008. Cooling rate and carbon content on the fraction of secondary phase precipitate in as-cast microstructure of AFTM F75 alloy. *Journal of Materials Processing Technology*, vol. 209(4), pp. 1681-1687.

Raub, C.J. & Ott, D. 1983. Gold casting alloys. The effect of zinc addition on their behavior. *Gold Bullion*, vol. 16(2), pp. 46-51.

Reimann, Ł. & Dobrzański, L.A. 2011. Microstructure and hardness of base cobalt alloys used in dentistry engineering. *Works of XXXIX Materials Engineering School. Monograph (editor: J. Pacyna),* Krakov-Krynica, vol. 49(2), pp. 198-202.

Ringer, S. & Physiol, J. 1882. Concerning the influence exerted by each of the constituents of the blood on the contraction of the ventricle. *Journal of Physiology Cambridge*, vol. 3(5-6), pp. 380-393.

Rodrigues-Lorenzo, L.M., Hart, J.N. & Gross, K.A. 2003. Influence of fluorine in synthesis of apatites: Synthesis of solid solutions of hydroxyl fluorapatite, *Biomaterials*, vol. 24(21), pp. 3777-3785.

Rui, N. & Dabosi, F. 1981. Comportement electrochimique en milieu salin de quelques alliages dentaires a base de nickel etde cobalt. CIMD*)/Pcy ed. *Metallurgie Dentaire*, Paris.

Ryan, G., Pandit, A. & Apatsidis, D.P. 2006. Fabrication methods of porous metals for use in orthopaedic applications. *Biomaterials*, vol. 27(13), pp. 2651-1670.

Salinas-Rodriguez, A. 1999. ASTM STP 1365. 108–121.

Sharma, M., Ramesh Kumar, A.V., Singh, N., Adya, N. & Saluja, B. 2008. Electrochemical corrosion behavior of dental/implant alloys in artificial saliva. *Journal of Materials Engineering and Performance*, vol. 17 (5), pp. 695-701.

Shi, H., Guo, D. & Ouyang, Y. 2008. Structural evolution of mechanically alloyed nanocrystalline FeAl intermetallics. *Journal of Alloys and Compounds*, vol. 455(1-2), pp. 207-209.

Shi, L.Q., Northwood, D.O. & Cao, Z.W. 1993. Dislocation network models for recovery creep deformation. *Journal of Materials Science*, vol. 28(22), pp. 1312-1316.

Staiger, M.P. & Pietak, A.M. 2006. Magnesium and its alloys as orthopaedic biomaterials: A review. *Biomaterials*, vol. 27(9), pp. 1728-1734.

Suchanek, W.L., Byrappa, K., Shuk, P., Riman, R.E., Janas, V.F. & TenHuisen, K.S. 2004. Preparation of magnesium-substituted hydroxyapatite powders by the mechanochemical-hydrothermal method. *Biomaterials*, vol. 25(19), pp. 4647-4657.

Sudarsanan, K., Mackie, P.E. & young, R.A. 1972. Comparison of synthetic and mineral fluorapatite, Ca5(PO4)3F, in crystallographic detail. *Materials Research Bulletin*, vol. 7(11), pp. 1331-1338.

Suitch, P.R., Lacout, J.L., Hewat, A. & Young, R.A. 1985. The structure location and role of Mn^{2+} Partially substituted for Ca^{2+} in fluorapatite. *Acta Crystallographica: B*, vol. 41(3), pp. 173-179.

Supady, J. 2010. Types of tooth filling used in dental treatment in 19th century. *Journal of Stomatology*, vol. 63(4), pp. 273-281.

Tesk, J.A. & Waterstrat, R.M. 1985. Physical metallurgy of dental casting alloy. Co-Cr-Mo system; Ni-Cr system; ferritic and austenitic, titanium alloys. *Encyclopedia of Materials Science and Engineering*, Elmsford(NY): Pergamon Press.

Townsend, J.D. & Hamilton, A.I. 1983. Biologic evaluation of a silver-copper-germanium dental casting alloy and a gold-germanium coating alloy. *Journal of Dental Research*, vol. 62(8), pp. 899-903.

Tuccillo, J. J & Nielsen, J. P. 1971. Observations of onset of sulfide tarnish on gold-based alloys. *Journal of Prosthetic Dentistry*, vol. 25, pp. 629-637.

Tuna, S.H., Pekmez, N.Ö., Keyf, F. & Canli, F. 2009. The influence of the pure metal components of four different casting alloys on the electrochemical properties of the alloys. *Dental Materials*, vol. 25(9), pp. 1096-1103.

Upadhyay, D., Panchal, M.A., Dubey, R.S. & Srivastava, V.K. 2006. Corrosion of alloys used in dentistry. *Materials Science & Engineering A*, vol. 432 (1-2), pp. 1-11.

Walke, W., Paszenda, Z. & Tyrlik-Held, J. 2006. Corrosion resistance and chemical compositions investigations of passive layer on the implants surface of Co-Cr-W-Ni alloy. *Journal of Achievements in Materials and Manufacturing Engineering*, vol. 16(1-2), pp. 74-79.

Wang, X.Y., Rice, D.M., Lee, Y.S & Downer, M.C. 1994. Time-Resolved Electron Temperature Measurement in a Highly-Excited Gold Target UsingFemtosecond Thermionic Emission. *Physical Review B*, vol. 50 (11), pp. 8016-8019.

Wapner, K.L. 1991. Implications of metallic corrosion in total knee arthroplasty. *Orthopedics Practice Research*, vol. 271, pp. 12-20.

Wataha, J.C, & Lockwood, P.E. 1998. Release of elements from dental casting alloys into cell-culture medium over 10 months. *Dental Materials*, vol. 14(2), pp. 158-163.

Wataha, J.C. 2000. Biocompatibility of dental casting alloys. *Journal of Prosthetic Dentistry*, vol. 83(2), pp. 223-234.

Wataha, J.C. 2001. Principles of biocompatibility for dental practitioners. *Journal of Prosthetic Dentistry*, vol. 86(2), pp. 203-209.

Wataha, J.C. 2002. Alloys for prosthodontics restorations. *Journal of Prosthetic Dentistry*, vol. 87(4), pp. 351-363.

Wataha, J.C. 2002a. Noble alloys and solders. Craig RG, Powers JM, editors. *Restorative Dental Materials* 11th edition, St. Louis. Mosby.

Wataha, J.C. 2002b.Nature of metals and alloys. *Restorative Dental Materials*. 11th edition, St. Louis. Mosby.

Wataha, J.C. 2002c. Alloys for prosthodontics restoration. *Journal of Prosthetic Dentistry*, vol. 87(4), pp. 351-383.

Wataha, J.C. 2002d. Casting and soldering. *Restorative Dental Materials.* 11th edition, St. Louis. Mosby.

Wataha, J.C., Craig, R.G. & Haks, C.T. 1991a. The Release of elements of dental casting alloys into cell-culture medium. *Dental Research*, vol. 70(6), pp. 1014-1018.

Wataha, J.C., Lockwood, P.E., Khajotia, S.S. & Turner, R. 1998. Effect of pH on element release from dental casting alloys. *Journal of Prosthetic Dentistry*, vol. 80(6), pp. 691-698.

Willmott, P.R., Timm, R. & Huber, J.R. 1997. Reactive crossed beam scattering of a Ti plasma and a N_2 pulse in a novel laser ablation method. *Applied Physics*, vol. 82(6), pp. 2082-2092.

Willmott, P. R & Huber, J. R. 2000. Pulsed laser vaporization and deposition. *Reviews of Modern Physics*, vol. 72(1), pp. 315-328.

Xue, W., Krishna, B.V., Bandyopadhyay, A. & Bosa, S. 2007. Processing and biocompatibility evaluation laser processed porous titanium. *Acta Biomaterialia*, vol. 3(6), pp. 1007-1018.

Yang, Z.H., Zhou, Y., Jia, D.C. & Meng, Q. 2008. Microstructures and properties of $SiB_{0.5}C_{1.5}N_{0.5}$ ceramics consolidated by mechanical alloying and hot pressing. *Materials Science and Engineering: A*, vol. 489(1-2), pp. 187-192.

Zhang, H. & Darvell, B.W. 2010. Constitution and morphology of hydroxyapatite whiskers prepared using amine additives. *Journal of the European Ceramic Society*, vol. 30(10), pp. 2041-2048.

Zhuang, L.Z. & Langer, E.W. 1989. Effects of alloy additions on the microstructures and tensile properties of cast Co-Cr-Mo alloy used for surgical implants. *Journal of Materials Science*, vol. 24(12), pp. 4324-4330.

Zupancic, R., Legat, A. & Funduk, N. 2006. Tensile strength and corrosion resistance of brazed and laser-welded cobalt–chromium alloy joints. *The Journal of Prosthetic dentistry*, vol. 96(4), pp. 273-282.